The Hypothetical Population of Intermediate Mass Black Holes In the Galactic Nucleus: Could a steady state of intermediate-mass black holes exist in the galactic centre?

Hochart, Erwan

Citation

Hochart, E. (2023). *The Hypothetical Population of Intermediate Mass Black Holes In the Galactic Nucleus: Could a steady state of intermediate-mass black holes exist in the galactic centre?*.

LEIDEN UNIVERSITY

THE HYPOTHETICAL POPULATION OF INTERMEDIATE-MASS BLACK HOLES IN THE GALACTIC NUCLEUS

Could a steady state of intermediate-mass black holes exist in the galactic centre?

THESIS

Submitted in partial fulfillment of the
requirements for the degree of

MASTER OF SCIENCE
in
PHYSICS

Author: Erwan Hochart
Student ID: s2009269
Supervisor: Prof.dr. Simon PORTEGIES ZWART
Second Corrector: Dr. M. SCHALLER

Leiden, the Netherlands, January 19, 2023

The Hypothetical Population of Intermediate Mass Black Holes In the Galactic Nucleus

Erwan Hochart

Huygens-Kamerlingh Onnes Laboratory, Leiden University
P.O. Box 9500, 2300 RA Leiden, The Netherlands

January 19, 2023

"It's all a great mystery...
Look up at the sky and
you'll see how everything changes"

- Antoine de Saint-Exupéry, The Little Prince

Acknowledgements

Contents

Abstract

This thesis aims to alleviate the final parsec problem by investigating the hypothetical intermediate-mass black hole environment lying at the cores of galaxies, a model first proposed by Ebisuzaki et al. (2001) [1]. Although intermediate-mass black holes remain undetected, their nature could be the key to understanding supermassive black hole formation.

If they are indeed present at the hearts of galaxies, their mutual interactions encourage supermassive black hole-intermediate-mass black hole merging events. Such merging events bypass theoretical constraints placed by binary dynamics and the Eddington limit, allowing for supermassive black holes to grow into their colossal sizes, and could potentially help explain their existence in the early stages of the Universe's life.

We investigate this model using both a Newtonian (`Hermite`) and post-Newtonian (`HermiteGRX`) algorithm. The post-Newtonian algorithm incorporates terms up to order 2.5, allowing it to model gravitational wave emission, which acts as an energy sink source and encourages merging events. In addition to comparing the results found using either algorithm, we forecast its corresponding gravitational wave events.

More specifically, assuming a steady intermediate-mass black hole infall rate of one every 7 Myr, we predict a population of $N_{\mathrm{IMBH}} = 15 \sim 20$ residing at the inner 0.4pc of the Milky Way galaxy. In turn, the future gravitational wave interferometer LISA and the proposed one μAres will be able to detect up to 926 supermassive black hole-intermediate-mass black hole merging events per year up to a redshift $z \leq 3$. This value is three orders of magnitude larger than those found in various literature ([2]; [3]; [4]; [5]) due to the lack of observation of intermediate-mass black hole leaving a large parameter space in such analysis.

1 Introduction

Black holes are objects tethering on the limits of our theoretical understanding. They are so dense, that their gravity pulls in anything, even light if it lies within their grasp. Nearly a century after Einstein formulated his theory of general relativity which predicted black holes ([6]; [7]), their existence was finally confirmed with advanced LIGO detecting the merging between two stellar-mass black holes [8], ushering a new era in astronomy.

In general, three distinct black hole families exist. Stellar-mass black holes are those with masses $M \lesssim 10^2 M_\odot$ ($M_\odot$ signifying a solar mass). In the other extreme, with $M \gtrsim 10^5 M_\odot$ lie supermassive black holes. Though it has been several decades that their presence at the core of galaxies has been well established ([9]; [10]; [11]; [12]; [13]; [14]), definitive proof has recently been published with the Event Horizon Telescope (EHT) successfully imaging the supermassive black hole lying at the heart of M87 in 2019 [15]. More recently, EHT successfully imaged our own galactic supermassive black hole, Sagittarius A* [16].

At the cutting edge of our theoretical understanding, these objects are rich in information and understanding their nature can help us decipher many of nature's greatest riddles, for instance, the evolutionary history of galaxies or the underlying theory of gravity. Regarding galactic evolution, one curious aspect of supermassive black holes is their gargantuan sizes achieved, with their observed presence in the early Universe contradicting constraints placed by theory.

This is where the third black hole population, intermediate-mass black holes can be decisive. These are black holes with masses lying between the stellar mass and supermassive mass range ($10^2 \lesssim M\,[M_\odot] \lesssim 10^5$). Even so, though countless works, both theoretical and observational, have been devoted to them (i.e [17]; [18]; [19]; [20]; [21]) intermediate-mass black holes remain unobserved.

In this paper, we use numerical tools to investigate the model initially proposed in Ebisuzaki et al. (2001) [1]. Here, the authors suggested that the presence of a dense population of intermediate-mass black holes in the cluster forming the galactic core could exist (figure 1.1 showing an example). In this scenario, interactions between IMBH's will encourage merging events, whose accumulation over time helps grow the supermassive black hole mass, bypassing theoretical limitations such as the Eddington limit and the final parsec problem [22]. In a first, we simulate such a model using both a Newtonian algorithm and a post-Newtonian algorithm. The latter allows us to capture general relativistic effects, namely modelling the emission of gravitational waves.

1.1 Aim and Outline

The paper has two aims. The primary is to investigate whether galactic centres such as the Milky Way could host a population of tens to dozens of intermediate-mass black holes, and if so, what are some observational effects that emerge from such an environment. We aim to provide a definitive number on the hypothetical steady-state population of intermediate-mass black holes present at the heart of a Milky Way-like galaxy. The second aim of the report is to analyse differences between integrators using Newtonian or post-Newtonian formalism.

To achieve this, we start by providing a theoretical background on various themes essential to the report. More specifically, in section 2, we expand on our current description of black holes, discuss the global properties of clusters, and outline the basics of observational properties of gravitational waves. Section 3 outlines fundamental aspects of the N-body integrators used in this thesis. With the theory behind the physics and code laid out, an outline of the methodology is given in section 4. Section 5 then examines the final results, followed by section 6, which concludes by providing a summary of results and mentioning possibilities for future work.
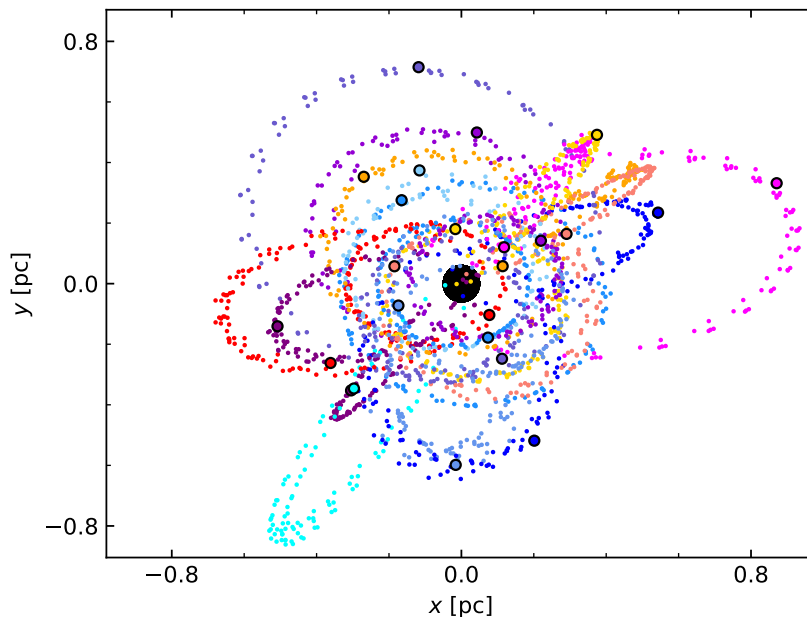
Figure 1.1: Example of a numerical simulation applying the model proposed by Ebisuzaki et al. (2001) [1]. Here, 30 intermediate-mass black holes of mass $M = 10^3 M_\odot$ (each colour representing an individual particle) reside within 1pc of a $4 \times 10^6 M_\odot$ supermassive black hole, located at the origin in black. Outlined circles show the final position of the intermediate-mass black holes, and smaller dots their corresponding trajectory mapped on the xy-plane over some simulation time.

2 Behind the Physics: Theoretical Background

2.1 Black Holes

2.1.1 Black Hole Families

Black holes (hereafter BH) make the crux of our investigation. They are celestial objects emerging naturally in the geometrical description of gravity formulated by Einstein (1916) [6]. If within a certain distance of it, its gravitational pull is so strong that not even light can escape its grasp. BHs cover a range of masses.

Stellar-mass black holes (hereafter SBH) have masses $M \lesssim 10^2 M_\odot$, where $M_\odot$ signifies one solar mass. It was a set of merging binary SBHs that, in 2016, ushered in the era of gravitational wave (hereafter GW) astronomy [23]. Lying at the other extreme, supermassive black holes (hereafter SMBH) have masses $\gtrsim 10^5 M_\odot$ and are often present at the centre of galaxies ([10]; [12]; [14]). The first-ever image of a BH, taken in 2019, was that of an SMBH lying at the core of the giant elliptical galaxy M87 [15]. More recently, the SMBH of our galaxy, Sagittarius A* (SgrA* for short), was photographed [16]. SgrA* weighs $M = (4.154 \pm 0.014) \times 10^6 M_\odot$ [24]. Interestingly, excluding the detection of a GW event leading up to the formation of a low-mass ($\sim 150 M_\odot$) intermediate-mass black hole (hereafter IMBH) [25], it is this family of BHs which remain undetected. IMBH's cover the mass range $10^2 M_\odot \lesssim M_{\mathrm{IMBH}} \lesssim 10^5 M_\odot$. These elusive objects comprise the focus of our research.

Various mechanisms have been brought forward to explain their formation. IMBHs may be the remnant of population III stars ([17]; [26]; [27]; [28]). Population III stars can grow larger than the current generation of stars since they have low metallicity and thus cannot radiate away energy as efficiently. Other ways IMBH may form is through merging of satellite galaxies with their hosts instigating collisions of SBH with the product eventually growing into an IMBH [20], or in the gas disk of active galactic nuclei (hereafter AGN) ([21]; [29]). Here, we assume IMBH form through runaway mergers at the centre of globular clusters (hereafter GC).

Runaway mergers occur in clusters due to mass segregation. This phenomenon follows from the equipartition theorem, which states that the kinetic energy of two particles will tend to equalise after an encounter. A fixed kinetic energy implies that massive objects have a lower velocity and thus cannot climb out of the potential well, sinking to the core instead. Contrariwise, lighter stars are quicker and expand their orbits to the outer regions until they find a stable orbit.

Numerical simulations have shown that in sufficiently dense clusters if collisions occur before the most massive stars undergo supernova explosions ($t \lesssim 3$ Myr), a runaway merger scenario leading to the formation of an IMBH can occur ([18]; [19]). Though the rate at which this happens is dependent on various assumptions, papers have suggested between 10% to 20% of GCs with masses $M_{\mathrm{GC}} > 10^5 M_\odot$ host an IMBH ([19]; [30]; [31]). Giersz et al. (2015) [19] found that if formed, half the simulations resulted in an IMBH with mass $M_{\mathrm{IMBH}} > 0.1 M_{\mathrm{GC}}$. Throughout the years, several GCs have become candidates for hosting IMBH ([32]; [33]; [34]; [35]), though none have had their existence definitively confirmed.

2.1.2 Formation of Supermassive Black Holes

BHs play a fundamental role in astronomy and cosmology. They are the fate of massive stars once they die and play a pivotal role in galaxy formation. They are also of great interest to theoretical physicists due to them lying at the threshold of our understanding, therefore holding the key to deciphering many of nature's greatest riddles. With GW astronomy at its early stages, many questions remain one of which are the gargantuan sizes achieved by SMBHs.

SMBHs are known to grow through gas accretion. However, the Eddington limit constrains the accretion rate while various dynamical effects, elaborated on shortly, suppress the merging time of binary objects. These mathematical limits placed on the growth rate of SMBH contradict their observations in the early Universe, for instance, J1342+0928, an $8 \times 10^8 M_\odot$ quasar at redshift $z = 7.54$ [36]. Observations of these massive objects so early into the life of the Universe tell us that there is yet unknown physics to uncover. With IMBHs lying in the mass range between SBHs and SMBHs, they become an obvious target for understanding the formation of SMBH.

Ebisuzaki et al. (2001) [1] proposed that SMBHs could form through the accumulation of mergers with IMBHs. In this scenario, while an IMBH forms at the centre of a GC through runaway mergers, the cluster sinks to the galactic core due to the drag force exerted by the wake of neighbouring stars it leaves behind it. This drag force is dynamical friction, a phenomenon first described by Chandrasekhar (1943) [37]. The timescale for which it sinks massive objects to the galactic core is [11]:

$$t_{\mathrm{df}} = \frac{1.65}{\ln \Lambda} \frac{r_i^2 \sigma}{GM} \approx \frac{19 \,\mathrm{Gyr}}{\ln \Lambda} \left(\frac{r_i}{5 \,\mathrm{kpc}}\right)^2 \frac{\sigma}{200 \,\mathrm{km\,s^{-1}}} \frac{10^8 M_\odot}{M} \tag{2.1}$$

Where $\ln \Lambda$ is the Coulomb parameter, expressed as $\ln \gamma N$ with $\gamma = 0.11$ for equal mass systems ([38]; [39]) and N being the number of stars, r_i is the initial distance

from the galactic centre the IMBH (and/or cluster) started to sink from, σ the velocity dispersion and M the mass of the object in question. Though there are various assumptions (constant Λ, σ...), as a rule of thumb when plugging in the values of the average GC circularly inspiraling inwards ($M{\sim}10^5 M_\odot$, $\ln \Lambda{\sim}10$ and using $\sigma{\sim}150$ km s^{-1} [11]), only clusters originally at $r \lesssim 500$ pc from the galactic centre reach the core within a Hubble time. This report considers the scenario where dynamical friction sources the appearance of IMBH in the inner parsec of the galaxy.

A crucial feature of the model proposed by Ebisuzaki et al. (2001) [1] is the existence of several IMBH within the galactic centre. Although dynamical friction helps clusters sink to the galactic core, the nearer one approaches the centre, the fewer field stars are in its proximity. With fewer neighbours, the IMBH experiences increasingly weaker dynamical friction and fewer scattering events which would otherwise help further deplete the sinking objects' orbital energy. The result is that the IMBH stalls out at a certain distance from the SMBH. Although stars may exchange energy with the binary if they have the correct angular momentum-energy configuration (the region being the loss cone), once scattered, they fly outside the domain. It has been found that the loss cone replenishment rate is too slow for scattering between a tertiary and a binary to be the sole instigator of merging events [40].

Stalling would be fine if it occurred at distances where GW radiation kicks in to exhaust the remaining orbital energy from the newly formed binary. However, numerical simulations show that stalling occurs at a distance roughly ten times larger than where GW radiation becomes prominent, thus implying that coalescence events exceed the Hubble time ([41]; [42]; [43]; [44]). This is the final parsec problem ([22]; [45]). With the existence of a substantial amount of IMBH in the galactic centre as suggested by the model proposed by Ebisuzaki et al. (2001) [1], encounters which alter their dynamics can encourage SMBH-IMBH merging events, thus offering a potential solution to the final parsec problem.

2.2   Clusters and the Galactic Nuclei

Dense environments such as clusters form an integral part of our analysis and are worth discussing. In general, clusters are self-gravitating stellar environments and can come in various shapes and sizes. Star clusters host $10^2 - 10^4$ stars and are irregular in shape, whereas GCs, which are roughly spherical, contain between $10^4 - 10^6$ stars [11]. Although we base our IMBH population to originate in GCs, in the context of this report, we investigate the IMBH population potentially residing in the Milky Way's (hereafter MW) nuclear star cluster

(hereafter NSC). To generalise our discussion, we use the term particles to describe the constituents of clusters. This is because the description of the global evolution of clusters is often unchanged whether it is composed of stars, IMBH or a mix of both.

NSCs are found in roughly 80% of galaxies [46] and are dense regions surrounding a central SMBH. They have masses ranging between $10^5 M_\odot \sim 10^8 M_\odot$ and densities reaching $\rho \lesssim 10^7 M_\odot$ pc^{-3} [14]. The MW's NSC weighs $2.5 \times 10^7 M_\odot$ and extends to $r \sim 10$ pc ([13]; [46]; [47]). The formation of NSCs remains a mystery, though two models are often discussed:

- In-situ formation: The high density of gas surrounding the SMBH fragment before triggering the onset of star formation ([48]; [49]; [50]). This results in the presence of a young stellar population.

- Infalling clusters: Extending from our previous discussion, as clusters sink to the galactic core and have material stripped away due to tidal forces, the disrupted stars start orbiting the central SMBH. Over time, with more clusters sinking in, everything blends into a new cluster surrounding the central SMBH ([51]; [52]; [53]). This scenario has a preference for an older stellar population.

The MWs NSC has 80% of its stellar mass composed of old ($t \lesssim 10$ Gyr) stars, 15% in stars younger than 5 Gyr and the remaining in stars formed in the last 100 Myr [54]. This diversity in the stellar population implies that both mechanisms play a role in its formation. Once formed, many complex dynamical processes shape the evolution of clusters. As we have seen with mass segregation, statistical arguments can be a helpful tool to understand their global properties, this remains the case when describing the effects of two-body relaxation.

2.2.1 Two-Body Relaxation

Two-body relaxation is a random walk process generated by weak encounters. It is an essential characteristic of clusters since weak perturbations are prevalent in these environments, even dominating the evolution of the system if you neglect stellar evolution [38]. Weak encounters are interactions where the change in a particle's velocity satisfies $\delta v \ll v$. Being a random walk process, two-body relaxation pushes the cluster towards a Maxwellian velocity distribution.

In general, for an N equal-mass system dominated by weak encounters, the two-

body relaxation acts on timescales ([11]; [38]):

$$t_{\text{rlx}} = \sqrt{\frac{r_c^3}{GM_c}} \frac{N}{8 \ln \gamma N} \tag{2.2}$$

Where r_c and M_c denote the cluster's radius and mass respectively. The logarithmic term accounts for the cumulative effect of weak encounters. In a system with a Maxwellian velocity distribution, a more precise formula is [11]:

$$t_{\text{rlx}} = \frac{2.1 \sigma r_c^2}{G\langle m \rangle \ln \gamma N} \tag{2.3}$$

Here $\langle m \rangle$ denotes the average particle mass. After a relaxation time has elapsed, the perturbations essentially cause the particles to have no memory of their original orbital parameters.

By giving the time scale in which clusters tend to a Maxwellian velocity distribution, t_{rlx} describes the timescale for particles to reach the tail end of the velocity distribution, regions in which velocities are large enough to eject from the system. Since our primary aim is to investigate the potential steady-state population of IMBHs in the NSC, understanding the timescales of mergers or ejections is critical.

We can refine the expression above to better fit our investigation. Assuming an isothermal velocity dispersion:

$$\sigma = \frac{v_c}{\sqrt{3}} = \sqrt{\frac{G\langle m \rangle N}{3r_c}} \tag{2.4}$$

Where v_c is the circular orbital velocity. Taking our own cluster as an example (section 4), we adopt $r_c = 0.4$ pc[1] and $\langle m \rangle = M_{\text{IMBH}} = 10^3 M_\odot$. Plugging these values and equation 2.4 into equation 2.3:

$$t_{\text{rlx}} = 2.1 \sqrt{\frac{N r_c^3}{G\langle m \rangle}} \ln^{-1}(\gamma N) \tag{2.5}$$

$$= 170 \text{ kyr} \frac{\sqrt{N}}{\ln \gamma N} \tag{2.6}$$

For a typical cluster population of 10^5 stars, the relaxation time is $t_{\text{rlx}} \approx 6$ Myr.

[1] Though our clusters are initialised with $r_c = 0.2$ pc, using AMUSE, the half-mass radius (the enclosed radius which contains half the total cluster mass) was found to be roughly 0.4 parsecs.

Continuing our derivation, following ([11]; [38]) we define the particle loss-rate as:

$$\frac{dN}{dt} \equiv -\frac{\beta N}{t_{\text{rlx}}} \tag{2.7}$$

Where β is the evaporation rate constant found to be $\beta \approx \frac{1}{300}$ in an isolated cluster ([11]; [38]). Evaporation is a process attributed to weak encounters, which, as already mentioned, shift the cluster to follow a Maxwellian velocity distribution over time, thus providing a mechanism for stars to reach the tail end of the velocity distribution and escape the cluster. Inverting the expression and subbing in for β and equation 2.6, the typical time for a cluster to lose a particle becomes:

$$t_{\text{loss}} = -\frac{t_{\text{rlx}}}{\beta N} \tag{2.8}$$

$$= 51.1 \text{ Myr } \left(\sqrt{N}\ln(\gamma N)\right)^{-1} \tag{2.9}$$

Although this expression dictates the approximate timescale for particles to become unbound from their host, this also represents the timescale for collision events and thus reflects the overall particle loss. This is reasoned because weak two-body encounters occur more often for particles that have high eccentricities since these are the particles that travel through the denser, heavily populated core more often.

More intuitively, in some instances, the orbital parameters may be just right for the particle to escape. Here, the accumulated perturbations experienced induce an increase in the particles' eccentricity. As stated already, increasing the eccentricity means that the particle often finds itself in the core. At this point, encountering a particle could cause a change in its orbital parameters such that it now follows an ejection trajectory. In other instances, plunging into the core can result in a merger with the SMBH. As we will see, merging events are also heavily influenced by the particles' eccentricity (see equation 2.24). Considering this, we expect the extracted particle loss timescale found in our simulations to be within an order of magnitude of equation 2.9.

Even so, it is worth mentioning that here we neglect the typical collisional timescale and assume that the equation reflects merging timescales due to the similar mechanisms ejections and mergers require to occur. We motivate this omission following a simple calculation using the collisional timescale [11]:

$$t_{\text{coll}} = \frac{1}{n\Sigma v} \tag{2.10}$$

$$= 0.2\left(\frac{v_{*,\text{esc}}}{v}\right)^4 t_{\text{rlx}} \ln N \tag{2.11}$$

Here, n is the number density, approximated as $n = \frac{N}{r^3}$, Σ the collisional cross-section $\Sigma = 4\pi r_*^2$, v the circular velocity of the system, $v = \sqrt{\frac{GM}{r}}$, while $v_{*,\text{esc}} = \sqrt{\frac{GM_*}{r_*}}$, is the escape velocity at the surface of a subject particle. Plugging in values similar to our simulated system (see section 4):

$$N = 20, \qquad M = M_* = 4 \times 10^6 M_\odot, \qquad r_* = r_{\text{ISCO}} = 51 R_\odot, \qquad r = 0.4 \text{ pc}$$

$$\therefore v_{*,\text{esc}} = \sqrt{\frac{GM_{\text{SMBH}}}{r_{\text{SMBH}}}} = 1.22 \times 10^8 \text{ m s}^{-1} \tag{2.12}$$

$$v = \sqrt{\frac{Gm}{r}} = 2.08 \times 10^5 \text{ m s}^{-1} \tag{2.13}$$

using these and equation 2.2, equation 2.11 becomes:

$$t_{\text{coll}} = 1.11 \times 10^8 \text{ Myr} \tag{2.14}$$

From this we see that $t_{\text{coll}} \gg t_{\text{loss}}$. Though the example has several assumptions (namely adopting a Newtonian approach though clearly equation 2.12 deserves a relativistic description), it helps push the point that t_{loss} is the expression to model our system off.

We emphasise once more: weak encounters dominate the global evolution of clusters. Their cumulative effect will cause a steady outflux of particles, be it from ejections or merging, due to them enhancing orbital eccentricities and their natural tendency to settle clusters into a Maxwellian velocity distribution. We now shift our discussion to the complex dynamics present during close encounters since these form a vital part of GW astronomy and make for interesting systems.

2.2.2 Binary and Hierarchical Systems

Though encounters between IMBH often result in transient fly-by events, a binary or hierarchical system may also form. Binary and hierarchical systems are potential sources of ejection events. They influence overall cluster evolution and could also source GW radiation (section 2.2.3).

We start our discussion with binary systems. Binary systems are composed of two particles and often need the presence of a third particle to carry away any excess kinetic energy before forming [38]. In dense clusters such as the NSC, this occurs relatively frequently. Binary systems can be either 'hard' or 'soft'.

Hard binaries are systems whose orbital binding energy exceeds the average kinetic energy of stars in the same environment. That is, they satisfy [55]:

$$a < \frac{Gm}{4\sigma^2} \tag{2.15}$$

Here, a is the binary's semi-major axis, m the mass of the more massive body and σ the velocity dispersion of the local environment.

By definition, during an encounter between a hard binary and a third particle, the binary will harden (feel a shrinking of its semi-major axis). By hardening, the binary releases binding energy in the form of potential energy to the environment, subsequently increasing the kinetic energy of the tertiary particle [56]. Contrariwise, encounters between a third particle and soft binaries often disrupt the system, after which several different outcomes may occur. Keeping our discussion simple, we keep our focus on hard binaries. The velocity of the ejected tertiary particle after interacting with a hard binary is expressed as [45]:

$$v \approx \sqrt{\frac{G(m_1 + m_2)}{a}} \tag{2.16}$$

Where m_1 and m_2 are the binary's mass components. Plugging values of $m_1 = m_2 = 10^3 M_\odot$ and $a = 10^{-2}$ pc (roughly 2000 AU), we see that the ejected tertiary can reach speeds of $\sim$30 km s^{-1}. If we plug the same values for an IMBH-SMBH binary and use the mass of SgrA* for the SMBH, this value exceeds 1000 km s^{-1}, allowing for objects unbound from the MW.

A similar process is the Hills mechanism [57]. Here, a binary system and a central SMBH interact. As the binary loses orbital energy due to GW or tidal forces and approaches the SMBH, one of the IMBH particles will bind with the SMBH ejecting the other at speeds over 1000 km s^{-1}. Koposov et al. (2019) [58] confirmed this phenomenon after discovering a hypervelocity star (hereafter HVS) following a trajectory radially outwards from the galactic centre with velocity 1755 ± 55 km s^{-1} in the galactic frame.

The dynamics of the various ejection and encounter outcomes are complex, and providing a thorough explanation for all lies outside the scope of the report (see instead: [59]; [60]; [61]; [62]; [63]). However, in general, three-body interactions allow for the exchange of the binary's internal binding energy into the escapee's kinetic energy allowing for large velocities. If the interaction is between three (or two) unbound particles, this ejected velocity is drastically smaller as no hardening occurs, which would otherwise release potential energy into the local environment before getting converted into the tertiary's kinetic energy.

Perhaps counterintuitively, gravitational systems have negative heat capacities, meaning that if a binary (or hierarchical) system releases potential energy into the cluster, the cluster gets colder. We can see this behaviour arise following statistical arguments. From thermodynamics, a system's total kinetic energy equals:

$$K_{E,\text{tot}} = \frac{1}{2}mv^2 = \frac{3}{2}Nk_B\langle T\rangle \tag{2.17}$$

Where N the number of bodies present in the system and $\langle T\rangle$ the particles' average temperature. The virial theorem, which describes a stable system of discrete particles, relates the system's kinetic energy with its potential energy:

$$K_{E,\text{tot}} = -\frac{1}{2}P_{E,\text{tot}} \tag{2.18}$$

Therefore, the system's total energy is:

$$E_{\text{tot}} = K_{E,\text{tot}} + P_{E,\text{tot}} \tag{2.19}$$

$$= -\frac{3}{2}Nk_B\langle T\rangle \tag{2.20}$$

Using the definition of heat capacity, this means:

$$C \equiv \frac{dE}{d\langle T\rangle} = -\frac{3}{2}Nk_BT \tag{2.21}$$

Negative heat capacity in gravitational systems means that, although encounters of particles with binary or hierarchical systems release binding energy into the cluster and heating it, it inevitably results in its cooling as the system expands. This phenomenon is intricately connected to mass segregation discussed earlier.

As alluded to, a stable three-body system (hierarchical system) may also form. Hierarchical systems contain an inner binary with mass components m_1 and m_2 and semi-major axis a_{in}, and a third particle orbiting the inner binary with a larger semi-major axis ($a_{\text{out}} \gg a_{\text{in}}$) and mass m_3. This third particle orbiting the inner binary forms the outer binary.

Though they usually aren't sustainable due to weak and the occasional strong encounters disrupting the system, Mardling and Aarseth (2001) [64] derived a condition for a stable hierarchical system. Mathematically, this criterion is:

$$\frac{a_{\text{out}}}{a_{\text{in}}} > \frac{2.8}{1-e_{\text{out}}}\left(1+\frac{m_3}{m_1+m_2}\right)\left(1+\frac{e_{\text{out}}}{\sqrt{1-e_{\text{out}}}}\right)^{2/5} \tag{2.22}$$

11

where e_{out} is the eccentricity of the outer binary. In such a system, resonant effects can increase the eccentricity to order of unity, enhancing the merger rate. A notable example of a resonant phenomenon is the Kozai-Lidov ([65]; [66]; [67]). Here, the oscillation occurs if the inclination between the inner and outer binary exceeds a critical value and acts on timescales much larger than the orbital period [68]:

$$t_{LK} = P_{in} \left(\frac{m_1 + m_2}{m_3} \right) \left(\frac{r}{a_{in}} \right)^3 (1 - e_{out}^2)^{3/2} \qquad (2.23)$$

where P_{in} is the inner binary's orbital period, and r is the distance from the inner binary to the tertiary star forming the outer binary. This effect gets suppressed if the particles forming the inner binary have equal masses. As we will see in section 4, this is the case for our modelled IMBH particles, and thus, the effect can only arise if the SMBH forms one of the inner binary particles [69]. It is hard to predict how the Kozai-Lidov effect influences our own simulations. However, given the density of the system simulated, one can expect that hierarchical systems rarely live long enough for them to play a defining role in growing the eccentricity of the particles compared to weak perturbations.

Given GWs act as an energy sink source, one expects that modelling this relativistic effect can encourage the formation of binary and hierarchical systems since it may help carry away excess kinetic energy from a prospective binary akin to the role of a tertiary particle. Indeed, this is the case observed in Rodriguez et al. (2018) [70]. As we have seen, this may then encourage both ejections, and under the correct configuration, merging events.

2.2.3 Gravitational Waves

In dense clusters such as the MW NSC, if the presence of IMBH is abundant, observations of GWs can be especially prevalent. Recording radiation emitted from SMBH-IMBH systems is the main aim of the future interferometer Laser Interferometer Space Antenna (LISA) [71], which will be capable to detect these signals emitted from sources throughout the Universe. The field of GW astronomy is rich, and its detailed description lies outside the scope of the current paper (see i.e [71]; [72]; [73]; [74]). Here, we describe the essentials needed when forecasting GW events present in our simulated NSC environment.

The vast amount of energy expended during the coalescence of an IMBH-IMBH or SMBH-IMBH merger produces ripples in space-time which could be measured using state-of-the-art interferometry techniques. The timescale for orbital decay of

a binary sourced by GW radiation to conclude in the inevitable merger is [75]:

$$t_{GW} = \frac{5}{256} \frac{c^5}{G^3} \frac{a^4(1-e^2)^{7/2}}{\mu(m_1+m_2)^2} \tag{2.24}$$

where m_1, m_2 are the masses of the two bodies merging, a and e the systems semi-major axis and eccentricity, c the speed of light and μ, the reduced mass given as:

$$\mu = \frac{m_1 m_2}{(m_1 + m_2)} \tag{2.25}$$

Note the $t_{GW} \propto a^4(1-e^2)^{3.5}$ proportionality. This relation has been hinted at before and shows the extent boosting the orbital eccentricity and hardening (reducing a) has on the rate of GW events.

GW events may be categorised into three distinct phases; the inspiral phase, the coalescence (merger) phase and the ringdown phase [72]. In our context, we will often encounter inspiral events though the coalescence phase constitutes one of the simulations' stopping conditions (see section 4). During an inspiral event, the emitted frequency of the GW is ([76]; [77]):

$$f_n = \frac{1}{\pi} \sqrt{\frac{G(m_1+m_2)}{a^3}} \frac{(1+e)^{1.1954}}{(1-e^2)^{1.5}} \tag{2.26}$$

m_1 and m_2 are the masses of the inspiralling objects forming a binary, a their semi-major axis and e their eccentricity. The subscript n denotes the nth harmonic of the GW radiation where $f_n = n f_{orb}$ and f_{orb} is the rest-frame GW frequency.

Since the Universe is expanding, if the source originates from a redshift z away, the rest-frame frequency relates to the observational frequency by $f_n = (z+1)f_{n,z}$. Note that the expression cannot record hyperbolic trajectories where $e > 1$ due to the presence of the $(1-e^2)^{1.5}$ term, meaning many of the potential signals are left unrecorded in our analysis.

Plugging in values for an SMBH-IMBH event occurring at the core of the MW ($e = 0.3$ and $a = 10^{-4}$ pc), the emitted GW frequency is $f = 1.95 \times 10^{-6}$ Hz and falls right outside the detectable frequency range of LISA, though it is still observable by the proposed GW interferometer μAres [78]. Even so, although the frequency may lie within the observable range, the power needs to be strong enough to be detectable.

The extent that GWs distort space-time in the observer frame, or using GW

13

astronomy jargon, the strain, is expressed as [79]:

$$h_{c,n}^2 = \frac{2}{3\pi^{4/3}} \frac{G^{5/3}\mathcal{M}_{c,z}^{5/3}}{c^3 D_L^2} \frac{1}{f_{n,z}^{1/3}(1+z)^2} \left(\frac{2}{n}\right)^{2/3} \frac{g(n,e)}{F(e)} \tag{2.27}$$

Here, $\mathcal{M}_{c,z}$ is the chirp mass given as:

$$\mathcal{M}_{c,z} = \mathcal{M}_c(1+z) \tag{2.28}$$
$$= \frac{(m_1 m_2)^{3/5}}{(m_1 + m_2)^{1/5}}(1+z) \tag{2.29}$$

D_L the luminosity distance, $g(n,e)$ a harmonic and frequency-dependent function given in Peters and Matthews (1963) [76], and $F(e)$ an eccentricity-dependent function given as:

$$F(e) = \frac{1 + (\frac{73}{24}e^2) + (\frac{37}{96}e^4)}{(1 - e^2)^{7/2}} \tag{2.30}$$

The lifetime of the GW emission may often be much longer than the interferometer observational lifetime, t_{obs}, meaning only a fraction of the power emitted is measured. To account for this, one has to multiply equation 2.27 by a factor $\min\{1, \dot{f}_n \frac{t_{\text{obs}}}{f_n}\}$ ([79]; [80]; [81]). Here $\dot{f}_n$ is the time derivative of the frequency, representing the frequency band swept by the source during the mission lifetime. Its expression is given as [79]:

$$\dot{f}_n = \frac{96n}{10\pi} \frac{(G\mathcal{M}_c)^{5/3}}{c^5} (2\pi f_{\text{orb}})^{11/3} F(e) \tag{2.31}$$

With the fundamentals of the theory laid out, we now shift our discussion to *N*-body simulations and computational astrophysics in the gravitational regime.

3 Behind the Code: Gravitational N-body Simulators

This thesis uses the Astronomical Multipurpose Software Environment[2] (hereafter AMUSE) ([56]; [82]; [83]; [84]). AMUSE is an astrophysical simulation environment which includes a wide range of astrophysical fields, namely gravitational dynamics, hydrodynamics, stellar evolution and radiative transport. Its main strength is that it allows one to combine different physical regimes coherently, allowing for multi-scale and multi-physics simulations. With a range of community codes at its disposition, AMUSE is a user-friendly software able to investigate complex astrophysical questions.

In this report, we focus our attention purely on gravitational dynamics. This section provides the reader with an introduction to the fundamentals behind the algorithm (or integrator) used to solve the gravitational system. We begin by discussing the basics of Newtonian and post-Newtonian gravity before delving into the various integrators used, Hermite and HermiteGRX (hereafter GRX).

3.1 Newtonian Gravity

In 1687, Newton published the *Philosophiæ Naturalis Principia Mathematica* [85]. Within it, he proposed the following law to describe the force of gravity, F_g:

$$F_g = m_1 \ddot{\vec{r}}_1 = Gm_1 \sum_{j \neq i}^{N} \frac{m_j}{r_{ij}^2} \tag{3.1}$$

Where G is the gravitational constant, m_j the mass of particle j, $r_{ij} \equiv |r_i - r_j|$ the relative distance between particle i and particle j, and N the number of particles in the system. Newton's law forms a set of coupled, ordinary differential equations. Using it, we can extract the gravitational force felt by a particle by summing over all the contributions exerted by the $(N - 1)$ others present. Although the equation can be solved analytically for $N = 2$ systems, in 1882, Henri Poincaré [86] showed that this no longer holds for $N > 2$ systems due to their chaotic nature (see Appendix A). Since these systems are ubiquitous in nature, astronomers and physicists alike resort to numerical methods and N-body simulators to investigate the properties of many-bodied systems.

---

[2] amuse.readthedocs.io/

In general, *N*-body simulators compute the gravitational force exerted onto each particle using equation 3.1 before calculating the particles' position and momentum at a given time step. Afterwards, it synchronises the information and repeats the procedure for the following time step until it has reached its endpoint.

There are many different ways of achieving this. Over the decades, different integrators have been developed in a seamlessly ever-lasting dance trying to balance computational efficiency with physical accuracy. Integrators can range in applications depending on their properties; from simulating galactic dynamics to solving the long-term evolution of planetary systems. Since `Hermite` simulates $N \lesssim 10^4$ systems in an efficient manner [56], we use its algorithm in this investigation for the Newtonian case.

Additionally, some integrators go beyond solving equation 3.1 and model relativistic effects. Oftentimes, solving the complete general relativistic equations of gravity [6] is overkill and computationally demanding. To preserve relativistic effects and reduce the computational load, some integrators use the post-Newtonian approximation (hereafter PN).

3.2 Post-Newtonian Gravity

PN expansion adopts the geometrical description of gravity by expanding Newtonian gravity to include minute perturbations in flat Euclidean space. These perturbations signify weak gravitational fields in and around bodies and represent the geometric nature of gravity. The approximation is modelled from Taylor expanding the Einstein field equations in powers of c^{-n} where the *x*th ordered term corresponds to the $\frac{n}{2}$ power. More explicitly, the first PN term (1PN) corresponds to terms scaled by a factor c^{-2}, the second PN term (2PN) with a c^{-4} dependency, and so on. The expansion thus takes the form:

$$\vec{r} = \vec{r}_N + \frac{1}{c^2}\vec{r}_{1PN} + \frac{1}{c^4}\vec{r}_{2PN} + \frac{1}{c^5}\vec{r}_{2.5PN} + \mathcal{O}(c^{-6}) \tag{3.2}$$

Where $\vec{r}_N$ represents the unperturbed Newtonian terms. `GRX`, provides the user with several different PN approximations (see [40]). In our context, we incorporate the 2.5PN terms since this is when GWs emerge.

When modelling the 2.5PN terms, `GRX` makes use of an adapted form of the complete Einstein-Infeld-Hoffman (EIH) [87] equations of motions, who themselves describe the equation of motion in a weak field to first order.

The EIH equations were the first non-trivial solution for a system composed of *N* Schwarzschild BH. A Schwarzschild BH, defined by the Schwarzschild metric, is

16

the first non-trivial solution to Einstein's field equations (Schwarzschild (1916) [88]) and describes the geometry of spacetime outside an electrically neutral, spherical mass with zero angular momentum. This description ensures that the EIH equations represent an accurate portrayal of those simulated here since we neglect the intrinsic spin and charge of BHs. Even so, as successful as it is, incorporating double summations within the EIH equations causes it to be computationally taxing when modelling three-body encounters in large N-body systems.

Will (2014) [89] found that by modifying the equation of motion through Taylor expanding with respect to a second investigation-dependent variable, one can remove the highest-ordered summation over pairs of particles without loss of generality. In our case of BH clusters, the secondary expansion is with respect to the mass ratios of the IMBH and SMBH. Ideally, applying this approximation reduces the scaling of the algorithm from $\mathcal{O}(N^3)$ to $\mathcal{O}(N^2)$. However, although GRX applies this modification, it conserves the second-to-highest-ordered pair summations due to their necessity in energy conservation [40] and influence on dynamical effects such as the suppression of resonant relaxation [89]. These double summations, also named cross terms due to their $m_i m_j$ dependencies, represent the coupling between the potentials of N particles and incorporating them causes GRX to scale as $\mathcal{O}(N^3)$.

Resonant relaxation is a phenomenon where repeated interactions within a system of low-mass particles orbiting around a BH induce torques on one another, potentially increasing a particle's orbital eccentricity while keeping its orbital energy constant [90]. Due to being a resonant effect, these torques accumulate in time and generate large orbital eccentricities in the long-term evolution. Given the large timescales for our system (recall $t_{\text{loss}} \approx 50$ Myr for our sample cluster), secular effects such as this can play a significant role in the overall dynamics of the system, encouraging merging events and so it is necessary to consider them in our investigation.

PN cross terms suppress this effect since it introduces a shift on the particle's semi-major axis over time, removing the tendency for torques to constructively accumulate, but rather destructively interfere with one another. Nevertheless, one should keep in mind that there are other phenomena present. As pointed out by Naoz et al. (2013) [69], if the 1PN precessing timescales are much larger than the Newtonian secular timescales, eccentricities can grow to unity, compensating for resonant suppression induced by the cross-terms. Given the chaotic nature of the dense system simulated here often disrupting sustained systems for which these secular effects emerge, we expect that the major differences in Hermite and GRX

will be due to the 2.5PN term. As mentioned before, this is when GWs start to emerge. Introducing an energy sink to the system, GW merging events are encouraged as the consistent depletion of a particle's orbital energy causes it to sink into the potential well until they cross the event horizon.

We've added the equation of motion used by GRX under Appendix B (equation B.1) for the reader's convenience. Note that it neglects 2PN terms, though this doesn't play a significant role in the final results. This is because the 2PN term introduces a shifting perihelion, something accounted for to an extent by the 1PN term. A secondary effect described by the 2PN term is the flattening of the poles due to rotation and tidal forces [91]. However, this effect starts to play a role only when the particles separation vector $\vec{r}_{ij}$ is nearing coalescence or has already merged based on our definition of the collisional radius (see section 4).

There is an abundance of papers focused on PN expansion and its numerical implementation (i.e [40]; [72]; [89]; [91]; [92]; [93]), for our current paper it suffices to understand the role each PN term plays in the dynamics of particles. In general, the following effects arise from the PN terms used in the selected GRX algorithm:

- 1PN gives corrections to the orbits of particles. More explicitly, these terms correspond to the periastron shift of a body's orbit.

- 2.5PN is when GWs emerge. This forms an essential part of the current investigation as we wish to record and forecast the GW signals of any potential BH clusters existing in galactic cores. Note that with an energy-sink source in the form of gravitational radiation (see Appendix B), the system no longer conserves energy [93].

Though higher-order terms exist, their effects lie outside the scope of our paper [91]. Given the context of our question, this report uses the Hermite integration scheme [94] as its Newtonian algorithm and GRX for the PN case. As mentioned before, these schemes provide the user with reliable results in a computationally efficient manner, allowing one to simulate many-body systems as is the case for a hypothetical IMBH cluster residing in the heart of galaxies. We will test and compare results extracted from either algorithm to see the role PN terms play in modelling these relativistic systems. When not comparing the formalisms, results from GRX are analysed since they provide a more accurate portrayal of nature.

The remaining subsections of this chapter provide an overview of various fundamental properties of the Hermite and GRX algorithms. The curious reader is directed to ([40]; [94]; [95]; [96]) if they wish for a more thorough understanding.

18

3.3 Hermite and HermiteGRX

3.3.1 Predict-Evaluate-Correct Scheme

Both `Hermite` and `GRX` use a fourth-order numerical method to solve ordinary differential equations implicitly. This is done by solving the following:

$$y(t + \delta t) = y(t) + \frac{y'(t) + y'(t + \delta t)}{2}\delta t + \frac{y''(t) - y''(t + \delta t)}{12}(\delta t)^2 + \mathcal{O}(\delta t^5) \quad (3.3)$$

The primes denote time derivatives and δt the time step. The implicit nature of the scheme is clear since, at a particular time step, one requires information about the system at that same time step. To account for this, the integrators use a fixed-point iteration until the solution converges. Implicit integration schemes generally are more stable than their explicit counterparts at the detriment of being more computationally intensive [56].

The fourth-order nature implies an energy error scaling as $\delta E \propto \delta t^4$. Conserving energy is essential if a simulation wishes to represent reality since this is a fundamental law of nature. Checking for energy conservation is often used as a preliminary check to see whether a given algorithm provides physically meaningful results. In this report, all simulations using `Hermite` satisfied the energy error $\frac{E(t_f) - E(t_0)}{E(t_0)} \lesssim 10^{-2}$ where $E(t_f)$, $E(t_0)$ denote the final and initial energy respectively with most lying in the 10^{-4} range (see Appendix C for a short discussion on energy errors). Due to the 2.5PN term being non-conservative, the same cannot be said for `GRX`. However, upon turning off the 2.5PN term and simulating a few runs, simulations did not exceed an energy error of $\sim 3 \times 10^{-1}$.

The following describes the `Hermite` algorithm:

1. A prediction is made on the position and velocity of a given particle by solving:

$$\vec{r}_{i+1}^{\text{pred}} = \vec{r}_i + \vec{v}_i \delta t + \frac{1}{2}\vec{a}_i^{\text{pred}}(\delta t)^2 + \frac{1}{6}\vec{j}_i(\delta t)^3 \quad (3.4a)$$

$$\vec{v}_{i+1}^{\text{pred}} = \vec{v}_i + \vec{a}_i \delta t + \frac{1}{2}\vec{j}_i(\delta t)^2 \quad (3.4b)$$

where r, v, a, j are the position, velocity, acceleration and jerk ($j \equiv \dddot{a}$) of the particle at time step t_i.

2. It then predicts the acceleration and jerk of the particle using [95]:

$$\vec{a}_{i+1} = G \sum_{\substack{j \neq i}}^{N} m_j \frac{\vec{r}_{ij}}{|\vec{r}_{ij}|^3} \tag{3.5a}$$

$$\vec{j}_{i+1} = G \sum_{\substack{j \neq i}}^{N} m_j \left(\frac{\vec{v}_{ij}}{|\vec{r}_{ij}|^3} + \frac{3(\vec{v}_{ij} \cdot \vec{r}_{ij})}{|\vec{r}_{ij}|^5} \right) \tag{3.5b}$$

Where $\vec{v}_{ij} = |\vec{v}_i - \vec{v}_j|$ is the relative velocity between two particles. Note how equation 3.5a uses the Newtonian description of gravitational force and sums the force exerted by each particle on a specific individual.

3. Using the predicted values of the jerk and acceleration, the particle's position and velocity get corrected in the following fashion:

$$\vec{v}_{i+1}^{\text{corr}} = \vec{v}_i + \frac{1}{2}(\vec{a}_i + \vec{a}_{i+1}^{\text{pred}})\delta t + \frac{\vec{j}_i - \vec{j}_{i+1}^{\text{pred}}}{12}(\delta t)^2 \tag{3.6a}$$

$$\vec{r}_{i+1}^{\text{corr}} = \vec{r}_i + \frac{1}{2}(\vec{v}_i + \vec{v}_{i+1})\delta t + \frac{\vec{a}_i - \vec{a}_{i+1}^{\text{pred}}}{12}(\delta t)^2 \tag{3.6b}$$

4. After doing this for every particle. Steps 1, 2 and 3 are repeated at each increment of time until the simulation reaches its end time.

This procedure is denoted as a predictor-evaluator-corrector scheme (sometimes called the velocity Verlet method or Leapfrog method [97]). We note that although GRX adopts different formulas for which it computes the properties of each particle, it follows the same predictor-evaluator-corrector procedure.

3.3.2 Adaptive time steps

Both integrators use shared, variable time steps to reduce numerical errors. It is applied in the following fashion:

$$\delta t = \eta \min_{i,j \neq i} \left(\frac{|\vec{r}_{ij}|}{|\vec{v}_{ij}|}, \frac{|\vec{r}_{ij}|}{|(m_i + m_j)\vec{a}_{ij}|} \right) \tag{3.7}$$

The adaptive time step scheme implemented has a physically meaningful basis since it's dependent on the system's minimum inter-particle collisional timescale. The user has the freedom to choose their time step parameter η, and, although $\eta = 0.1$ is sufficient most of the time [98], a value of $\eta = 0.01$ is adopted here due to it giving a nice balance between numerical accuracy and computational time.

Utilising an adaptive time step scheme helps reduce energy errors present in the simulation and also benefits results by better resolving close encounters.

We note that time symmetrisation is essential to energy conservation [99], especially when simulating the long-term evolution of systems. Though the mechanism isn't adopted here, future projects with more time to conduct the investigation should incorporate it.

3.3.3 Regularisation

Notice from equations 3.5a and 3.5b that as a particle separation vector approaches zero, both the acceleration and jerk diverge. Though this may reflect reality, the feature plagues *N*-body simulation since a diverging force results in the computer needing smaller and smaller time steps to resolve the system accurately, essentially stopping the integration scheme at singularity. We see this also reflected in equation 3.7 since as a particle's separation approaches the singularity, that is $\vec{r}_{ij} \rightarrow 0$, our adaptive time step approaches zero. To work around this problem, `Hermite` and `GRX` use regularisation. We direct the reader to ([40]; [94]; [95]; [96]; [100]; [101]) if they wish for a more comprehensive discussion.

In essence, the regularisation technique uses similar ideas to those of Kustaanheimo-Stiefel regularisation (hereafter KS regularisation) [100]. KS regularisation moulds the equations of motions to take the form of a harmonic oscillator, thereby removing the singularity through a re-mapping of coordinates. This mapping is more complicated for the PN formalism due to its acceleration being velocity dependent [102] and thus `GRX` utilises quaternions as its map [103].

Before proceeding to the methodology adopted in our simulation, we reiterate just how significant a role regularisation plays. By removing the singularity present in our accustomed form of the equations of motion, we allow the computer to perform better during close encounters and better conserve energy (see figures 2 and 3 of Por (2014) [40]), a vital feature to understand the reliability of *N*-body simulations. Modelling at best as possible close encounters is especially vital in a dense system such as NSCs since these are environments where such events are prominent. Furthermore, we recall that merging events are sourced by highly eccentric pairs (recall equation 2.24), who, due to their near-radial path, experience close encounters. This tendency makes regularisation essential to our investigation since these same mergers form a possible outcome of our simulations.

4 Methodology

As mentioned at the beginning of section 3, we use `AMUSE` and its two community codes `Hermite` and `GRX` to run our simulations. The simulations are conducted on the ALICE computing resources provided by Leiden University.

4.1 Intermediate Mass Black Hole Infall Rate

Due to the lack of information, it is not yet possible to model our environment with the correct IMBH in-fall rate to the galactic centre. Many papers assume IMBH to fall into the galactic core at a rate of $\tau \sim 1$Gyr ([2]; [3]; [4]; [5]) on the basis that GCs sinking into the galactic core form the MW's NSC. In this scenario, however, they assume that the densest GCs, the ones where IMBH may form, are untouched by tidal forces exerted by galactic potential and, therefore, can deposit a significant fraction of their mass into the NSC. Given the mass of the NSC, this limits the total number of GCs formed and, subsequently, the IMBH population.

Instead, we follow the results shown in figure 4 of Portegies Zwarte et al. (2006) [31] and discussed in Gerhard (2001) [104], in that even the densest clusters have a substantial amount of its material dissipate into the galactic environment due to tidal forces before it reaches the inner few parsecs of the galactic centre. Doing so allows for a larger IMBH population residing in the galactic centre. To estimate the steady-state population of IMBH, we take the deduced infall rate found in Portegies Zwarte et al. (2006) [31], that is, $\tau = 7$ Myr IMBH^{-1}.

4.2 Initial Conditions

For `Hermite`, we run simulations consisting of $10 \leq N_{\mathrm{IMBH}} \leq 100$ IMBH's separated in increments of ten while `GRX` covers $10 \leq N_{\mathrm{IMBH}} \leq 40$, separated in increments of five. Being chaotic by nature, N-body systems are sensitive to initial conditions and random numerical errors. To extract physics we are confident reflect the true phase-space configuration of the system, we fix the initial configuration and run the system 20 and 40 times per population using `Hermite` and `GRX` respectively, basing our analysis on the bulk statistics.

Although both `GRX` and `Hermite` are deterministic such that identical simulations will yield identical results, the use of different combinations of nodes on the ALICE cluster once simulating the system will introduce random numerical errors, changing the outcomes between individual simulations. When testing the bulk statistics of simulations run with identical conditions and those run with

different initial conditions, the same global trends and values were found, signifying the strength of bulk statistics when conducting N-body simulations.

The reduced populations investigated with GRX are motivated by two factors. The first comes from the shortened merging times (see section 5.2), entailing that larger populations lie nowhere near the needed stability time to be classified as a steady-state population. The second reason is due to the GRX scaling as $\mathcal{O}(N^3)$.
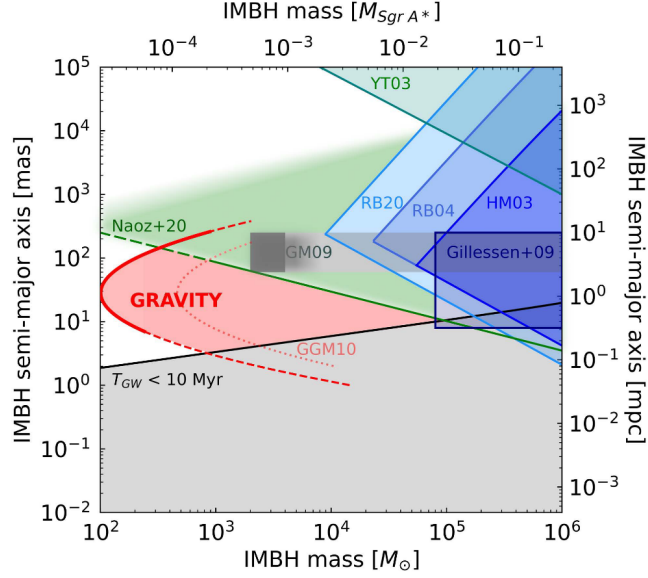

Figure 4.1: Shaded regions are regimes excluding the existence of an IMBH. Constraints are found by Yu and Tremaine (2003)[105], Reid and Brunthaler (2004) [106], Gualandris and Merritt (2009) [107], Naoz et al. (2020) [108], Reid and Brunthaler (2020) [109] and the Gravity collaboration (2020) [110]. Figure courtesy of [110].

We select our initial conditions based on various observational constraints. The spatial distribution is sampled from a Plummer sphere [111] of radius 0.25 pc, and their velocities from an isothermal sphere with velocity dispersion $\sigma_{\text{disp}} = 150$ km s^{-1} following Ghez et al. (1998) [9]. Furthermore, the code moves any particle within 0.15 parsec of the centre to a shell of $0.15 < r_{\text{SMBH}}$ [pc]< 0.35 keeping in mind the other IMBH present. The cluster radius and IMBH mass satisfy the constraints of the galactic centre placed by various research (see figure 4.1 above).

Although the Bahcall-Wolf distribution [112] is the theoretical spatial distribution of particles surrounding a SMBH, a Plummer model was chosen thanks to its straightforward implementation in AMUSE and the non-observation of a Bahcall-Wolf cusp in galactic centres. Each IMBH has mass $M_{\text{IMBH}} = 10^3 M_{\odot}$, a

value taken from Portegies Zwarte et al. (2006) [31] who found it to be the average IMBH mass for the population residing within $r \leq 10$pc of the SMBH. The central SMBH mimics that residing in the centre of our galaxy and has mass $M = 4 \times 10^6 M_\odot$ ([113]; [114]). Finally, we do not implement any intrinsic spin on the BHs and virialise the system before running the code to ensure that the system starts in a steady state.

4.3 Simulation Parameters

After configuration, the code will integrate the system in time steps of $\delta t = 10^3$ years and $\eta = 10^{-3}$ (recall equation 3.7) until one of the following is satisfied:

1. The simulation exceeds the maximum simulation time, $t_{\text{end}} \equiv 100$ Myr.

2. An IMBH particle gets ejected from the system.

3. A merging (IMBH-SMBH or IMBH-IMBH) event has occurred.

The first criterion has a large value as it helps reduce the number of simulations reaching the maximum time limit but still provides decent resolution of the simulation with snapshots of the system every 1000 years. The latter two conditions require further elaboration but in essence, stopping the simulation after any particle loss allows us to extract the steady-state lifetime of a particular population.

4.3.1 Stopping Conditions: Ejection Events

One possible way to lose an IMBH in the galactic core is through ejections. As we saw in section 2.2, this can occur from various mechanisms namely close encounters inducing perturbations of the order $\delta v \approx v$, or from the countless weak perturbations which accumulate until a slight nudge causes the particle to pass a critical threshold. An ejection occurs once the following four criteria are satisfied:

1. $K_E > |P_E|$ where K_E is the particle kinetic energy and P_E its potential energy.

2. The particle lies at a distance $|r| > 2.00$ pc from the cluster's centre of mass.

3. The particle is moving away from the cluster. That is, $\vec{r}_{ij} \cdot \vec{v}_{ij} > 0$ where $\vec{r}_{ij}$ and $\vec{v}_{ij}$ denote the positional separation and the velocity with respect to the cluster's centre-of-mass frame of reference.

4. The particle is on a hyperbolic trajectory with respect to the centre-of-mass such that its eccentricity satisfies $e > 1$.

The first criterion follows naturally from the definition of unbound systems. If a particle's kinetic energy is larger than its binding energy, it has a large enough velocity to escape the system.

The second criterion ensures that particles aren't automatically flagged as ejected if the other three are satisfied. This is important because, during a particle's ejected trajectory, it may yet feel perturbations which nudge the particle's orbital parameters enough to make it bound to the system once more.

The third criterion ensures that the particle moves away from the cluster. It acts as a safety check on whether a particle is bound to the system. The fourth also acts as a safety since it mathematically amounts to the same argument laid out by the first criterion since $E \propto (e^2 - 1) > 0$ and thus $K_E > |P_E|$. Figure 4.2 shows a simulation ending by ejection.
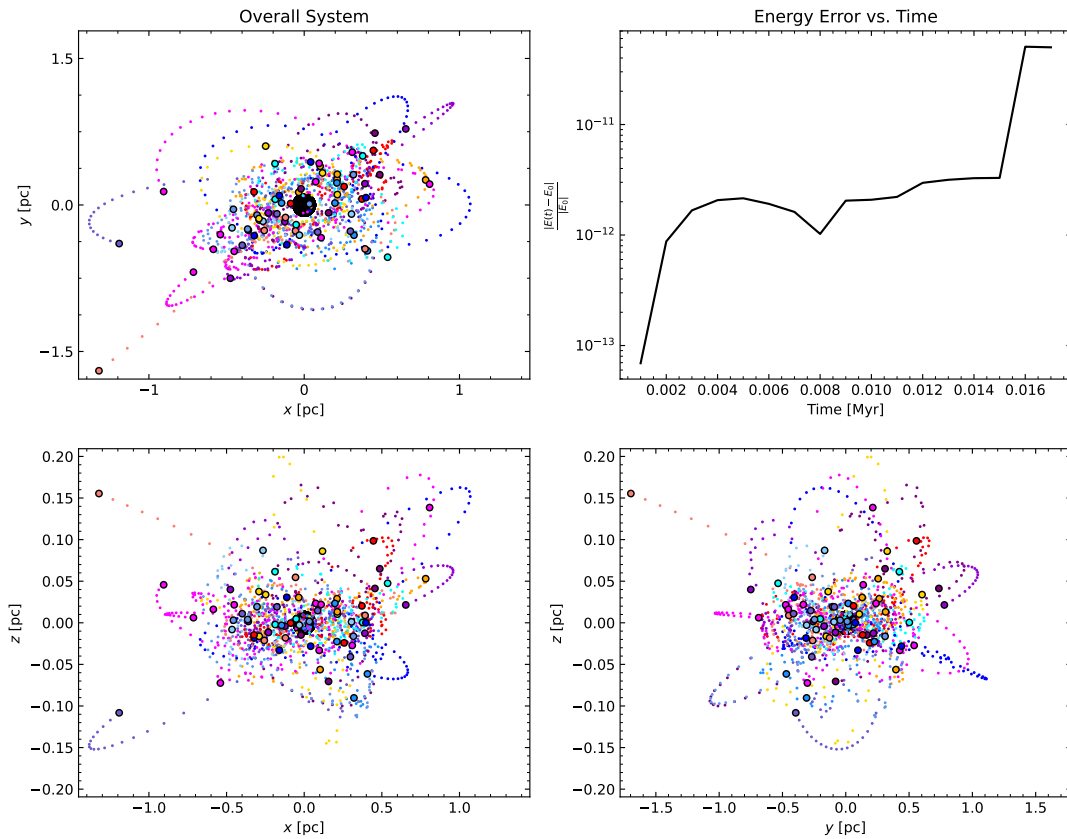

Figure 4.2: Evolution of an $N_{\mathrm{IMBH}} = 70$ simulation using `Hermite`. Coloured are the IMBH particles, and at the origin lies the SMBH. The top-left, bottom-left and bottom-right panels show the particle trajectory in time (small dots) and final position (larger and outlined dots) along the three cartesian planes. The top-right panel shows the energy error of the simulation.

25

Observe that although some particles reach large apostrons, they remain bound to the system and curve back in due time. Contrariwise, the ejected salmon-coloured IMBH particle shows a clear radial trajectory outwards.

We note that the escape velocity of the system at $r = 0.25$ pc is $v_{esc} \gtrsim 263$ km s^{-1}. Thus, a particle takes roughly 6500 years to reach 2.00 parsec, implying a systematic error of the survival time of simulations ending with ejection events by roughly 7000 years.

4.3.2 Stopping Conditions: Merging Events

The final way in which the simulation can end is through a merging event. With `AMUSE`, this is accounted for by turning on collisional detection. A collision is detected by `AMUSE` when the position of two particles lies within a separation distance smaller than the sum of their radii. Here we define the collisional radius to be three times the Schwarzschild radius, that is:

$$r_{coll} \equiv r_{ISCO} = \frac{6GM}{c^2} \tag{4.1}$$

This value reflects the innermost stable circular orbit, r_{ISCO}, defining the regime for which beyond, no stable circular orbits exist and the particle plunges into the event horizon [72]. Our SMBH has a collisional radius of $r_{SMBH, coll} = 51 R_\odot$ whereas our IMBH particles $r_{IMBH, coll} = 0.01 R_\odot$ where $R_\odot$ is the Solar radius.

The stopping condition submerses itself into the algorithm of the gravitational integrator by forcing it to check whether any two particles pass within $r < r_{coll}$ after every internal time step. In doing so, it can resolve the particles' position at intermediate time steps and not simply at the end of every simulation snapshot where collisions may have otherwise occurred and therefore, been skipped over.

Table 4.1 summarises the key parameters. Figure 4.3 shows the codes workflow.

N_{IMBH}	`GRX`: $[10, 40]$, `Hermite`: $[10, 100]$
t	$t_{end} \leq 100$ Myr with $\delta t = 10^3$ years
$\vec{r}_0$	Plummer Distribution
$r_{cluster}$	0.25pc
$\vec{v}_0$	Isothermal Sphere, $\sigma_{disp} = 150$ km s^{-1}
M	IMBH: $10^3 M_\odot$, SMBH: $4 \times 10^6 M_\odot$

Table 4.1: Summary of parameters used for simulations. The columns are in order: The simulated populations, parameters defining the time properties of the simulation, the initial spatial distribution of the particles, the radius of the cluster, the initial velocity distribution of the particles and finally the particles' mass.
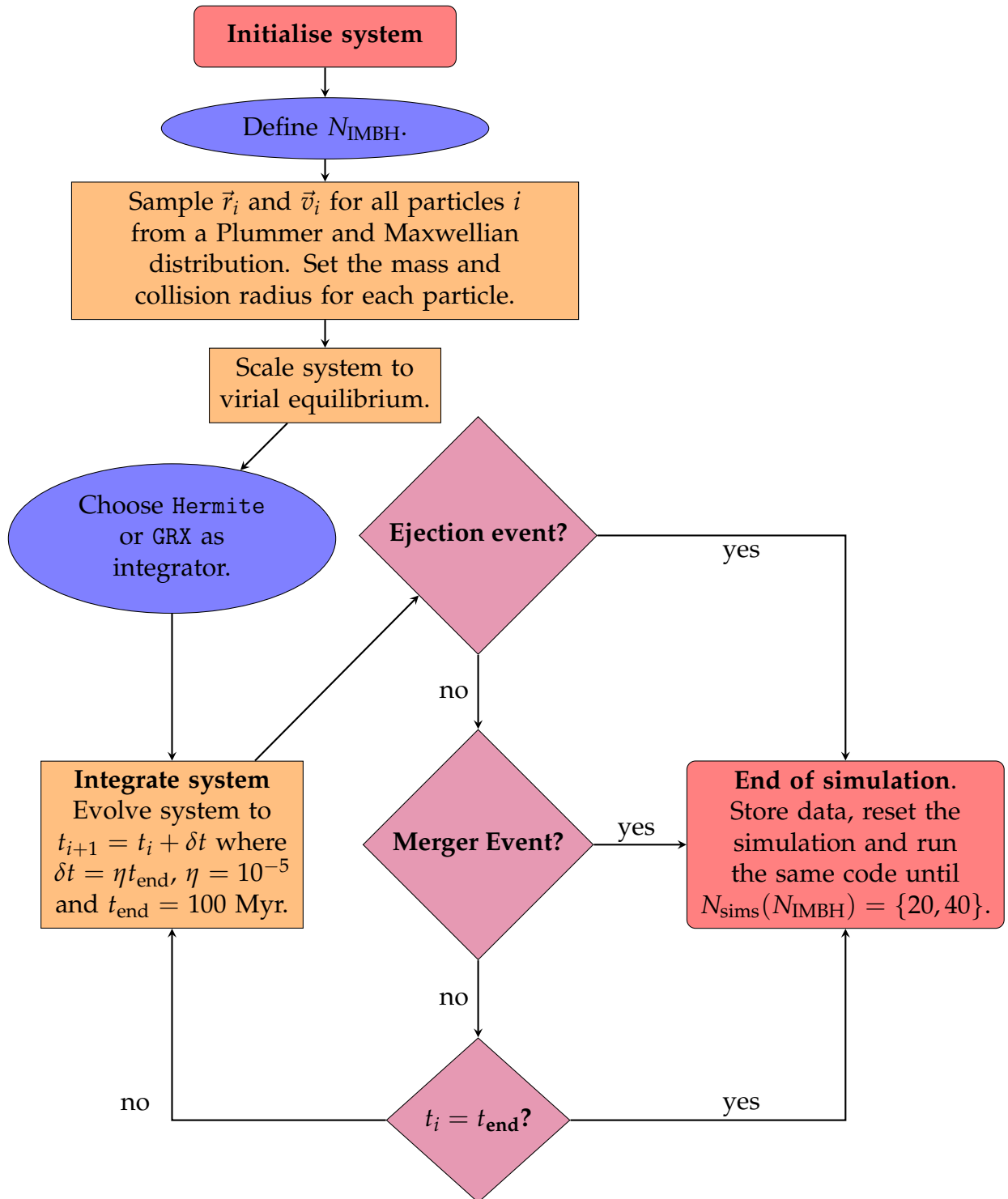
Figure 4.3: Workflow diagram of the code.
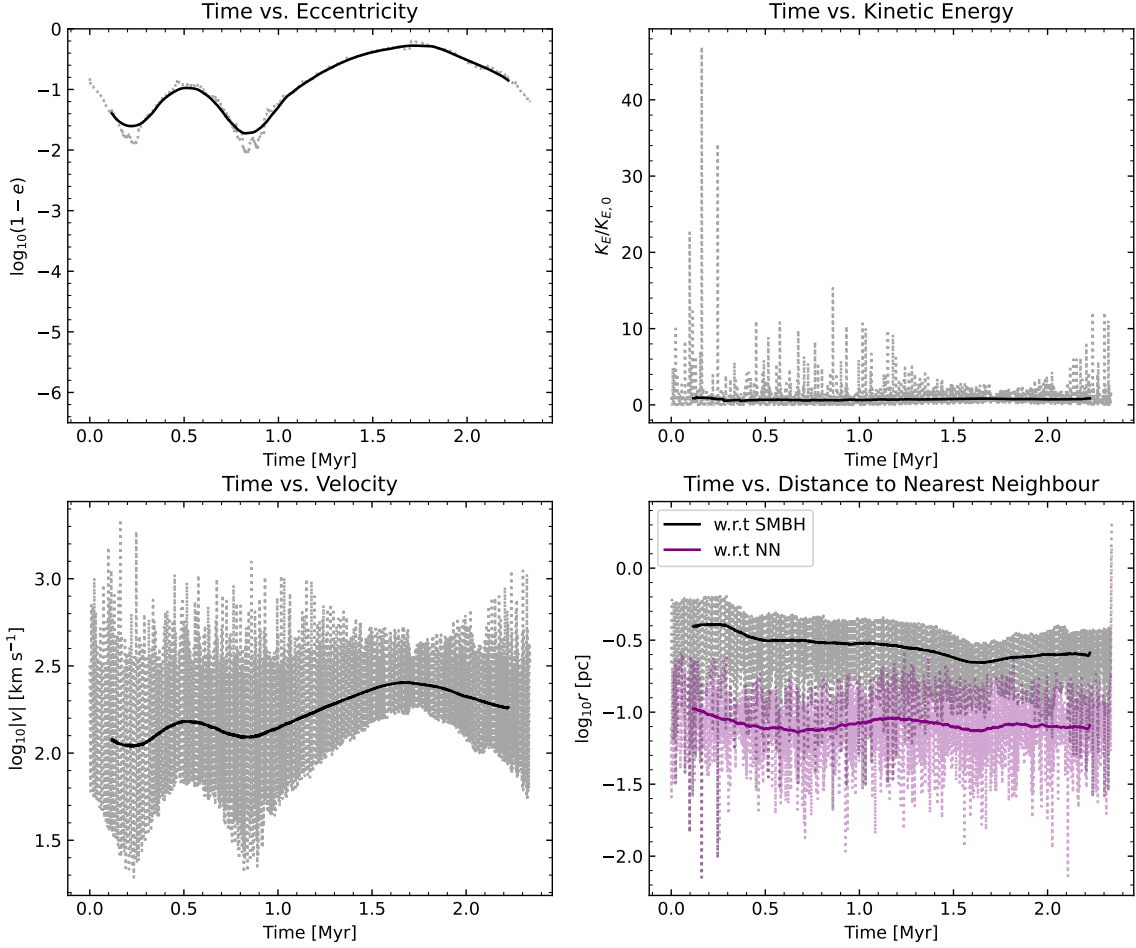
5 Results

5.1 System Evolution

Figure 5.1: The evolution of different parameters corresponding to an IMBH particle flagged as 'ejected' in a $N_{\mathrm{IMBH}} = 30$ `GRX` simulation. The solid lines represent the running average, while the translucent dotted ones the parameters at each snapshot. In the bottom right panel, 'w.r.t' is shorthand for 'with respect to' and 'NN', the IMBHs' nearest neighbour. NN could either be the SMBH or another IMBH. Top left: The eccentricity relative to the SMBH. Top right: The IMBH's kinetic energy relative to its original value. Bottom left: The velocity of the IMBH over time. Bottom right: The distance from the SMBH (black) and nearest neighbour (purple).

Figure 5.1 above shows various properties of an IMBH particle flagged as ejected. The solid lines denote the running average (averaged over 5% of the simulation length), and the dotted ones the value after each snapshot.

The top-left panel shows that the IMBH in this simulation reaches large eccentricities periodically, with the trough attaining values of $\log_{10}(1 - e) = -2.1$. The minima in the $\log_{10}(1 - e)$ factor (maximum eccentricities) coincide with the timing of the velocity minima (bottom left panel), suggesting that the IMBH experiences the greatest changes in its trajectory at apostron. This trend naturally occurs since it is easier for strong encounters to occur at lower velocities since they are events causing a change in the particle's velocity of order $\delta v \approx v$.

The orbit of the IMBH is generally stable and sustained for over a thousand crossing times, which we find by using the definition of a crossing time, $t_{\text{cross}} \equiv \frac{R}{v}$, and taking the liberty to plug in approximate values for the particle inferred by the figure above. Namely: $\langle R \rangle \sim 0.3$ pc, $\langle v \rangle \sim 158$ km s^{-1} with a total simulation time $t \sim 2.5$ Myr. Be that as it may, interactions are frequent due to the large densities in the simulation. As discussed in section 2, the accumulation of weak and strong perturbations can drastically alter the path of a particle. We see this manifest in the plots, namely at $t = 2.4$ Myr when the IMBH finds itself within 0.03pc of the SMBH and another IMBH particle. The interaction with these two particles causes them to eject from the system, the extent of which is highlighted in the bottom right panel, with the distances skyrocketing during the final time step. Though this isn't the closest it has been to another particle, the interactions shift the IMBH sufficiently to eject it.

We shift our analysis to a simulation ending in a merger (figure 5.2). This simulation also consists of $N_{\text{IMBH}} = 30$ and is run using GRX. We note in passing that the results varied greatly between individual simulations. The two examples shown have no special significance.

Here, the IMBH's eccentricity oscillates once more. The most notable difference, however, is that towards the end, the $\log_{10}(1 - e)$ factor decreases much quicker than in the previous example. As emphasised throughout the report, large eccentricities are a tell-tale sign of a merging event. By getting extremely close to the SMBH, the IMBH has a significant amount of its orbital energy exhausted away and finds itself located in an increasingly steep potential well. Though close interaction with the SMBH can cause the particle to eject at times, more often than not in the GRX case, the vast amount of GW energy emitted encourages it to plummet and merge with the SMBH. In this sense, we note the fine margins on which the outcomes depend.

These two plots further motivate our intuition in using equation 2.9 as our overall particle loss rate since they signify that mergers and ejections rely on large eccentricities. As already stressed numerous times, e plays a pivotal role when

reducing GW merging timescales. Additionally, recall that ejection events occur more often for IMBH with large eccentricities due to them reaching the dense cluster core during their orbits and thus are more susceptible to weak and strong interactions relative to their low eccentricity IMBH counterparts, who lie on the outskirts. It is the tweaks in the orbital parameters induced by interactions which determine whether the particle will get trapped within the SMBH potential well and eventually merge with it or whether the IMBH marginally skims the SMBH and ejects from the cluster out onto the other side.
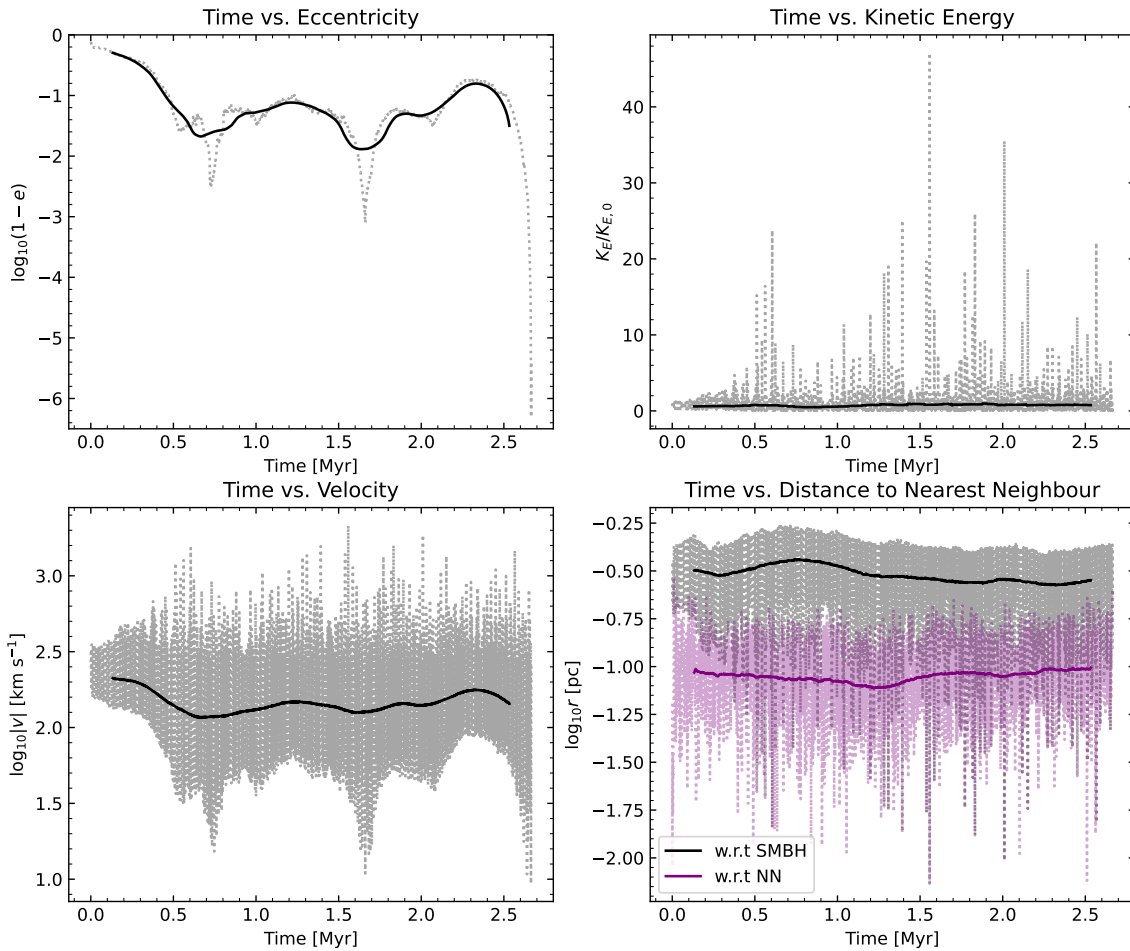

Figure 5.2: Evolution of different orbital parameters of an IMBH particle flagged as 'merged' in a $N_{\mathrm{IMBH}} = 30$ `GRX` simulation.

Lastly, we note that although the IMBH reaches a peak velocity over 2000 km s^{-1}, ejection doesn't occur due to it happening when it is near the SMBH where the

potential is the strongest ($r_{\text{NN}} \approx 2.5 \times 10^{-3}$ pc, $v_{\text{esc}} = 2630$ km s^{-1}).

Figure 5.3 below shows the cumulative distribution (hereafter CDF) of similar properties as the previous plots for all IMBH particles that merge. To avoid bias in our comparison, we ensure that a givens simulations data is extracted only up to the timestep corresponding to the minimum between the individuals' simulation time or the average simulation time for simulations run with the same population in the GRX case. The main result is in the top-left panel and shows that GRX tends to larger eccentricities, even during mergers.
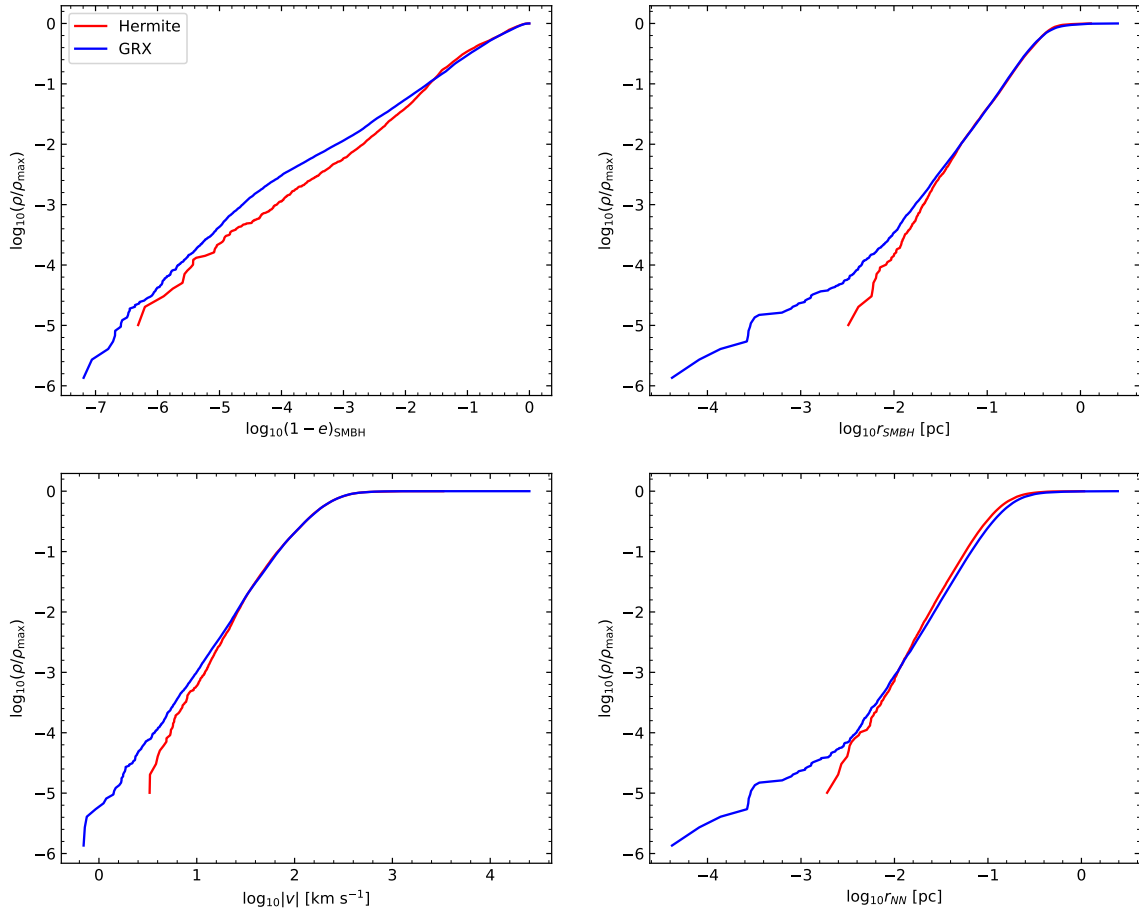
Figure 5.3: The CDF plots of various orbital parameters of 'merged' IMBHs. Top left: The eccentricity attained. Top right: The distances attained between the IMBH and SMBH. Bottom left: The velocity values occupied. Bottom right: Distances to the IMBHs' nearest neighbour.

With clear differences in the eccentricities obtained, the plot tells us explicitly that modelling relativistic systems requires PN terms as it could drastically alter the

final results. In fact, not only is eccentricity substantially larger for all values between $0.97 \lesssim e < 1$, but it spans a wider range, with particles able to reach the extremities more often.

The right-hand panels show the distances between any individual IMBH with the SMBH and its nearest neighbour. The `GRX` curves at $\log_{10} r$ [pc] $\lesssim -3.2$ show identical behaviour, signifying that beyond a critical value of $\log_{10} r$ [pc] ≈ -3, the nearest neighbour is always the SMBH. `Hermite` doesn't have this since the negligence of GW emission means the IMBH has more difficulty reaching close distances to the SMBH, resulting in reduced merger rates (see table 5.1).

Though intermediate values of r_{NN} occur more often with `Hermite`, this is a result of the low samples. Tracking the properties of all particles simulated increases the number of samples and results in the removal of the trend, as seen in figure 5.4.
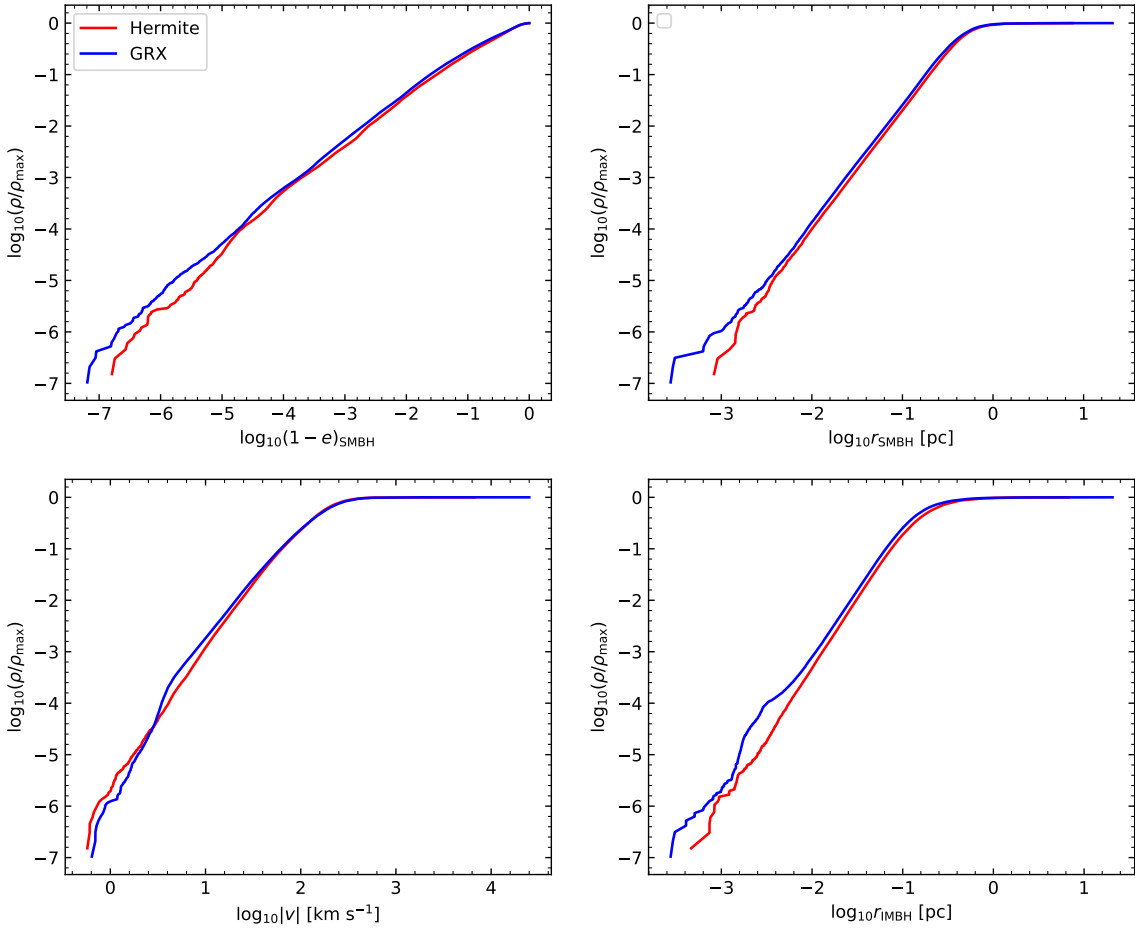

Figure 5.4: The CDF plots of various orbital parameters for all particles present in each simulation.

Figure 5.4 shows the same global characteristics. Specifically; `GRX` exhibits larger eccentricities and closer distances between particles relative to `Hermite`. Interestingly, eccentricities reached for `Hermite` when accounting for all particles attain larger values (smaller $\log_{10}(1-e)$) compared to the purely merging case. Though these large eccentricities should amount to mergers due to them essentially defining radial paths, if the particle skims the collision region of the SMBH, it could be ejected out at extreme speeds. The lack of energy dissipation makes it harder for the particle to succumb to the pull of the SMBH.

Additionally, though hard to see, IMBH velocities for `GRX` runs reach higher values, and a lower proportion of them occupy the low values ($v \leq 40$ km s^{-1}). The higher velocities reached are due to their ability to sink ever closer to the SMBH, as we have seen in the two previous figures, and whose increasingly strong gravitational pull boosts the IMBH. This also explains the lower proportionality of low velocities, since the simulated cluster in `Hermite` tend to have larger radii, and thus, is generally a colder system in that particles often find themselves orbiting on the outskirts.

Applying the Kolmogorov–Smirnov test, each distribution rejected the null hypothesis ($p \leq 0.05$), entailing that the distributions are statistically significant from one another.

Figure 5.5 shows the fraction of simulations ending with mergers. The substantial differences highlight once more the necessity of PN formalism when studying mildly relativistic environments. `GRX` never reaches a SMBH-IMBH merging outcome of less than 90%, while for `Hermite` the peak is an SMBH-IMBH merging rate of 68%, occurring for $N_{\text{IMBH}} = 20$. The linear decrease in merging fractions relative to the population for `Hermite` is due to the larger number of binary systems, which, as discussed in section 2.2.2, help prompt ejection events. The low merger fraction for $N_{\text{IMBH}} = 10$ `Hermite` is due to thirteen of its twenty simulations reaching $t = 100$ Myr (the third stopping condition).

Table 5.1 summarises the simulation outcomes. N_{sims} denotes the total number of runs, SMBH and IMBH Mergers the number of SMBH-IMBH and IMBH-IMBH events respectively, ejections the number of ejection events and N_{100Myr} the number of times a simulation reached 100 Myr.

	N_{sims}	SMBH Mergers	IMBH Mergers	Ejections	N_{100Myr}
`Hermite`	200	86	0	100	14
`GRX`	280	257	0	19	4

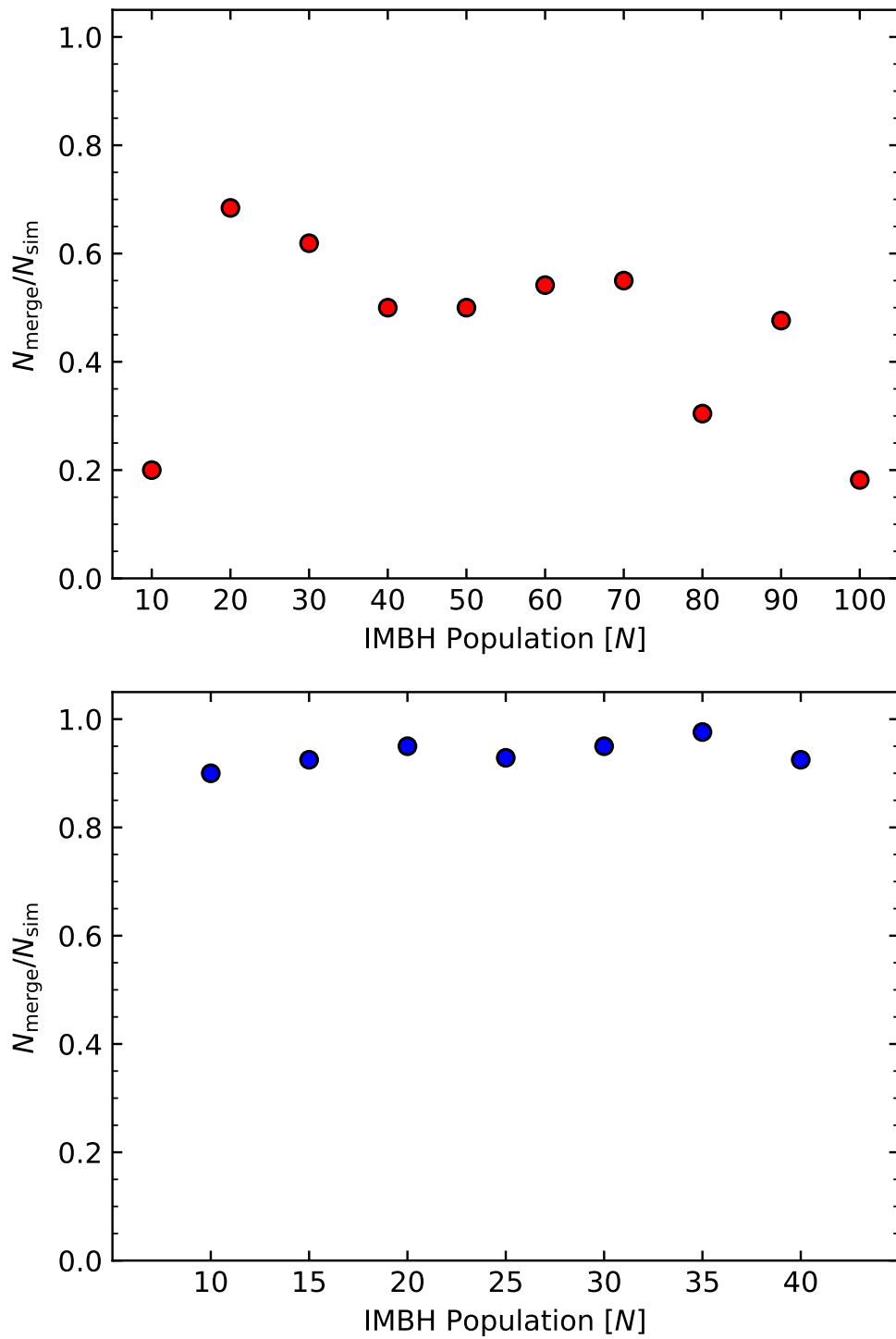**Table 5.1:** Summary of simulation outcomes.

Figure 5.5: Fraction of simulations ending with a merger. The top panel shows `Hermite` results. The bottom panel shows results for `GRX`.
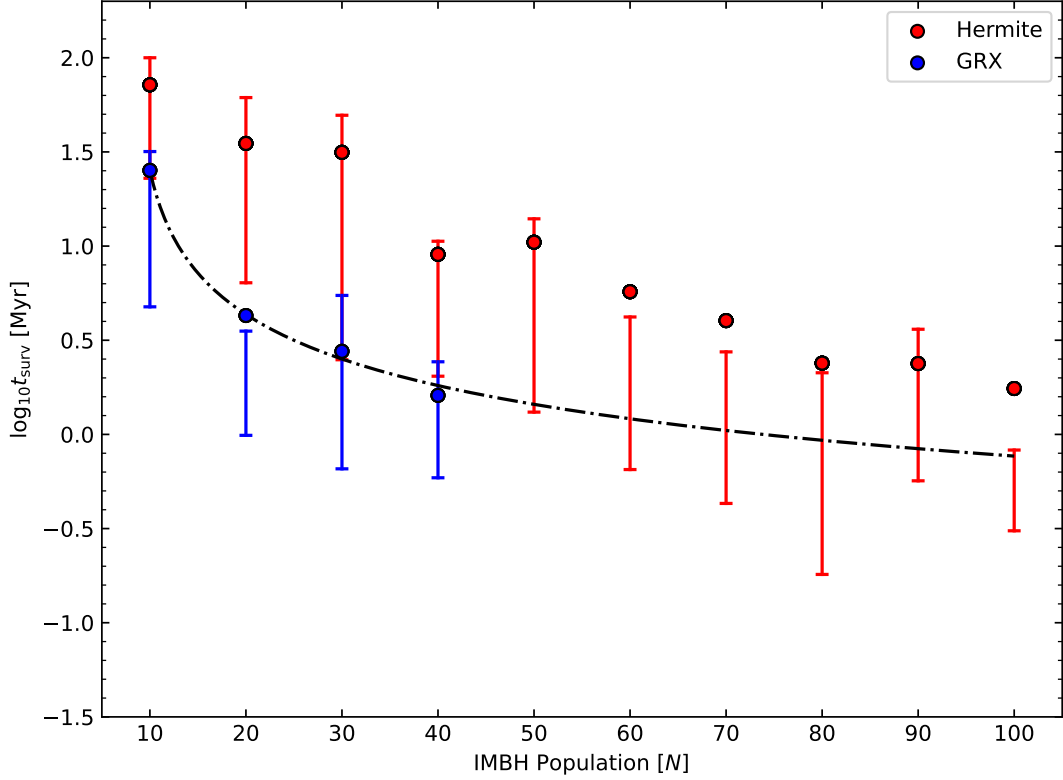
5.2   Stability Time

Figure 5.6: Simulation times depending on the IMBH population. Filled circles signify the mean. The upper bar shows where 75% of the data lies below (the upper percentile) and the lower one where 25% of the data lies below (lower percentile).

Figure 5.6 shows the average time before particle loss occurs (t_{surv}) depending on the IMBH population. The figure represents the main result of the thesis as it answers our primary aim, what constitutes a steady-state population of IMBH in the MW. The filled circles denote the average simulation time for each IMBH population, while the upper and lower bars denote where 75% and 25% of the data lie below and above (the interquartile range).

As alluded to throughout the thesis, accounting for PN effects decreases the survival time of a given population relative to a Newtonian algorithm. Here we finally see the effect manifest itself explicitly. For all populations of $N_{\mathrm{IMBH}} > 10$, this difference is over an order of magnitude. We note that this trend may also hold for the $N_{\mathrm{IMBH}} = 10$ case since 65% ($N_{\mathrm{sims}} = 13$) of $N_{\mathrm{IMBH}} = 10$ `Hermite` runs reached $t = 100$ Myr, while for `GRX` only 8% ($N_{\mathrm{sims}} = 3$) reached the maximum

simulation time. This natural cap on the simulation time of $N_{\mathrm{IMBH}} = 10$ runs makes it difficult to interpret deviations between either simulation. Additionally, 10% of the `Hermite` $N_{\mathrm{IMBH}} = 20$ runs reached $t = 100$ Myr, while for `GRX` this occured 0% of the time, with $N_{\mathrm{IMBH}} = 15$ reaching it once (2.5%).

Following our discussion in 4.1 and assuming an MW IMBH infall rate of one every 7 Myr (equivalently $\log_{10} t$ [Myr] = 0.845), results from `GRX` predict a steady-state IMBH population at the galactic core between 10~20. Contrariwise, `Hermite` has this value increase to $N_{\mathrm{IMBH}} = 50$~60. Given that general relativity better describes nature, we show the results for `GRX` in the figure below.
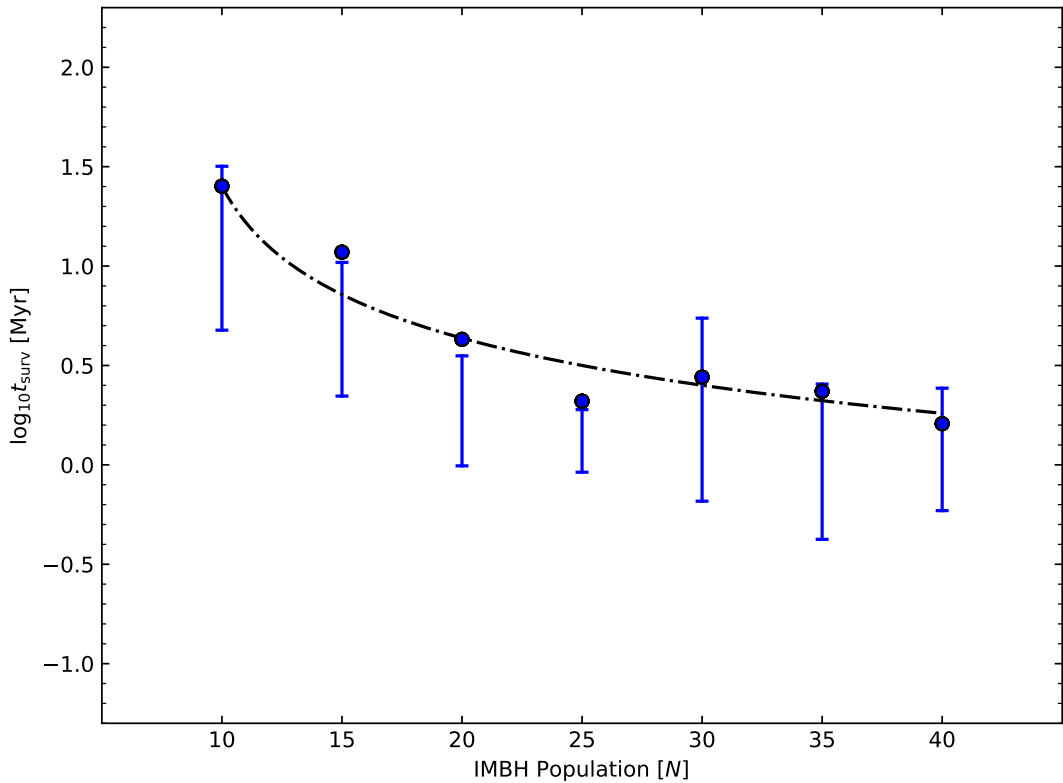
Figure 5.7: Simulation times depending on the IMBH population for `GRX`.

Refining our previous estimate with figure 5.7, we conclude that the inner 0.4 parsec of the MW, a value determined from the average half-mass radius of the cluster, may harbour a steady state of $N = 15$~20 IMBHs in a MW-like galaxy.

Given the various assumptions made, this value may vary depending on the model (recall that papers often suggest an infall rate of one IMBH per Gyr).

Furthermore, the assumed infall rate isn't a fixed value and, instead, fluctuates throughout the galaxy's life. Here, we based our results on the average value found in Portegies Zwart et al. (2006) [31]. Lastly, we stress that only one specific configuration was investigated in this report, changing initial conditions such as the IMBH mass, the initialised IMBH distance from the central SMBH, properties of the central SMBH black hole or the positional distribution of the system amongst others could influence results.

Given the complexity of the dynamics, it is hard to predict how these changes may alter results. However, given the theory developed in section 2, one may expect that a lower IMBH mass may increase the stability time as GW emission becomes less pronounced as reflected by a decrease in the GW timescale (see equation 2.24). Additionally, decreasing the mass also lowers the gravitational cross section making perturbations less significant and increasing the relaxation time. Increasing the relaxation time means an increase in our derived particle escape rate (see equation 2.2 and equation 2.9). Furthermore, sampling the particle mass from a distribution function result in an increase in ejection events. We reason with this since the equipartition theorem states velocities should increase for lower mass particles after encounters. During encounters with a large mass ratio, the lower-mass particle will experience a large change in its velocity.

In terms of increasing the distance of the IMBH relative to the central SMBH, we predict that this results in longer stability times and, thus, a larger IMBH population in the galactic core. All of these influences are worth taking a deeper look at, though some require further manipulation of the system than others (i.e changing the central SMBH mass may influence our inferred infall rate).

The line-of-best fit (dashed) in figure 5.6 and figure 5.7 should be taken with a grain of salt given the sensitivity to individual simulations and the low number of runs. Even so, it mimics the form of equation 2.9. The mathematical expression for the curve is:

$$t_{\text{loss}} = 15.87 \, \text{Myr} (\sqrt{N} \ln 0.121 N)^{-0.942} \tag{5.1}$$

Here we note several features. The first is that the γ factor in $\ln \gamma N$ is similar to results for equal N-body systems observed by Spitzer (1987) [38] and Giersz and Heggie (1994) [39] who found $\gamma = 0.11$. The extracted power law is slightly smaller than predicted but lies within a reasonable range. Physically, the difference may come from the derivation following a Newtonian argument, whereas final results rely on PN effects, entailing that the derivation may have neglected various subtleties. Finally, the pre-factor 15.87 Myr is of the same order as the 51.05 Myr predicted in equation 2.9. Recall that the earlier expression is

37

derived using the evaporation rates and that the inclusion of mergers decreases the factor since it adds in a new particle loss mechanism, as seen here. In passing, we note that the loss cone forms an interesting aspect of binary dynamics and the final parsec problem. Although the results are not added here due to the information it provides being repetitive, Appendix D provides a brief analysis for the curious reader.

Plugging $t_{\text{loss}} = 7$ Myr into the expression and working backwards, we find a predicted steady-state population of $N_{\text{IMBH}} = 15.24$ in the heart of Milky Way galaxies.

A keen eye may have observed a strange behaviour between some of the data points in both figures. At times the mean lies above the upper percentile range. All this is saying is that the mean survival time gets skewed by outliers who vastly exceed the time range where the vast majority of the data lies. Figure 5.8 illustrates this fact by combining similar distributions found for the $N_{\text{IMBH}} = 60$ and $N_{\text{IMBH}} = 70$ populations in the Hermite runs.
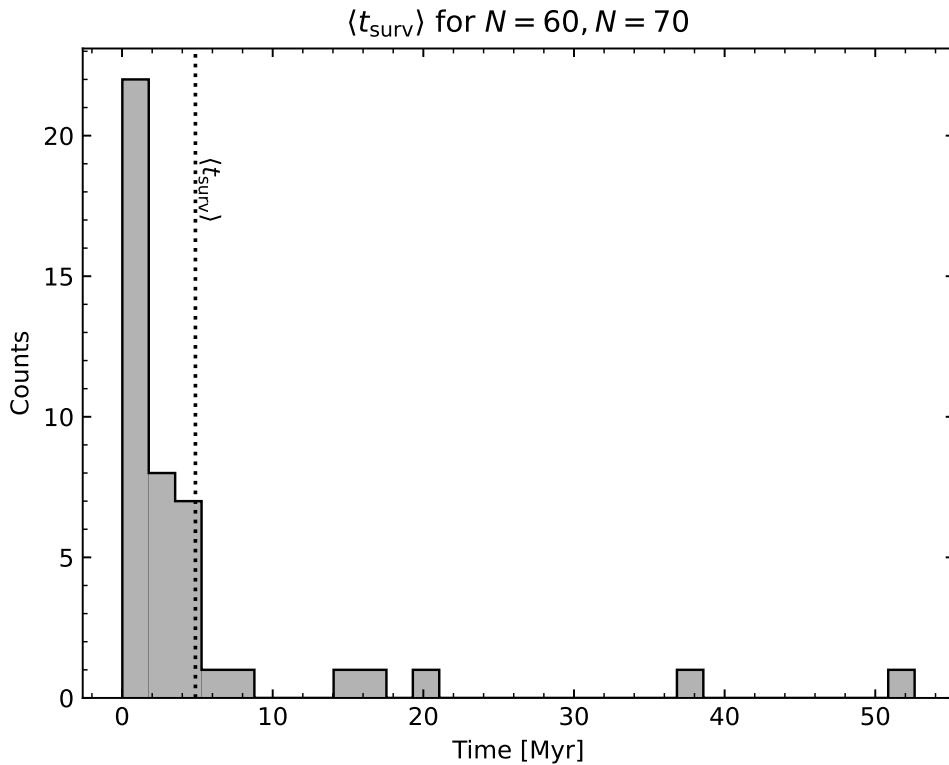

Figure 5.8: Combined histogram of the survival rate for $N_{\text{IMBH}} = 60$ and $N_{\text{IMBH}} = 70$ during Hermite runs. The dashed vertical line corresponds to their combined average survival time, t_{surv}.

The dashed vertical line denotes their combined average time while the counts denote the frequency the simulation ended at a given time range (bins of ~ 2 Myr). We note that although an overwhelming majority lies below the mean, the rare occurrence of an $t_{\text{surv}} \sim 37$ Myr and $t_{\text{surv}} \sim 51$ Myr simulation shifts the average to go beyond the upper percentile range.

Table 5.2 summarises the extracted mean simulation time in Myr per population.

N_{IMBH}	10	20	30	40	50	60	70	80	90	100
Hermite ($\langle t_{\text{surv}} \rangle$)	71.8	35.1	31.5	9.04	10.5	5.72	4.02	2.39	2.38	1.75

N_{IMBH}	10	15	20	25	30	35	40
GRX ($\langle t_{\text{surv}} \rangle$)	25.2	11.8	4.28	2.09	2.76	2.35	1.61

Table 5.2: Summary of simulation outcomes. Survival times are in Myr.

5.2.1 Forecasting Mergers

The merger of an IMBH into an SMBH creates energetic events which are detectable throughout the Universe with next-generation interferometers such as LISA. Here, we take a rudimentary approach and predict the expected GW event rate a 7 Myr steady-state population implies.

Using the merger fraction found in figure 5.5, we predict an IMBH-SMBH merger event rate of one per $7.\overline{77}$ Myr. From here, we define our total event rate:

$$\Gamma \equiv \frac{d}{dt} \iint \frac{dN(z)}{dM_{\text{gal},*}} \Phi(z, M_{\text{gal},*}) \, dM_{\text{gal},*} dz \qquad (5.2)$$

Where $\frac{dN(z)}{dM_{\text{gal},*}}$ is the number of events per galactic stellar mass and $\Phi(z, M_{\text{gal},*})$ the Press-Schechter function, which predicts the number of galaxies of a given mass up to some redshift. Assuming that $\frac{dN(z)}{dM_{\text{gal},*}}$ is constant for all galaxies and basing our results on the MW, we adopt a galactic stellar mass of $M_{\text{MW},*} = 6 \times 10^{10} M_{\odot}$ [115] such that the event rate becomes:

$$\frac{d}{dt} \frac{dN(z)}{dM_{\text{gal},*}} = 2.143 \times 10^{-12} \, \text{Myr}^{-1} M_{\odot}^{-1} \qquad (5.3)$$

Using Press-Schechter parameters found with the EAGLE simulation (table A.1 of Furlong et al. (2015) [116]) and cosmological parameters found by Planck (2018) [117] to integrate over redshift, we extract the number of events up redshift $z = 3$.

Our results integrate over galaxies lying within the mass range $M_{\mathrm{gal},*} \in [10^8, 10^{14}] M_\odot$, the lower limit corresponding to galaxies harbouring an SMBH while the upper limit follows from the galactic mass range probed in Furlong et al. (2015) [116]. Figure 5.9 shows the results.
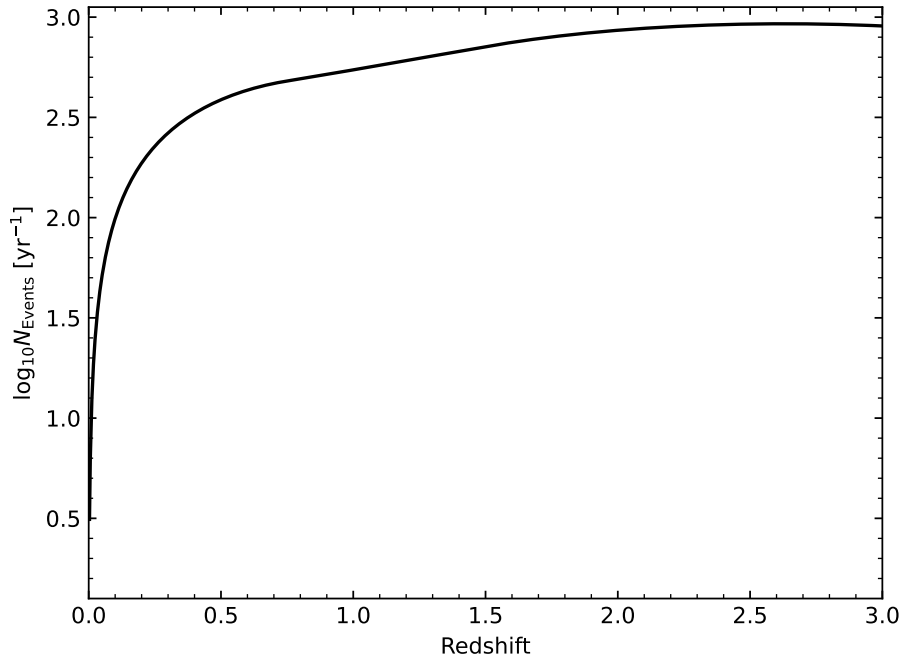

Figure 5.9: The cumulative forecasted SMBH-IMBH events.

The cumulative event rate up to redshift $z = 3$ is $\Gamma = 926$ events per year ($\Gamma = 2.54$ day^{-1}). This value is nearly three orders of magnitude larger than that found in ([5]; [118]; [119]). The discrepancy arises from several factors, most notably their inferred infall rate of $\sim$Gyr scales, which decreases predictions by two orders of magnitude. Furthermore, their investigation looks at the merger rates in which an NSC and SMBH reside in the galactic centre. This amounts to $\epsilon = 0.3$ of all galaxies lying in their more restricted mass range, $M \in [10^{8.5}, 10^{10.75}] M_\odot$ ([2]; [5]; [120]). Following the same procedure with their assumptions would reduce our predicted event rate to $\Gamma \sim 1.92$ yr^{-1}, lying within their range. Indeed, given the huge range of possible values, the LISA interferometer will be key to constraining various properties of the model investigated.

The value found is dependent on various assumptions. In addition to generalising MW results for all galaxies, here we neglect the formation rate of GCs and the delay

time for which they emerge within galaxies. Both diminish the inferred event rate, meaning we should interpret our prediction as the upper limit.

5.2.2 Ejection of Intermediate-Mass Black Holes

As discussed in section 2.2.2, IMBHs may eject from the cluster at extreme speeds. Although table 5.1 shows GRX is not immune to such events, we detract from our otherwise GRX-centric discussion and look at Hermite runs due to the more frequent experience of ejection events.

Figure 5.10 shows the mean ejected velocity as a function of population (top) and the combined ejection velocity distribution (bottom). The smallest average value corresponds to N_{IMBH} with $\langle v_{\text{ejec}} \rangle = 267$ km s^{-1} which is near the lower bound (recall that for $r = 0.25$pc, $v_{\text{esc}} = 263$ km s^{-1} in our cluster).

Looking at the colour code of the top panel, we note that the ejection time roughly follows the trend seen in figure 5.6, where an increasing population takes a shorter amount of time to eject a particle. The longest average ejection time was for $N_{\text{IMBH}} = 30$ with $\langle t_{\text{ejec}} \rangle = 39.7$ Myr, whereas the shortest occured for $N_{\text{IMBH}} = 80$ with $\langle t_{\text{ejec}} \rangle = 1.37$ Myr. Table E.1 in Appendix E summarises the ejection statistics for Hermite (table E.2 for GRX). The appendix also provides the equivalent plots for GRX.

Though the number of samples is too low to formulate a conclusive discussion of some observed characteristics, we dissect the global properties. Generally, ejection events occur more often and sooner for larger populations. Linking back to section 2.2.2, we understand this because ejection events often need binary systems to release their binding energy before they can convert the free energy into their kinetic energy, boosting it in the process. The dependency on population size gets accentuated by the fact that binary formation often needs a third particle to absorb any excess kinetic energy before forming and that, naturally, with more particles present, it is easier for these systems to emerge in denser systems. All these effects result in the perceived shorter ejection time and more frequent ejection events.
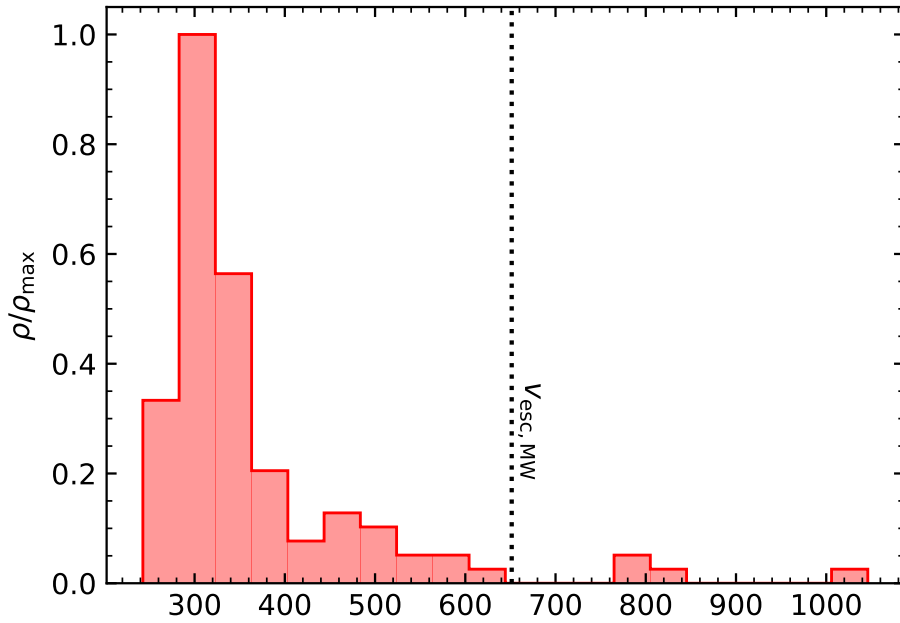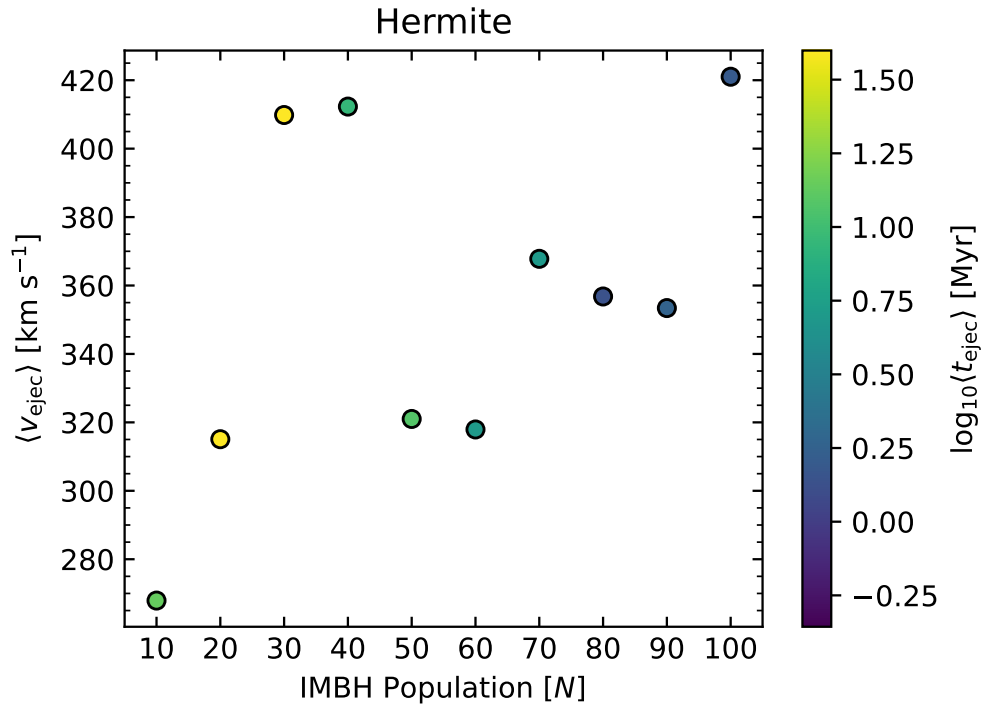
Figure 5.10: Top: Average ejection velocities as a function of IMBH population. Bottom: Histogram showing ejection velocities of simulations ending with ejections. Both panels are for `Hermite`.

The histogram shows that on four separate occasions, the ejected IMBH exceeds the MW escape velocity at $r = 0.2$ pc ($v_{esc, MW} \sim 660$ km s^{-1} when using Bovy (2015) [121] and including the SgrA* mass). Though this phenomenon is much less common in GRX, it could be insightful in future investigations to scatter lower mass particles to replicate a stellar population around the central SMBH and see the rate at which HVS form or where the ejected particles settle. Perhaps they can form an observable outer shell consisting of lower-mass compact objects and stars. In fact, observational data show that the NSC exhibits a segregation of stellar population, with the older stars lying on the outskirts and recently formed stars lying nearer to the centre [122].

This detachment between the stellar population is thought to relate to older stars having had time to scatter with massive particles, whereby they gain kinetic energy and climb out the potential well to settle onto orbits further out. Instead, younger stars have not yet experienced scattering events which would enable them to settle into distant orbits. Furthermore, the result of unbound IMBH may indicate the possibility of migrating IMBH between galactic systems, though to what extent deserves its own research and is left for future work.

Lastly, we note that our simulation only models the SMBH potential. When accounting for the NSC potential, the SMBH sphere of influence diminishes significantly. For the case of Bovy (2015) [121], the SMBH dominates the dynamics at $r \lesssim 0.1$pc, for which our initialised cluster lies beyond. Including the MW NSC will steepen the potential well of the simulation, and particles will have a harder time ejecting from the system. Although GRX rarely experiences ejection events, a trend also seen in Rodriguez et al. (2018) [70], in reality, the value here is exaggerated. We also note that the exclusion of the NSC potential influences the merging timescales since a steeper potential will allow particles to sink nearer to the SMBH. Nevertheless, the results here provide a good starting point for understanding the effects such a hypothetical environment may bring forward.

5.3 Binary and Hierarchical Systems

As discussed in section 2.2, clusters may include binary and hierarchical systems. In this section, hard binaries are those satisfying equation 2.15, while soft binaries satisfy a more relaxed condition:

$$a < \frac{GM}{4(0.1\sigma)^2} \tag{5.4}$$

Hierarchical systems are those whose outer binary has $e < 1$, semi-major axis $a < 0.1$ pc, and satisfies the Mardling-Aarseth condition stated in equation 2.22. Note

that figure 5.4 tells us that the nearest IMBH-IMBH neighbours are within $r_{\text{IMBH}} <$ 0.1 pc 10% of the time.

Table F.1 summarises the binary systems observed in our simulations while table F.2 that of hierarchical systems. Results show that 11.6% and 7.92% of binaries formed in `Hermite` and `GRX` are hard, a value similar to those found in previous literature (10% in the Newtonian case [123]). The small number of persistent binaries and hierarchical systems observed means that secular effects play a small role in the overall evolution of the cluster.

Figure 5.11 shows the average fraction of time at least one binary or hierarchical system exists for simulations run with varying populations. In both cases, the binary existence fraction ($t_{\text{sys}}/t_{\text{sim}}$) and the average number of binary systems, N_{sys}, formed show nearly identical results. The same cannot be said about hierarchical systems (stable triples). This is no doubt due to the large times needed before triples can emerge (see table F.2), which `GRX` simulations rarely attain. Additionally, due to the IMBH being nearer to the SMBH in the `GRX` case, the particles experience larger velocities making IMBH-IMBH encounters predominantly hyperbolic, making it harder for systems to satisfy the conditions used to define hierarchical systems. With both algorithms, all binaries were detected as SMBH-IMBH binaries.

The line-of-best fit plotted for `Hermite` (H) and `GRX` (G) are:

$$\log_{10}(t_{\text{sys}}/t_{\text{sim}})_{\text{H}} = -0.027N - 0.643 \qquad (5.5)$$

$$\log_{10}(t_{\text{sys}}/t_{\text{sim}})_{\text{G}} = -0.028N - 0.766 \qquad (5.6)$$

The plot shows two global characteristics. Firstly, an increasing IMBH population implies more binaries. Knowledge built throughout section 2.2.2 helps us understand this since we learned that a denser system allows for more triple encounter events. Such encounters are essential since the third particle will absorb any excess energy of the prospective binary, helping them to bind to one another. This necessity of a third particle to carry away energy during binary formation gets emphasised by the large IMBH masses adopted here. Large masses make the relative accelerations of encountering particles at close approaches larger, making it harder for prospective binaries to settle into a stable orbit. It would be interesting to investigate how changing the mass properties of the IMBH influences system formation. Lower masses will allow more binaries (and hierarchical systems) to form. A mass distribution could further increase this tendency. The presence of these systems would change several properties of the cluster and, as already alluded to, are worth taking a deeper look at (i.e number of ejection events, number of GW events, final particle distribution ...).
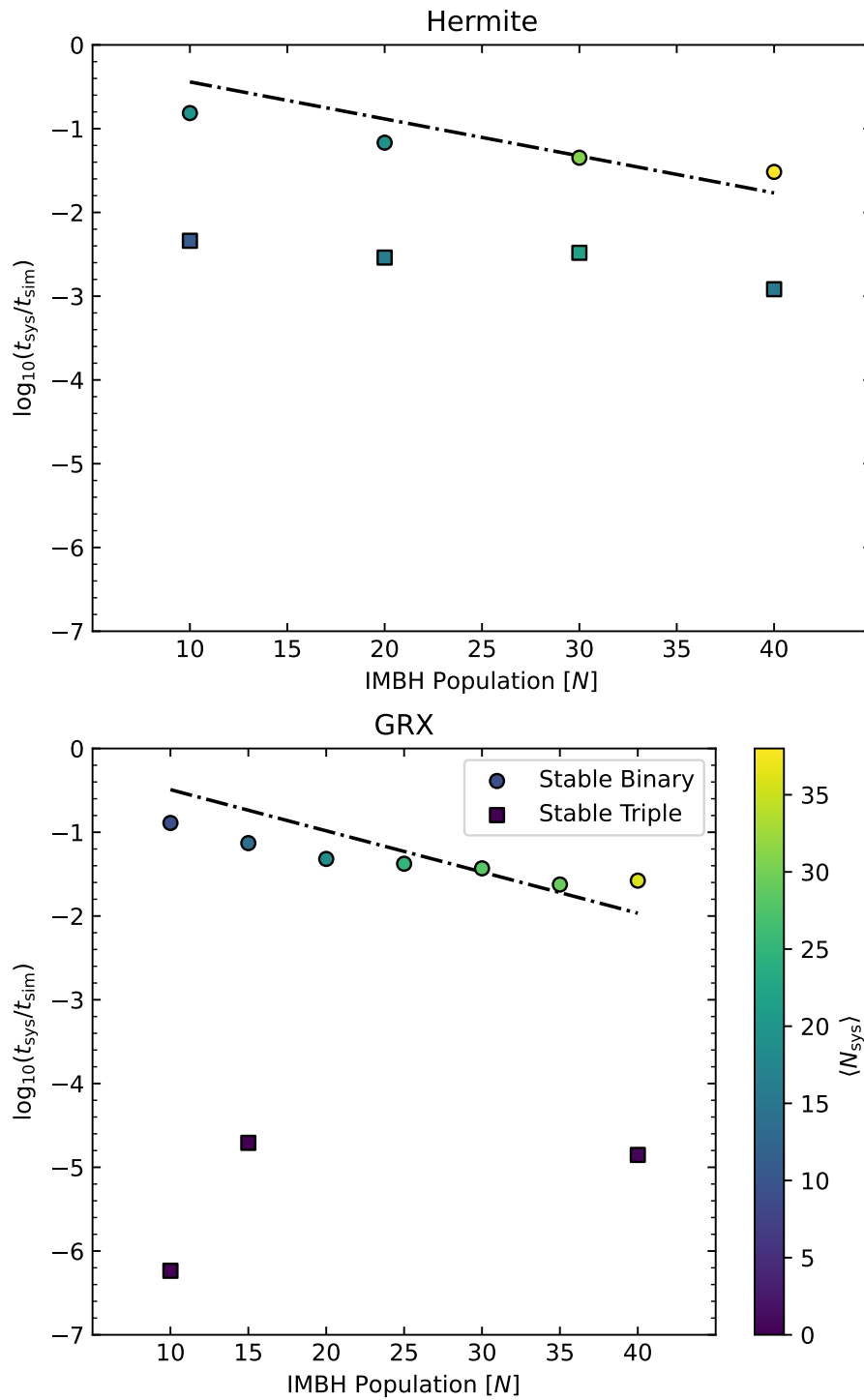
44

Figure 5.11: The average percentage of time binary and triple systems are present.

Secondly, the larger the population, the lower the fractional presence of a binary or hierarchical system. Although this may seem to contradict the fact that more systems emerge in more populated clusters, results show that the average formation time of the first system, at best, weakly correlates with the initial population (see table F.1) while the system lifetime has a strong inverse relationship with the initial population (recall figure 5.6). The latter relation has more influence, causing the value to diminish. This also explains why GRX exhibits a lower number of systems.

More specifically, although the time of first formation is ever so slightly reduced for GRX $N_{IMBH} \geq 20$ runs, their system lifetime is consistently an order of magnitude lower. IMBHs need time to settle and exchange energy before forming binaries, a resource not as readily available in GRX runs. This results in the suppression of their formation. In theory, PN terms should increase the formation of binary's and, to an extent, hierarchicals since the presence of GW emission reduce orbital energies, providing an outlet for stable systems to form. Indeed, in a more controlled environment that doesn't stop the system once particle loss occurs, including PN terms increases the formation of binaries [70].

We note in passing that presence of hierarchical systems in the simulations is roughly 1.4 orders of magnitude lower than the binary systems for all populations in the Hermite case. It could be insightful to see whether this tendency emerges in GRX simulations which run for longer times. This would help uncover some of the complex dynamical behaviour present in these systems and further enhance our understanding of the role PN terms have on system formation.

With their sustained interactions, binary and hierarchical systems generate a consistent source of GW events. Figure 5.12 shows where in frequency-strain space these events lie when assuming an event luminosity distance of $D_L = 1$ Mpc. Observe that, although present, hierarchical systems barely contribute to the total GW emission suggesting that they get quickly disrupted.

The next section will include transient events. For now, we note that binaries show larger strains and frequencies than their hierarchical counterparts (see figure F.1 for a clearer example). Both of these characteristics are due to binary systems having a smaller semi-major axis, which influences the strain and frequency as $h \propto \sqrt{f^{-4/3}\dot{f}} \propto f^{5/3} \propto a^{-5/2}$ (using equations 2.26, 2.27 and 2.31).
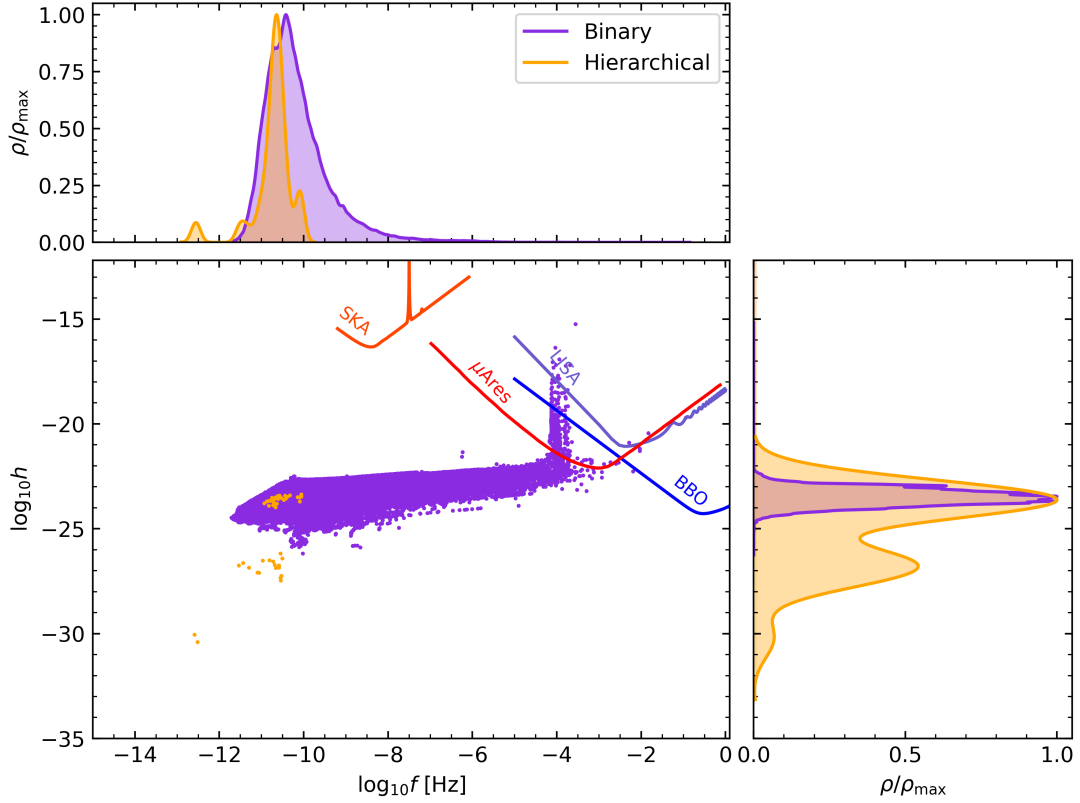
Figure 5.12: Diagram showing where GWs emitted by binaries lie in (f, h)-space in our `GRX` simulations composed of $N_{IMBH} \leq 40$. Overlayed on the plot are four gravitational interferometers: Square Kilometre Array [124], μAres [78], LISA [71] and the Big Bang Observer [125].

Over time, as binaries harden, their strains and frequencies increase, causing a rightward shift of events. With the ever-tighter binaries undergoing circularisation ($e \to 0$), the frequency will only slightly change, scaling with $a^{-3/2}$ multiplied by some eccentricity-dependent factor quickly approaching zero. Meanwhile, the opposite holds for the strain, with the power emitted being strongest at circularisation - explaining the near-vertical ascent once systems approach the detectable range.

Figure 5.13 perfectly encapsulates this scenario and shows only events induced by hard binaries. Once more, the prominent vertical feature is present. Additionally, figure 5.13 shows that a larger semi-major axis causes a weakening of the strain due to the reduced number of events detected with strains $h < 10^{-24}$, signified by the narrower kernel density estimate shown in the right-hand panel.

Neglecting the effect of a shortened simulation time, the same f vs. h plot for

`Hermite` doesn't exhibit the vertical ascent otherwise seen above (see figure F.1). This difference exemplifies once more the difficulty Newtonian algorithms have in reducing the semi-major axis of binaries, especially in systems with such large masses where PN terms are made more prominent. A fact also reflected with the smaller fraction of binaries formed having coalescence time $t_{GW} < t_H$ (table F.1).
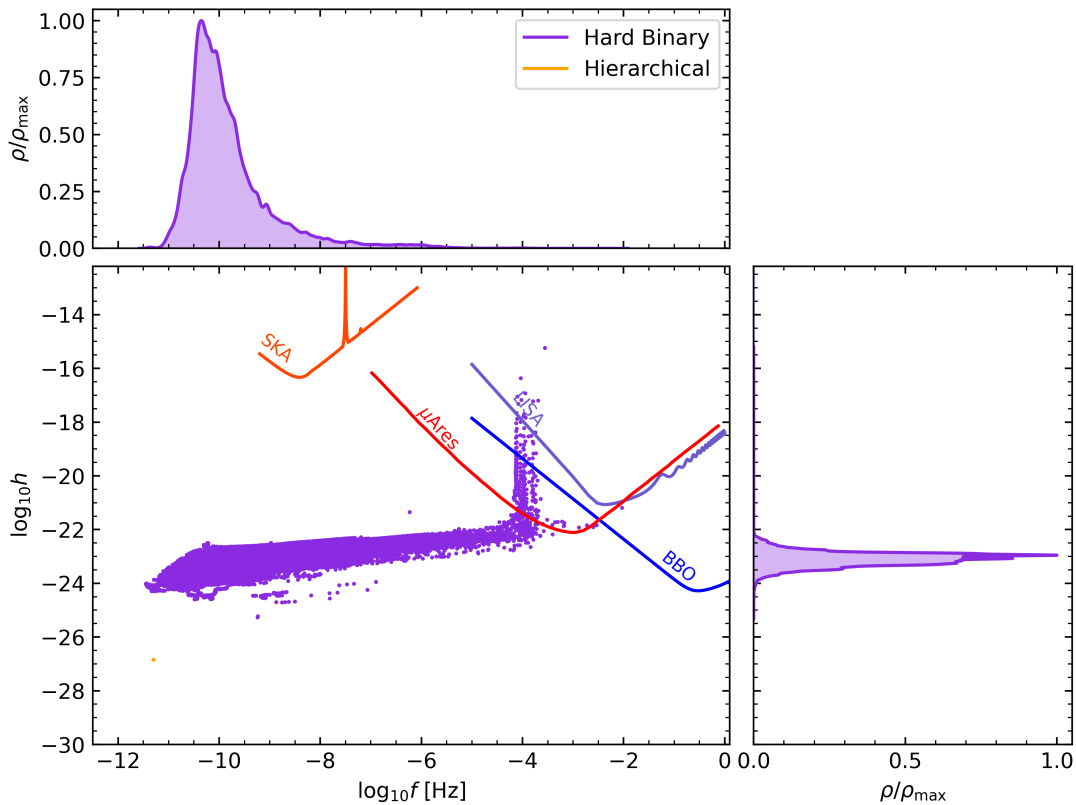
Figure 5.13: Diagram showing where GWs emitted by hard binary systems lie in (f, h)-space for `GRX` simulations with $N_{IMBH} \leq 40$ The single hierarchical data point signifies the fact that in only one time step did a tertiary IMBH interact with a hardened binary.

In both of the previous figures, streak-like features appear. These streaks are artificial since we can only detect GW events occurring at the simulation snapshots. The radial drift corresponds to the hardening of a binary system. Figure 5.14 shows an example of this by tracking a particular binary system found in a `GRX` run. Observe that as time moves forward, the events shift to larger frequencies and strains, signifying the hardening of the system. As we will see later, figure 5.17 exhibits the same streak, although with a different perspective, allowing a clearer understanding of the binary evolution.

48

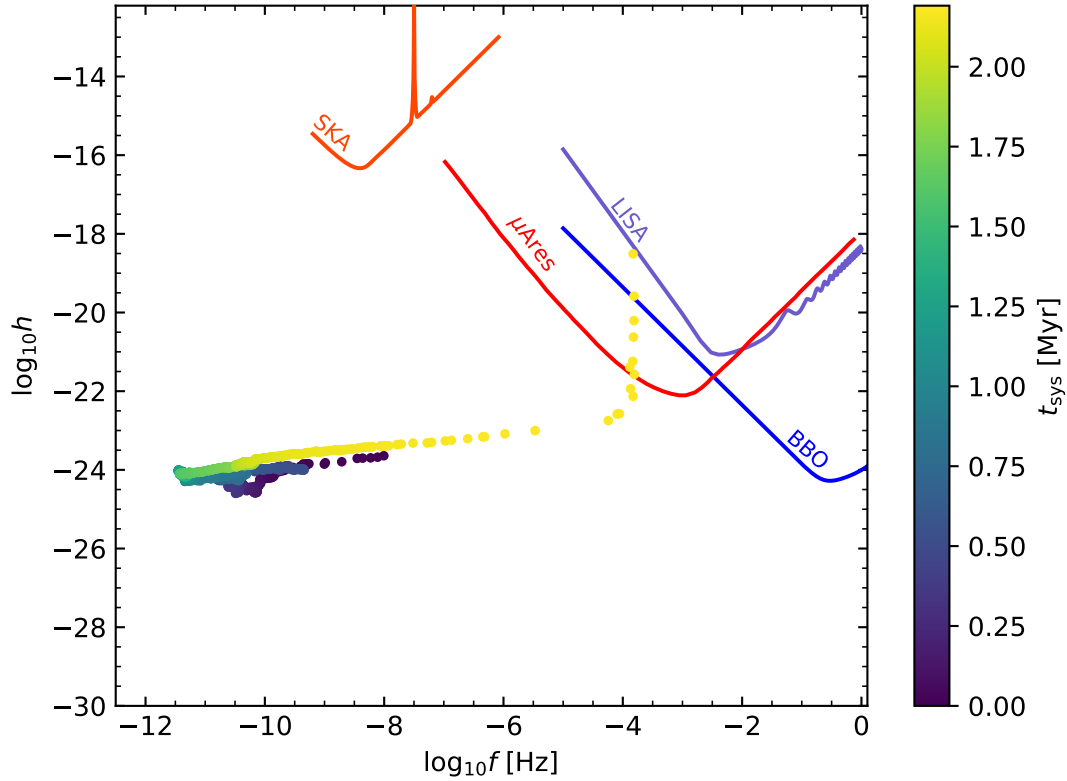**Figure 5.14:** Example of how binary systems induce the streak-like features present in our frequency vs. strain diagrams. The colour corresponds to the age of the binary system at a particular point. This particular binary formed in a `GRX` run.

5.4 Gravitational Wave Events

Before concluding the report, we extend our discussion of GW events and analyse events generated by transient events or binary systems in a NSC harbouring $10\sim20$ IMBH. Before discussing, we note several caveats to our analysis.

As alluded to earlier, detections are constrained by the resolution of the simulation, meaning we can only track events occurring at discrete time steps of $\delta t = 1000$ years. Events which occur in between these snapshots get ignored. Additionally, although events originating from a sustainable binary or hierarchical system in nature will emit a continuous signal, with the discrete sampling method adopted here, the same system may emit several GW events, and thus a single system may cause numerous events. Finally, we note that due to the $(1-e^2)^{-1.5}$ proportionality in equation 2.26, hyperbolic encounters ($e > 1$) are not detected. Since this is often the case during a fly-by, many events remain undetected, significantly influencing

the number of IMBH-IMBH events detected.

All in all, though this discussion is a good first step, it deserves its own investigation. Namely, we look at the global features of GW radiation and leave forecasting for future papers. Proceeding forwards, we note that the data here includes the complete duration of simulations. Comparing algorithms with these data will give a systematic bias towards `Hermite` due to its longer-lived binary and hierarchical systems.

Table 5.3 summarises the results for events satisfying $f > 10^{-12}$ Hz and $h > 10^{-30}$ in $N_{\mathrm{IMBH}} \in [10, 20]$ simulations, a value chosen to reflect the varying steady-state population potentially present in MW-like galaxies due to the fluctuation of IMBH infall rate. The events signify rates per Myr. Appendix G gives the full results.

	Hermite	GRX
Avg. Event Rate (IMBH-IMBH)	1.275×10^3	32.11
Avg. Event Rate (SMBH-IMBH)	1.410×10^4	2.546×10^4
Avg. Event Rate (Total)	1.538×10^4	2.549×10^4

Table 5.3: Summary of GW events. Values are averaged over all simulations. They signify the number of events (combined nearest neighbour and secondary nearest neighbour) per Myr for a MW-like galactic core composed of $N_{\mathrm{IMBH}} \in [10, 20]$.

Although limiting the frequency and strain removes a substantial amount of data, namely events induced by hierarchical systems and IMBH-IMBH transients, most of the information extracted would be redundant to what we have seen previously. Namely, figures 5.12 and F.1 tell us that hierarchical systems, or by extension IMBH-IMBH encounters with large a, generate the weaker signals. Nevertheless, the key takeaway from the table is that the majority of events detected using `GRX` are between SMBH-IMBH, whereas $\sim 10\%$ of those in `Hermite` are between two interacting IMBH's, even after constraining the strain.

The vast majority of `Hermite` IMBH-IMBH events are from interactions between secondary neighbour events (`GRX` showing slightly more nearest neighbour IMBH-IMBH events, see table G.1). Considering figure 5.4 shows that for fixed simulation times, `GRX` have their particles approach nearer with one another than `Hermite`, this result is surprising at first.

The discrepancy relates to the closer approaches `GRX` particles experience with the SMBH. As mentioned previously, in environments surrounding the SMBH, the orbital velocities of the particles take on relativistic speeds. In turn, this reduces the number of IMBH-IMBH trajectories with $e < 1$ since they are now more prone

to being hyperbolic. More explicitly, taking into account all eccentricities, we find that 84.5% of the tracked IMBH-IMBH encounters for `GRX` have $e > 1$. For `Hermite`, this reduces to 67.9%.
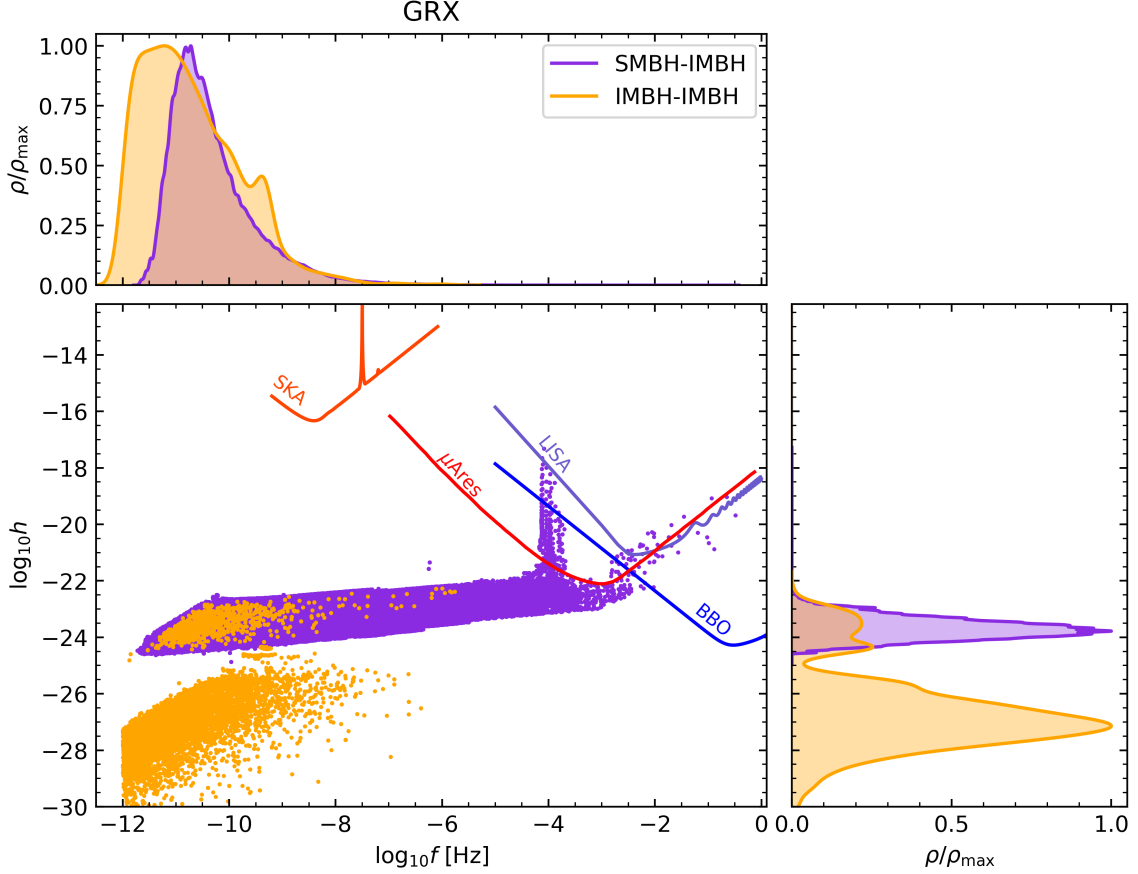
Figure 5.15: f vs. h diagram for GW events occuring in all $N_{\text{IMBH}} \leq 20$ `GRX` simulations. As before, overlayed on the plot are four different gravitational interferometers: Square Kilometer Array [124], μAres [78], LISA [71] and the Big Bang Observer [125]. All values assume $D_L = 1$ Mpc.

Figure 5.15 shows where in the frequency-strain parameter space GW events occur for `GRX`. Observe the vast majority of events lying outside the detectable range of GW interferometers. As alluded to before, this is due to the large semi-major axis of the interacting system. In turn, this decreases the frequency and strain (see equation 2.26 and equation 2.27, but also figures 5.16 and 5.17). Generally, SMBH-IMBH events cover a narrower area of parameter space and often exhibit larger frequencies and strains. This is partly due to the IMBH particles sinking into the SMBH potential well, reducing the semi-major axis over time, and partly from the

larger chirp mass of the SMBH-IMBH system.

The strain's kernel density (right panel) shows a bimodality in the emission of GW. Interestingly, when increasing the population to account for $N_{\text{IMBH}} \leq 40$, `Hermite` shows this feature, but `GRX` does not (see figure G.1 and figure G.2). Comparing data extracted for binary systems (figure 5.12) with the one above helps us understand why.

The gap featured in figure 5.15 coincides with the region right below that which binaries occupy. Furthermore, figure 5.12 does not include the SNN island located at $h \lesssim 10^{-26}$. Including transient events in this subsection, we allow ourselves to model weaker events explaining the emergence of the second peak at lower strains. By deduction, we can infer that the gap is due to a lack of events instigated by extremely soft binaries. That is, events generated by binaries which do not satisfy our earlier condition of what constitutes a binary but still have a small enough semi-major axis to generate large enough signals which otherwise bridge the gap. This region in semi-major axis space, though not small enough to induce binaries, encourages GW events and can be considered softer-than-soft binaries. In the case of figure 5.16, a binary lasting 20Myr populated the gap, given the low number of IMBH-IMBH events for `GRX` and this binary surviving for 2×10^4 snapshots, the persistent generation and detection of its events removed the bimodality. It is interesting to see such a soft binary last so long, especially in a dense system.

Another feature is the slanted 'Y' exhibited once SMBH-IMBH events reach the μAres range. To understand this, we compare the results in the figures here with those found in figure 5.13. As mentioned before, events following a nearly vertical ascent and forming a streak are those generated by hard binaries. By definition, these systems require a small semi-major axis so that they don't get disrupted by external encounters (recall equation 2.15). Since the strain spans similar values for either branch of the 'Y', we infer that events lying at the larger frequencies are those skimming past the SMBH and thus consist of large eccentricities and semi-major axis. A larger semi-major axis makes the systems easily disrupted and hence are not considered binaries with our conditions, explaining the omission of the second branch in our earlier figures shown in section 5.3.

Using results found in Kremer et al. (2019) [79], we can also conclude that the vertical ascent is formed by (hardened) binary systems that undergo GW capture. That is, the hardened binary merges over time after losing an enormous amount of its orbital energy in the form of GW radiation during a resonant encounter. Contrariwise, the events occurring on the gentle slope are due to in-cluster mergers. These are events where the binaries merge primarily due to dynamical encounters rather than GW radiation ([70]; [79]; [126]). These two classifications

help us understand why `Hermite` doesn't exhibit the vertical ascent, the GW capture branch, namely through its exclusion of 2.5PN terms. Furthermore, it helps us understand why figures focusing on binary systems showed a sparsely populated in-cluster branch, since, by definition, these events are not formed by binary systems but rather due to the dynamical encounters which shift their orbital parameters in the right way to have extremely large eccentricities and skim the SMBH.

5.4.1 Global Gravitational Wave Properties

Figure 5.16: Scatter plot denoting where `Hermite` and `GRX` IMBH-IMBH GW events lie in the a vs. $\log_{10}(1-e)$ parameter space. The panels above and on the right show the kernel density estimate. The greyed-out regions denote the frequency range probed by LISA and μAres. The dashed-dotted lines show where the sensitivity of the interferometers is at a maximum, while the dotted ones, the frequency range probed ([78]; [127]). Note that the upper bounds for μAres and LISA are the same ($f = 1$Hz). The data here is from runs simulated with $N_{\text{IMBH}} \leq 40$.

53

Analysing the induced GW events through a different perspective, figure 5.16 and figure 5.17 show where in semi-major axis - eccentricity space SMBH-IMBH and IMBH-IMBH events lie for simulations with $N_{\text{IMBH}} \leq 40$. The solid line denotes the region where merging events would take longer than the Hubble time to occur ($t_{\text{GW}} > t_H$) and those which would take shorter ($t_{\text{GW}} < t_H$) using equation 2.24 and assuming that the system doesn't get disrupted. The greyed out bands delineate the region in $(a, \log_{10}(1 - e))$ space observable by LISA and μAres. The dotted lines span their observational range, whereas the central dash-dot curve denotes the peak sensitivity ([78]; [127]). These curves neglect the frequency-dependent strain sensitivity of the interferometers and instead assume an ideal interferometer. We note that in both plots, the data extracted encompasses the complete simulation data, and isn't cropped to a constant time frame which otherwise removes systematic biases.
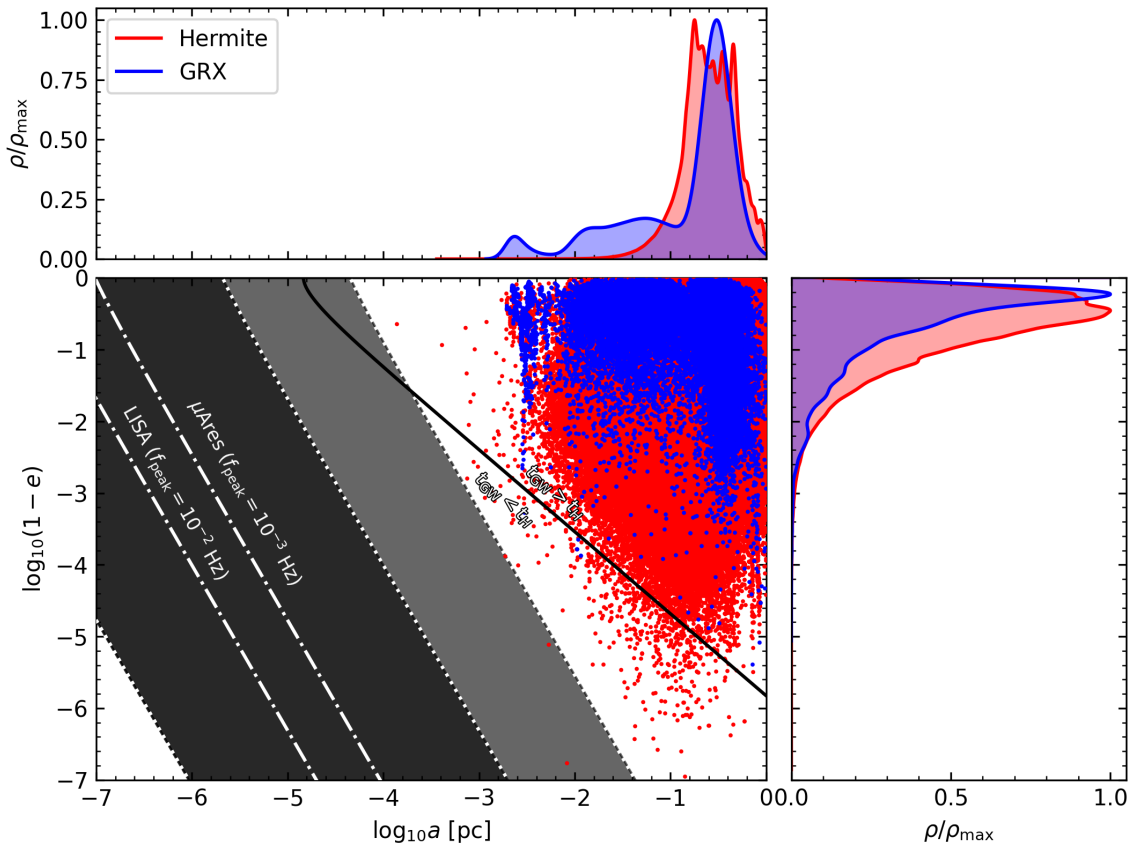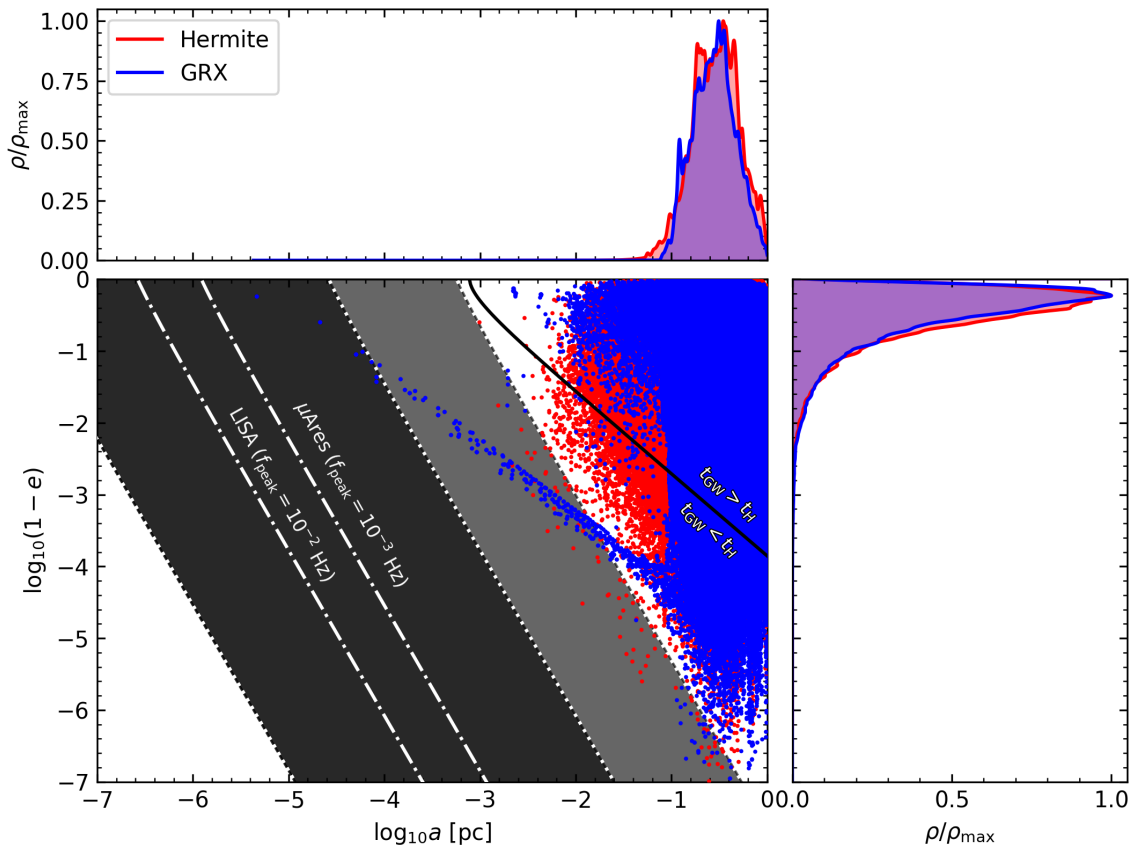

Figure 5.17: Scatter plot denoting where `Hermite` and `GRX` SMBH-IMBH GW events lie in the a vs. $\log_{10}(1 - e)$ parameter space.

From the plot, it is clear once more that an overwhelming amount of events lie outside the detectable range, and even if the systems resist disruption, their merging timescales are over the Hubble time. Furthermore, we see most events are due to particles with eccentricities between $0 \lesssim e \lesssim 0.9$ and semi-major axis $0.1 \lesssim a$ [pc] $\lesssim 1$. This is not surprising since figure 5.4 shows roughly 85% of the eccentricities tracked have $e \leq 0.9$.

In terms of differences, `Hermite` occupies a narrower range in semi-major axis values in both figures, with the differences more prominent for IMBH-IMBH events, once more relating to the ease of close approaches for binaries present in `GRX` through GW radiation. Contrariwise, the eccentricity found by `Hermite` covers a larger range for both IMBH-IMBH and SMBH-IMBH events. Though perhaps surprising, we note that even looking at the few IMBH-IMBH events with extreme eccentricities, the small collisional radii of the IMBH ($r_{\mathrm{coll}} = 0.01 R_\odot$) ensures that IMBH-IMBH mergers do not happen.

In terms of SMBH-IMBH events (figure 5.17), the larger eccentricities exhibited by `Hermite` is only a mild difference, and only occur for low~intermediate values of eccentricity, values not substantial enough to encourage merging events.

To wrap up, we note once more the fact that figure 5.17 nicely shows the streak formed by hard binaries observed for `GRX`. Here we see explicitly the evolution of such systems, whereby they initially have large e, drastically reducing the merging timescale. If it is left undisturbed by field particles, we observe that as the IMBH emits GW and its semi-major axis shrinks, it starts to circularise ($\log_{10}(1-e) \to 0$) with its semi-major axis reducing by several orders of magnitudes in the process. This is the GW capture mechanism in action. Furthermore, we see that in-cluster mergers tend to occupy relatively large a and extremely small $\log_{10}(1-e)$ regions, a region still detectable by the detectable region for μAres.

To conclude this section, we emphasise the necessity of PN terms to model clusters with compact objects. Though most of the time particles inhabiting clusters are far away from one, the presence of PN terms introduces a new avenue in which observable GW events may emerge, namely that of GW capture events. Modelling this is essential as it changes the simulation outcomes and with it, the predicted observables.

6 Conclusion

Black holes lie on the cutting edge of our understanding. Although some mysteries have started to unravel with the onset of GW astronomy, many remain. Observations of supermassive black holes lying at the heart of galaxies help us peer into galactic dynamics and evolution, yet their existence in the early Universe has contradicted our mathematical understandings, with their formation mechanism remaining unknown.

Lying between stellar-mass black holes and supermassive black holes, the currently undetected intermediate-mass black hole population may be the key to understanding the formation mechanism. In this report, we investigate the model proposed by Ebisuzaki et al. (2001) [1]. Here, intermediate-mass black holes formed in the hearts of dense globular clusters migrate inwards through dynamical friction, whereby a steady-state population of intermediate-mass black holes may exist in the galactic centre. Through their interactions, their orbital eccentricities may increase, reducing their merging timescales with the central supermassive black holes and alleviating several mathematical limits placed on the growth rate of supermassive black holes, namely the final parsec problem and the Eddington limit. Section 2 describes the model some more, followed by a discussion on the basics of N-body simulations in section 3. With the theory and methodology outlined, we explored the results in section 5.

Comparing the results between a Newtonian (`Hermite`) and a post-Newtonian (`GRX`) algorithm incorporating terms up to 2.5PN, we find that `GRX`, with its inclusion of gravitational wave radiation, predicts a survival time consistently one order of magnitude lower compared to its Newtonian counterpart for fixed populations. Differences in the results of either algorithm are further dissected throughout the section for which we note that the use of a PN algorithm is fundamental for a deeper understanding of relativistic systems, namely due to its introduction of a new GW formation channel.

When assuming the intermediate-mass black hole infall rate to the galactic core of $\tau = 7$ Myr [31], we predict that a population of $N_{\text{IMBH}} = 15\sim20$ intermediate-mass black holes reside within 0.4pc of Sagittarius A*, the supermassive black hole lying at the heart of our own galaxy. Forecasting the gravitational wave events observable by LISA [71] and μAres [78] based on such a steady-state environment, 926 supermassive black hole-intermediate-mass black hole merging events are detectable per year up to $z = 3$. This value is three orders of magnitude larger than other papers, but differences stem from the lack of constraints placed on the intermediate-mass black hole infall rate. Namely,

previous papers have assumed an infall rate of $\tau \sim 1$ Gyr ([2]; [3]; [4]; [5]).

Though a good first step, the investigation is rudimentary. Improvements in several aspects can provide more reliable results. The most noteworthy is the lack of an external nuclear star cluster potential. Inclusion of such would steepen the potential well, encouraging merging events to occur possibly resulting in a lowered steady-state population and would also reduce the number of observed ejections.

Additionally, time constraints limited the parameter space explored. Here, we assumed an equal mass intermediate-mass black hole initiated at a specific distance from the supermassive black hole when drawn from a Plummer distribution. Seeing how the intermediate-mass black hole mass influences results would be an interesting next step, with many of the phenomena present in cluster dynamics (relaxation time, mass segregation, binary formation...) all being dependent to a varying extent on the constituent mass.

Furthermore, though the supermassive black hole here has properties chosen to mimic that of Sagittarius A*, the analysis of such environments centred on a different supermassive black hole could be equally insightful and allow for a better way of generalising results. Not only would a change in its mass cause a change in the extent relativistic effects play a role, but it may influence the intermediate-mass black hole infall rate.

Similarly, though the initialised distances used here satisfy constraints placed by the Gravity Collaboration [110], these reflect the lower limits. Increasing their initial distances from the supermassive black hole would no doubt affect the survival time of the cluster and allow for a larger steady-state population of intermediate-mass black holes.

Amongst these considerations, future investigations may choose to probe the nature of ejection events. Introducing lower-mass objects into the cluster (such as stellar-mass black holes, intermediate-mass black holes or stars) should increase the ejection rate, and it could be insightful to analyse their trajectories and their final settled orbits. In fact, it has been observed that the old stellar population present in the Milky Way nuclear star cluster, those who've had more time to scatter with other objects, occupy a larger radius than the recently formed stellar population [122]. As shown here, intermediate-mass black holes can eject particles to large velocities, the mechanism of which could help alleviate this apparent separation between stellar populations.

Though neglected here, applying spin to the black hole populations could yield different results and may be worth taking a deeper look into. Previous results

show that, depending on the mass ratio of the interacting particles, eccentricities may enhance (when corotating with one another) or suppress (when counter-rotating) [128]. Lastly, although GW effects dissipate energy more efficiently than tidal effects, incorporating tidal effects may encourage the formation of intermediate-mass black hole-intermediate-mass black hole binary systems. It may be worth including the effect as, if the binary is tight enough, these systems also lie in detectable LISA and μAres range and could be an interesting and unique observable for such a system.

References

[1] T. Ebisuzaki, J. Makino, T. G. Tsuru, Y. Funato, S. Portegies Zwart, P. Hut, S. McMillan, S. Matsushita, H. Matsumoto, and R. Kawabe, *Missing Link Found? The "Runaway" Path to Supermassive Black Holes*, **562**, L19 (2001).

[2] F. Antonini, E. Barausse, and J. Silk, *The Coevolution of Nuclear Star Clusters, Massive Black Holes, and Their Host Galaxies*, **812**, 72 (2015).

[3] M. Arca-Sedda and R. Capuzzo-Dolcetta, *The MEGaN project – I. Missing formation of massive nuclear clusters and tidal disruption events by star clusters–massive black hole interactions*, Monthly Notices of the Royal Astronomical Society **471**, 478 (2017).

[4] A. Leveque, M. Giersz, M. Arca-Sedda, and A. Askar, *MOCCA-survey data base: extra galactic globular clusters - II. Milky Way and Andromeda*, **514**, 5751 (2022).

[5] G. Fragione, *Mergers of Supermassive and Intermediate-mass Black Holes in Galactic Nuclei from Disruptions of Star Clusters*, The Astrophysical Journal **939**, 97 (2022).

[6] A. Einstein, *Erklärung der Perihelbewegung des Merkur aus der allgemeinen Relativitätstheorie*, Sitzungsberichte der Königlich Preussischen Akademie der Wissenschaften , 831 (1915).

[7] J. R. Oppenheimer and H. Snyder, *On Continued Gravitational Contraction*, Phys. Rev. **56**, 455 (1939).

[8] and J Aasi et al., *Advanced LIGO*, Classical and Quantum Gravity **32**, 074001 (2015).

[9] A. M. Ghez, B. L. Klein, M. Morris, and E. E. Becklin, *High Proper-Motion Stars in the Vicinity of Sagittarius A*: Evidence for a Supermassive Black Hole at the Center of Our Galaxy*, The Astrophysical Journal **509**, 678 (1998).

[10] L. Ferrarese and D. Merritt, *A Fundamental Relation between Supermassive Black Holes and Their Host Galaxies*, **539**, L9 (2000).

[11] J. Binney and S. Tremaine, *Galactic Dynamics: Second Edition*, 2008.

[12] J. Kormendy and L. C. Ho, *Coevolution (Or Not) of Supermassive Black Holes and Host Galaxies*, Annual Review of Astronomy and Astrophysics **51**, 511 (2013).

[13] R. Schödel, A. Feldmeier, D. Kunneriath, S. Stolovy, N. Neumayer, P. Amaro-Seoane, and S. Nishiyama, *Surface brightness profile of the Milky Way's nuclear star cluster*, **566**, A47 (2014).

[14] A. Askar, M. B. Davies, and R. P. Church, *Formation of supermassive black holes in galactic nuclei – I. Delivering seed intermediate-mass black holes in massive stellar clusters*, Monthly Notices of the Royal Astronomical Society **502**, 2682 (2021).

[15] T. E. H. T. Collaboration et al., *First M87 Event Horizon Telescope Results. I. The Shadow of the Supermassive Black Hole*, The Astrophysical Journal Letters **875**, L1 (2019).

[16] E. H. T. Collaboration et al., *First Sagittarius A* Event Horizon Telescope Results. I. The Shadow of the Supermassive Black Hole in the Center of the Milky Way*, The Astrophysical Journal Letters **930**, L12 (2022).

[17] P. Madau and M. J. Rees, *Massive Black Holes as Population III Remnants*, **551**, L27 (2001).

[18] S. F. P. Zwart and S. L. W. McMillan, *The Runaway Growth of Intermediate-Mass Black Holes in Dense Star Clusters*, The Astrophysical Journal **576**, 899 (2002).

[19] M. Giersz, N. Leigh, A. Hypki, N. Lützgendorf, and A. Askar, *MOCCA code for star cluster simulations – IV. A new scenario for intermediate mass black hole formation in globular clusters*, Monthly Notices of the Royal Astronomical Society **454**, 3150 (2015).

[20] J. Bellovary, F. Governato, T. Quinn, J. Wadsley, S. Shen, and a. Volonteri, *Wandering Black Holes in Bright Disk Galaxy Halos*, The Astrophysical Journal Letters **721**, L148 (2010).

[21] B. McKernan, K. E. S. Ford, W. Lyra, and H. B. Perets, *Intermediate mass black holes in AGN discs – I. Production and growth*, Monthly Notices of the Royal Astronomical Society **425**, 460 (2012).

[22] M. C. Begelman, R. D. Blandford, and M. J. Rees, *Massive black hole binaries in active galactic nuclei*, **287**, 307 (1980).

[23] B. P. Abbott et al., *Observation of Gravitational Waves from a Binary Black Hole Merger*, **116**, 061102 (2016).

[24] and R. Abuter et al., *A geometric distance measurement to the Galactic center black hole with 0.3% uncertainty*, Astronomy &amp Astrophysics **625**, L10 (2019).

[25] R. Abbott et al., *GW190521: A Binary Black Hole Merger with a Total Mass of 150 $M_\odot$*, **125**, 101102 (2020).

[26] V. Bromm, P. S. Coppi, and R. B. Larson, *The Formation of the First Stars. I. The Primordial Star-forming Cloud*, **564**, 23 (2002).

[27] G. Lodato and P. Natarajan, *Supermassive black hole formation during the assembly of pre-galactic discs*, **371**, 1813 (2006).

[28] M. Mapelli, N. Giacobbo, E. Ripamonti, and M. Spera, *The cosmic merger rate of stellar black hole binaries from the Illustris simulation*, **472**, 2422 (2017).

[29] Y. Taniguchi, Y. Shioya, T. G. Tsuru, and S. Ikeuchi, *Formation of Intermediate-Mass Black Holes in Circumnuclear Regions of Galaxies*, Publications of the Astronomical Society of Japan **52**, 533 (2000).

[30] M. C. Miller and D. P. Hamilton, *Four-Body Effects in Globular Cluster Black Hole Coalescence*, **576**, 894 (2002).

[31] S. F. Portegies Zwart, H. Baumgardt, S. L. W. McMillan, J. Makino, P. Hut, and T. Ebisuzaki, *The Ecology of Star Clusters and Intermediate-Mass Black Holes in the Galactic Bulge*, **641**, 319 (2006).

[32] J. Silk and J. Arons, *On the nature of the globular cluster X-ray sources.*, **200**, L131 (1975).

[33] J. Strader, L. Chomiuk, T. J. Maccarone, J. C. A. Miller-Jones, and A. C. Seth, *Two stellar-mass black holes in the globular cluster M22*, Nature **490**, 71 (2012).

[34] B. Lanzoni, A. Mucciarelli, L. Origlia, M. Bellazzini, F. R. Ferraro, E. Valenti, P. Miocchi, E. Dalessandro, C. Pallanca, and D. Massari, *The Velocity Dispersion Profile of NGC 6388 from Resolved-star Spectroscopy: No Evidence of a Central Cusp and New Constraints on the Black Hole Mass*, **769**, 107 (2013).

[35] M. Mezcua, *Observational evidence for intermediate-mass black holes*, International Journal of Modern Physics D **26**, 1730021 (2017).

[36] E. Bañados, B. P. Venemans, C. Mazzucchelli, E. P. Farina, F. Walter, F. Wang, R. Decarli, D. Stern, X. Fan, F. B. Davies, J. F. Hennawi, R. A. Simcoe, M. L. Turner, H.-W. Rix, J. Yang, D. D. Kelson, G. C. Rudie, and J. M. Winters, *An 800-million-solar-mass black hole in a significantly neutral Universe at a redshift of 7.5*, Nature **553**, 473 (2017).

[37] S. Chandrasekhar, *Dynamical Friction. I. General Considerations: the Coefficient of Dynamical Friction.*, **97**, 255 (1943).

[38] L. Spitzer, *Dynamical evolution of globular clusters*, 1987.

[39] M. Giersz and D. C. Heggie, *Statistics of N-Body Simulations - Part One - Equal Masses Before Core Collapse*, **268**, 257 (1994).

[40] E. Por, *Post-Newtonian N -body Dynamics*, (2014).

[41] M. G. Haehnelt, *Low-frequency gravitational waves from supermassive black holes*, Monthly Notices of the Royal Astronomical Society **269**, 199 (1994).

[42] M. Valtonen, H. Lehto, K. Kokkonen, and S. Mikkola, *The 0J287 Binary Model and the November 1995 Outburst*, in *Blazar Continuum Variability*, edited by H. R. Miller, J. R. Webb, and J. C. Noble, volume 110 of *Astronomical Society of the Pacific Conference Series*, page 93, 1996.

[43] A. Gould and H.-W. Rix, *Binary Black Hole Mergers from Planet-like Migrations*, **532**, L29 (2000).

[44] M. Milosavljević and D. Merritt, *Formation of Galactic Nuclei*, **563**, 34 (2001).

[45] M. Milosavljevic
, *The Final Parsec Problem*, in *AIP Conference Proceedings*, AIP, 2003.

[46] N. Neumayer, A. Seth, and T. Böker, *Nuclear star clusters*, **28**, 4 (2020).

[47] E. Gallego-Cano, R. Schödel, H. Dong, F. Nogueras-Lara, A. T. Gallego-Calvente, P. Amaro-Seoane, and H. Baumgardt, *The distribution of stars around the Milky Way's central black hole. I. Deep star counts*, **609**, A26 (2018).

[48] H. H. Loose, E. Kruegel, and A. Tutukov, *Bursts of star formation in the galactic centre*, **105**, 342 (1982).

[49] M. Milosavljević, *On the Origin of Nuclear Star Clusters in Late-Type Spiral Galaxies*, **605**, L13 (2004).

[50] D. Aharon and H. B. Perets, *FORMATION AND EVOLUTION OF NUCLEAR STAR CLUSTERS WITH IN SITU STAR FORMATION: NUCLEAR CORES AND AGE SEGREGATION*, The Astrophysical Journal **799**, 185 (2015).

[51] S. D. Tremaine, J. P. Ostriker, and J. Spitzer, L., *The formation of the nuclei of galaxies. I. M31.*, **196**, 407 (1975).

[52] R. Capuzzo-Dolcetta, *The Evolution of the Globular Cluster System in a Triaxial Galaxy: Can a Galactic Nucleus Form by Globular Cluster Capture?*, **415**, 616 (1993).

[53] M. Agarwal and M. Milosavljević, *Nuclear Star Clusters from Clustered Star Formation*, **729**, 35 (2011).

[54] R. Schödel, F. Nogueras-Lara, E. Gallego-Cano, B. Shahzamanian, A. T. Gallego-Calvente, and A. Gardini, *The Milky Way's nuclear star cluster: Old, metal-rich, and cuspy. Structure and star formation history from deep imaging*, **641**, A102 (2020).

[55] G. D. Quinlan, *The dynamical evolution of massive black hole binaries I. Hardening in a fixed stellar background*, New Astronomy **1**, 35 (1996).

[56] S. Portegies Zwart and S. McMillan, *Astrophysical Recipes; The art of AMUSE*, 2018.

[57] J. G. Hills, *Hyper-velocity and tidal stars from binaries disrupted by a massive Galactic black hole*, Nature **331**, 687 (1988).

[58] S. E. Koposov, D. Boubert, T. S. Li, D. Erkal, G. S. D. Costa, D. B. Zucker, A. P. Ji, K. Kuehn, G. F. Lewis, D. Mackey, J. D. Simpson, N. Shipp, Z. Wan, V. Belokurov, J. Bland-Hawthorn, S. L. Martell, T. Nordlander, A. B. Pace, G. M. D. Silva, and M.-Y. W. and, *Discovery of a nearby 1700 km s-1 star ejected from the Milky Way by Sgr A**, Monthly Notices of the Royal Astronomical Society **491**, 2465 (2019).

[59] J. Spitzer, Lyman, *The stability of isolated clusters*, **100**, 396 (1940).

[60] J. G. Hills, *Encounters between Single and Binary Stars: The Effect of Intruder Mass on the Maximum Impact Velocity for Which the Mean Change in Binding Energy is Positive*, **99**, 979 (1990).

[61] J. G. Hills, *Effects of Intruder Mass on Collisions With Hard Binaries. II. Dependence on Impact Parameter and Computations of the Interaction Cross Section*, **103**, 1955 (1992).

[62] J. Samsing and T. Ilan, *Topology of black hole binary–single interactions*, Monthly Notices of the Royal Astronomical Society **476**, 1548 (2018).

[63] N. C. Weatherford, F. Kıroğlu, G. Fragione, S. Chatterjee, K. Kremer, and F. A. Rasio, *Stellar Escape from Globular Clusters I: Escape Mechanisms and Properties at Ejection*, 2022.

[64] R. A. Mardling and S. J. Aarseth, *Tidal interactions in star cluster simulations*, **321**, 398 (2001).

[65] Y. Kozai, *Secular perturbations of asteroids with high inclination and eccentricity*, **67**, 591 (1962).

[66] M. L. Lidov, *The evolution of orbits of artificial satellites of planets under the action of gravitational perturbations of external bodies*, **9**, 719 (1962).

[67] S. Naoz, *The Eccentric Kozai-Lidov Effect and Its Applications*, Annual Review of Astronomy and Astrophysics **54**, 441 (2016).

[68] G. Fragione and N. Leigh, *Intermediate-mass ratio inspirals in galactic nuclei*, Monthly Notices of the Royal Astronomical Society **480**, 5160 (2018).

[69] S. Naoz, B. Kocsis, A. Loeb, and N. Yunes, *RESONANT POST-NEWTONIAN ECCENTRICITY EXCITATION IN HIERARCHICAL THREE-BODY SYSTEMS*, The Astrophysical Journal **773**, 187 (2013).

[70] C. L. Rodriguez, P. Amaro-Seoane, S. Chatterjee, K. Kremer, F. A. Rasio, J. Samsing, C. S. Ye, and M. Zevin, *Post-Newtonian dynamics in dense star clusters: Formation, masses, and merger rates of highly-eccentric black hole binaries*, Physical Review D **98** (2018).

[71] P. Amaro-Seoane et al., *Laser Interferometer Space Antenna*, arXiv e-prints , arXiv:1702.00786 (2017).

[72] M. Maggiore, *Gravitational Waves: Volume 1: Theory and Experiments*, Gravitational Waves, OUP Oxford, 2008.

[73] S. M. Carroll, *Spacetime and geometry. An introduction to general relativity*, 2004.

[74] C. W. Misner, K. S. Thorne, J. A. Wheeler, and D. I. Kaiser, *Gravitation*, 2018.

[75] P. C. Peters, *Gravitational Radiation and the Motion of Two Point Masses*, Phys. Rev. **136**, B1224 (1964).

[76] P. C. Peters and J. Mathews, *Gravitational Radiation from Point Masses in a Keplerian Orbit*, Physical Review **131**, 435 (1963).

[77] L. Wen, *On the Eccentricity Distribution of Coalescing Black Hole Binaries Driven by the Kozai Mechanism in Globular Clusters*, The Astrophysical Journal **598**, 419 (2003).

[78] A. Sesana et al., *Unveiling the gravitational universe at μ-Hz frequencies*, Experimental Astronomy **51**, 1333 (2021).

[79] K. Kremer, C. L. Rodriguez, P. Amaro-Seoane, K. Breivik, S. Chatterjee, M. L. Katz, S. L. Larson, F. A. Rasio, J. Samsing, C. S. Ye, and M. Zevin, *Post-Newtonian dynamics in dense star clusters: Binary black holes in the LISA band*, Physical Review D **99** (2019).

[80] B. Willems, V. Kalogera, A. Vecchio, N. Ivanova, F. A. Rasio, J. M. Fregeau, and K. Belczynski, *Eccentric Double White Dwarfs as iLISA/i Sources in Globular Clusters*, The Astrophysical Journal **665**, L59 (2007).

[81] D. J. D'Orazio and J. Samsing, *Black hole mergers from globular clusters observable by LISA II. Resolved eccentric sources and the gravitational wave background*, Monthly Notices of the Royal Astronomical Society **481**, 4775 (2018).

[82] S. Portegies Zwart et al., *A multiphysics and multiscale software environment for modeling astrophysical systems*, **14**, 369 (2009).

[83] S. Portegies Zwart, S. L. W. McMillan, E. van Elteren, I. Pelupessy, and N. de Vries, *Multi-physics simulations using a hierarchical interchangeable software interface*, Computer Physics Communications **184**, 456 (2013).

[84] F. I. Pelupessy, A. van Elteren, N. de Vries, S. L. W. McMillan, N. Drost, and S. F. Portegies Zwart, *The Astrophysical Multipurpose Software Environment*, **557**, A84 (2013).

[85] I. Newton, *Philosophiae Naturalis Principia Mathematica.*, 1687.

[86] H. Poincaré, *Les méthodes nouvelles de la mécanique céleste*, 1892.

[87] A. Einstein, L. Infeld, and B. Hoffmann, *The Gravitational Equations and the Problem of Motion*, Annals of Mathematics **39**, 65 (1938).

[88] K. Schwarzschild, *On the Gravitational Field of a Mass Point According to Einstein's Theory*, Abh. Konigl. Preuss. Akad. Wissenschaften Jahre 1906,92, Berlin,1907 **1916**, 189 (1916).

[89] C. M. Will, *Incorporating post-Newtonian effects in N-body dynamics*, Physical Review D **89** (2014).

[90] K. P. Rauch and S. Tremaine, *Resonant relaxation in stellar systems*, **1**, 149 (1996).

[91] T. Futamase and Y. Itoh, *The post-Newtonian approximation for relativistic compact binaries*, Living Rev. Rel. **10**, 2 (2007).

[92] Y. Itoh, T. Futamase, and H. Asada, *Equation of motion for relativistic compact binaries with the strong field point particle limit: The second and half post-Newtonian order*, Physical Review D **63** (2001).

[93] T. C. N. Boekholt, A. Moerman, and S. F. Portegies Zwart, *Relativistic Pythagorean three-body problem*, **104**, 083020 (2021).

[94] J. Makino, *Optimal Order and Time-Step Criterion for Aarseth-Type N-Body Integrators*, **369**, 200 (1991).

[95] J. Makino and S. J. Aarseth, *On a Hermite Integrator with Ahmad-Cohen Scheme for Gravitational Many-Body Problems*, **44**, 141 (1992).

[96] S. F. Portegies Zwart, T. C. N. Boekholt, E. H. Por, A. S. Hamers, and S. L. W. McMillan, *Chaos in self-gravitating many-body systems. Lyapunov time dependence of N and the influence of general relativity*, **659**, A86 (2022).

[97] L. Verlet, *Computer "Experiments" on Classical Fluids. I. Thermodynamical Properties of Lennard-Jones Molecules*, Phys. Rev. **159**, 98 (1967).

[98] T. Boekholt and S. Portegies Zwart, *On the reliability of N-body simulations*, Computational Astrophysics and Cosmology **2**, 2 (2015).

[99] P. Hut, J. Makino, and S. McMillan, *Building a Better Leapfrog*, **443**, L93 (1995).

[100] P. Kustaanheimo, A. Schinzel, H. Davenport, and E. Stiefel, *Perturbation theory of Kepler motion based on spinor regularization.*, **1965**, 204 (1965).

[101] S. Mikkola and K. Tanikawa, *Algorithmic regularization of the few-body problem*, Monthly Notices of the Royal Astronomical Society **310**, 745 (1999).

[102] S. Mikkola and D. Merritt, *Algorithmic regularization with velocity-dependent forces*, **372**, 219 (2006).

[103] J. Waldvogel, *Quaternions for regularizing Celestial Mechanics: The right way*, Celestial Mech. Dynam. Astronom. **102**, 149 (2008).

[104] O. Gerhard, *The Galactic Center HE I Stars: Remains of a Dissolved Young Cluster?*, **546**, L39 (2001).

[105] Q. Yu and S. Tremaine, *Ejection of Hypervelocity Stars by the (Binary) Black Hole in the Galactic Center*, The Astrophysical Journal **599**, 1129 (2003).

[106] M. J. Reid and A. Brunthaler, *The Proper Motion of Sagittarius A*. II. The Mass of Sagittarius A**, The Astrophysical Journal **616**, 872 (2004).

[107] A. Gualandris, S. Gillessen, and D. Merritt, *The Galactic Centre star S2 as a dynamical probe for intermediate-mass black holes*, Monthly Notices of the Royal Astronomical Society **409**, 1146 (2010).

[108] S. Naoz, C. M. Will, E. Ramirez-Ruiz, A. Hees, A. M. Ghez, and T. Do, *A Hidden Friend for the Galactic Center Black Hole, Sgr A**, The Astrophysical Journal **888**, L8 (2019).

[109] M. J. Reid and A. Brunthaler, *The Proper Motion of Sagittarius A*. III. The Case for a Supermassive Black Hole*, The Astrophysical Journal **892**, 39 (2020).

[110] R. Abuter et al., *Detection of the Schwarzschild precession in the orbit of the star S2 near the Galactic centre massive black hole*, Astronomy &amp Astrophysics **636**, L5 (2020).

[111] H. C. Plummer, *On the problem of distribution in globular star clusters*, **71**, 460 (1911).

[112] J. N. Bahcall and R. A. Wolf, *Star distribution around a massive black hole in a globular cluster*, ApJ **209**, 214 (1976).

[113] A. M. Ghez, S. Salim, N. N. Weinberg, J. R. Lu, T. Do, J. K. Dunn, K. Matthews, M. R. Morris, S. Yelda, E. E. Becklin, T. Kremenek, M. Milosavljevic, and J. Naiman, *Measuring Distance and Properties of the Milky Way's Central Supermassive Black Hole with Stellar Orbits*, The Astrophysical Journal **689**, 1044 (2008).

[114] R. Genzel, F. Eisenhauer, and S. Gillessen, *The Galactic Center massive black hole and nuclear star cluster*, Reviews of Modern Physics **82**, 3121 (2010).

[115] T. C. Licquia and J. A. Newman, *Improved Estimates of the Milky Way's stellar mass and star formation rate from hierarchical Bayesian meta-analysis*, The Astrophysical Journal **806**, 96 (2015).

[116] M. Furlong, R. G. Bower, T. Theuns, J. Schaye, R. A. Crain, M. Schaller, C. Dalla Vecchia, C. S. Frenk, I. G. McCarthy, J. Helly, A. Jenkins, and Y. M. Rosas-Guevara, *Evolution of galaxy stellar masses and star formation rates in the EAGLE simulations*, **450**, 4486 (2015).

[117] N. Aghanim et al., *iPlanck/i2018 results*, Astronomy &amp Astrophysics **641**, A6 (2020).

[118] M. Arca-Sedda and A. Gualandris, *Gravitational wave sources from inspiralling globular clusters in the Galactic Centre and similar environments*, **477**, 4423 (2018).

[119] M. Arca-Sedda and R. Capuzzo-Dolcetta, *The MEGaN project II. Gravitational waves from intermediate-mass and binary black holes around a supermassive black hole*, **483**, 152 (2019).

[120] R. Capuzzo-Dolcetta and I. Tosta e Melo, *On the relation between the mass of Compact Massive Objects and their host galaxies*, Monthly Notices of the Royal Astronomical Society **472**, 4013 (2017).

[121] J. Bovy, *galpy: A python Library for Galactic Dynamics*, **216**, 29 (2015).

[122] X. Chen and F. K. Liu, *IS THERE AN INTERMEDIATE MASSIVE BLACK HOLE IN THE GALACTIC CENTER: IMPRINTS ON THE STELLAR TIDAL-DISRUPTION RATE*, The Astrophysical Journal **762**, 95 (2012).

[123] *Dynamics of star clusters: proceedings of IAU 113th Symposium no. 113 held in Princeton, New Jersey, U.S.A., 29 May-1 June, 1984.*, volume 113, 1985.

[124] R. Smits, M. Kramer, B. Stappers, D. R. Lorimer, J. Cordes, and A. Faulkner, *Pulsar searches and timing with the square kilometre array*, **493**, 1161 (2009).

[125] G. M. Harry, P. Fritschel, D. A. Shaddock, W. Folkner, and E. S. Phinney, *Laser interferometry for the Big Bang Observer*, Classical and Quantum Gravity **23**, 4887 (2006).

[126] J. Samsing and D. J. D'Orazio, *Black Hole Mergers From Globular Clusters Observable by LISA I: Eccentric Sources Originating From Relativistic N-body Dynamics*, Monthly Notices of the Royal Astronomical Society **481**, 5445 (2018).

[127] J. Samsing, M. MacLeod, and E. Ramirez-Ruiz, *The Formation of Eccentric Compact Binary Inspirals and the Role of Gravitational Wave Emission in Binary-Single Stellar Encounters*, The Astrophysical Journal **784**, 71 (2014).

[128] A. Rasskazov, G. Fragione, N. W. C. Leigh, H. Tagawa, A. Sesana, A. Price-Whelan, and E. M. Rossi, *Hypervelocity Stars from a Supermassive Black Hole–Intermediate-mass Black Hole Binary*, The Astrophysical Journal **878**, 17 (2019).

[129] D. M. Hernandez, S. Hadden, and J. Makino, *Are long-term N-body simulations reliable?*, **493**, 1913 (2020).

Appendix A: Chaos in N-body Systems

In $N > 2$ body systems, any slight change in initial conditions will drastically influence the final results due to its chaotic nature. Being chaotic, one cannot use individual N-body simulations to gather meaningful interpretations. Instead, one conducts several simulations and analyses its global properties such runs yielded with the assumption that this shows an accurate representation of such systems ([98]; [129]). In the context of this report, due to the parallelisation scheme, numerical errors were essentially random. In turn, final results varied between simulations, even when initialised with identical conditions, hence the need for multiple simulations.

To understand this better in this context, we note that although identical conditions should provide equivalent results due to the deterministic nature of computers, this isn't the case here due to the parallelisation scheme forcing different cores (and subsequently threads) to compute different segments of a given simulation at different times depending on the computational resources available. Since each core has a unique intrinsic numerical error attributed to it, two individual simulations will not show the same results. Figure A.1 in the following page shows an example in which various properties of identical particles are tracked in two separate simulation runs. Note that the curves in the bottom two panels denote averages over time.

As seen, a many-body system is sensitive to any input making even numerical round-off errors have consequential effects at later times. The larger the system, the more sensitive the system is to numerical errors and initial conditions. This difference is illustrated in the top right of figure A.1, which shows the deviation in the phase-space coordinates over time. The expression used was taken from Portegies Zwart (2021) [96]:

$$\ln[\delta w(\vec{r}, \vec{v})] = \frac{1}{2} \ln \left[\sum \left((\vec{r}_i - \vec{r}_j)^2 + (\vec{v}_i - \vec{v}_j)^2 \right) \right] \tag{A.1}$$

Here i and j denote the two particles. The sensitivity of N-body systems towards the initial conditions cause individual simulations of N-body systems to be inaccurate when representing real-life situations since precise initial conditions relevant to different environments are difficult to come by.
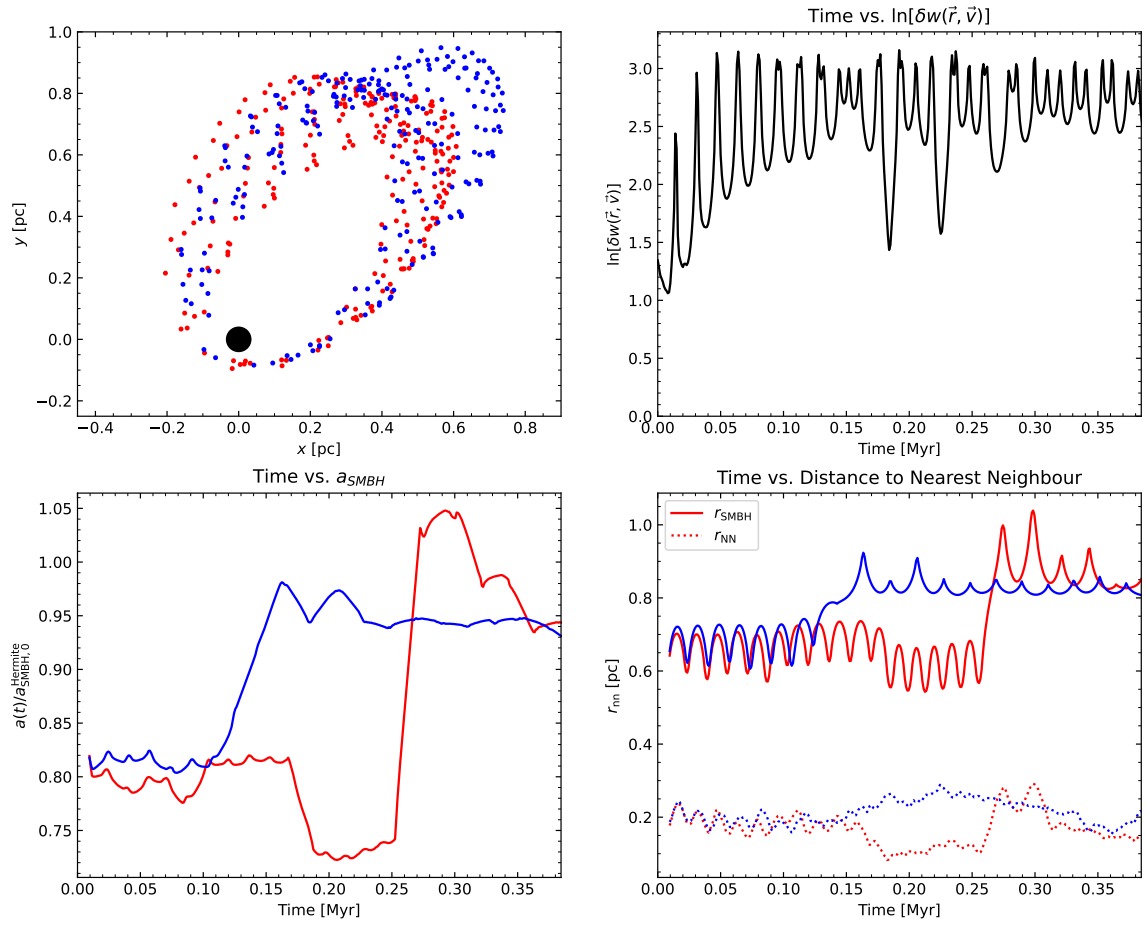
Figure A.1: Top left: System evolution in the *xy*-plane using `Hermite` of the same particle in the same configuration for two different runs, distinguished by their colour. Top right: Deviations in the phase-space coordinates of the particle. Bottom left: Evolution of the particle's semi-major axis with respect to the central SMBH. Bottom right: The evolution of distance of the IMBH particle with respect to the SMBH (solid) and its nearest neighbour (dashed).

Appendix B: HermiteGRX Post-Newtonian Terms

The EIH expression including the 2.5PN term used by GRX is shown below.

$$
\begin{aligned}
\vec{a}_A = & -\sum_{B\neq A} \frac{Gm_B \vec{x}_{AB}}{r_{AB}^3} - \sum_b \frac{Gm_b \vec{x}_{Ab}}{r_{Ab}^3} \\
& + G\frac{1}{c^2} \sum_{B\neq A} \frac{m_B \vec{x}_{AB}}{r_{AB}^3} \Bigg[\frac{4m_B}{r_{AB}} + \frac{5m_A}{r_{AB}} + \sum_{C\neq A,B} \frac{m_C}{r_{BC}} + \sum_c \frac{m_c}{r_{Bc}} + 4\sum_{C\neq A,B} \frac{m_C}{r_{AC}} \\
& + 4\sum_c \frac{m_c}{r_{Ac}} - \frac{1}{2} \sum_{C\neq A,B} \frac{m_C}{r_{BC}^3} (\vec{x}_{AB}\cdot \vec{x}_{BC}) + G^{-1}\left(4(\vec{v}_A\cdot\vec{v}_B) - 2v_B^2 + \frac{3}{2}(\vec{v}_B\cdot\vec{n}_{AB})^2 - v_A^2\right) \Bigg] \\
& + G\frac{1}{c^2} \sum_b \frac{m_b \vec{x}_{Ab}}{r_{Ab}^3} \Bigg[\frac{4m_b}{r_{Ab}} + \frac{5m_A}{r_{Ab}} + \sum_{C\neq A} \frac{m_C}{r_{bC}} + \sum_{c\neq b} \frac{m_c}{r_{bc}} + 4\sum_{C\neq A} \frac{m_C}{r_{AC}} \\
& + 4\sum_{c\neq b} \frac{m_c}{r_{Ac}} - \frac{1}{2} \sum_{C\neq A} \frac{m_C}{r_{bC}^3} (\vec{x}_{Ab}\cdot \vec{x}_{bC}) + G^{-1}\left(4(\vec{v}_A\cdot\vec{v}_b) - 2v_b^2 + \frac{3}{2}(\vec{v}_b\cdot\vec{n}_{Ab})^2 - v_A^2\right) \Bigg] \\
& - \frac{7}{2c^2} \Bigg(\sum_{B\neq A} \frac{Gm_B}{r_{AB}} \Bigg[\sum_{C\neq A,B} \frac{Gm_C \vec{x}_{BC}}{r_{BC}^3} + \sum_c \frac{Gm_c \vec{x}_{Bc}}{r_{Bc}^3} \Bigg] + \sum_b \frac{Gm_b}{r_{Ab}} \Bigg[\sum_{C\neq A} \frac{Gm_C \vec{x}_{bC}}{r_{bC}^3} \\
& + \sum_{b\neq c} \frac{Gm_c \vec{x}_{bc}}{r_{bc}^3} \Bigg] \Bigg) + \frac{1}{c^2} \Bigg[\sum_{B\neq A} \frac{Gm_B}{r_{AB}^3} \vec{x}_{AB}\cdot (4\vec{v}_A - 3\vec{v}_B)\vec{v}_{AB} + \sum_b \frac{Gm_b}{r_{Ab}^3} \vec{x}_{Ab}\cdot(4\vec{v}_A - 3\vec{v}_b)\vec{v}_{Ab} \Bigg] \\
& + \frac{1}{c^5} \sum_{A\neq B} \frac{4}{5} \frac{G^2 m_A m_B}{r_{AB}^3} \Bigg[\vec{v}_{AB}\left(\frac{2Gm_A}{r_{AB}} - \frac{8Gm_B}{r_{AB}} - v_{AB}^2 \right) \\
& \qquad + \vec{r}_{AB}(\hat{\vec{r}}_{AB}\cdot\vec{v}_{AB})\left(\frac{52Gm_B}{3r_{AB}} - \frac{6Gm_A}{r_{AB}} + 3v_{AB}^2 \right) \Bigg] + \mathcal{O}(c^{-6}) \qquad\text{(B.1)}
\end{aligned}
$$

Where, $\hat{\vec{r}} = \frac{\vec{r}_{AB}}{|r_{AB}|}$. The expression above shows the PN equation of motion followed by a massive particle, A. The less massive particles (in our case, IMBH) have their equations of motion expressed equivalently, the only difference being the exchange of upper case with lower case letters since these correspond to massive (upper-case) and less-massive particles thanks to the symmetry of the derivation [40]. Note that the first term is of Newtonian order, while the following three describe 1PN corrections, $\mathcal{O}(c^{-2})$.

It is insightful to look at the 2.5PN term in expression B.1. If we restrict ourselves to circular orbits then $\hat{\vec{r}}_{AB}\cdot\vec{v}_{AB} = 0$. Taking equal mass objects ($m_A = m_B = m$)

then the 2.5PN term reduces into:

$$\vec{a}_{2.5\text{PN}} = \frac{1}{c^5} \sum_{A \neq B} \frac{4}{5} \frac{G^2 m^2}{r_{AB}^3} \left[\vec{v}_{AB} \left(\frac{2Gm}{r_{AB}} - \frac{8Gm}{r_{AB}} - v_{AB}^2 \right) \right.$$
$$\left. + \vec{r}_{AB} (\hat{r}_{AB} \cdot \vec{v}_{AB} \left(\frac{52Gm}{3r_{AB}} - \frac{6Gm}{r_{AB}} + 3v_{AB}^2 \right) \right] \tag{B.2}$$

Substituting the form for circular velocity:

$$v_{\text{circ}} = \sqrt{\frac{Gm}{r}} \tag{B.3}$$

we get that:

$$\vec{a}_{2.5\text{PN}} = \frac{4}{5} \frac{G^2 m^2}{r_{AB}^3} \left(\frac{8Gm}{r_{AB}} \sqrt{\frac{Gm}{r_{AB}}} \right) \tag{B.4}$$

$$= \frac{32}{5c^5} \sqrt{\frac{G^7 m^7}{r_{AB}^9}} \tag{B.5}$$

The expression above is important as it implies that the drag force felt by each BH particle in the simulation is:

$$F = ma = \frac{32}{5c^5} \sqrt{\frac{G^7 m^9}{r_{AB}^9}} \tag{B.6}$$

Which results in an energy loss of the binary per unit time of:

$$\Delta E = 2\pi a F \tag{B.7}$$

where a is the binary's semi-major axis.
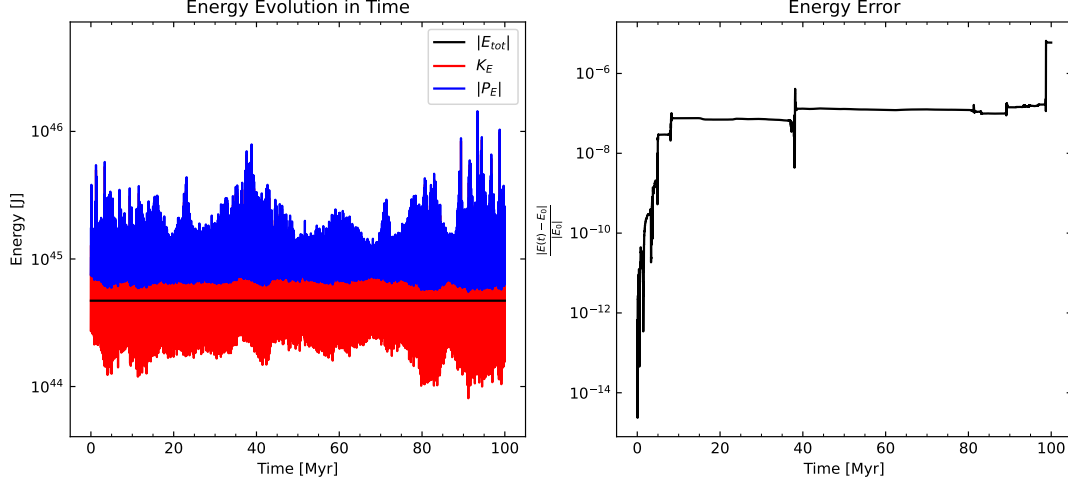
Appendix C: Energy Conservation

Figure C.1: Left: The energy evolution of a specific simulation over time. Right: The corresponding simulations cumulative energy error. The run was using `Hermite`.

Figure C.1 shows how the energy and its error evolve for a given system. As we can see from the left-hand panel, the system starts out virialised to ensure stability (at $t = 0$ years, $P_E = -2K_E$). On the right, we see that the simulation error reaches a value of $\Delta E \approx 10^{-5}$.

Though this is large compared to typical N-body simulations, the root is due to the density of the system causing many close-body encounters. Many algorithms, including `Hermite`, adopt time symmetry. This mechanism ensures that the systematic drift in energy gets suppressed since it forces the simulation (to some extent) to recover its initial conditions when played backwards.

However, this mechanism is only suited for two-body interactions (Prof. dr. Makino, private discussion). During a two-body encounter, errors will naturally arise due to numerical errors and complexity when resolving close encounters. Once the interaction is over, it will diminish back to its original value. However, since we simulate a many-bodied system, the energy error induced by the encounter gets absorbed into the surrounding particles. The absorbing particle carries the energy away before time-symmetrisation can regulate the errors produced, which explains the frequent jumps observed. The error gets amplified by the background IMBH who have just absorbed the excess energy since they may still influence the complex dynamics of the encounter through applying weak perturbations.

Appendix D: Loss Cone

The loss cone forms a fundamental aspect of the final parsec problem. As a reminder, the loss cone defines the region in angular momentum-energy space, which, when occupied, objects can scatter with an existing binary depleting its orbital energy in the process through an exchange of energy.

Here we make use of results following Tremaine and Binney (2008) [11] to investigate how the different algorithms differ in the rate at which particles reach the loss cone boundary of the SMBH. There is a subtle difference here as we do not care for the influence of a third particle on binary systems, but rather, the loss-cone boundary now denotes the region for which the particle will get swallowed by the SMBH. In this case, the angular momentum boundary, J_{crit}, is:

$$J_{\text{crit}} = \sqrt{2GM_{\text{SMBH}}q} \qquad (D.1)$$

where $q = a(1-e)$ is the pericenter of the particle in question. If the particle has $J \leq J_{\text{crit}}$, it has crossed the horizon and will merge with the SMBH. Figure D.1 shows the 2D histogram of the loss cone evolution for every particle simulated in $N_{\text{IMBH}} \leq 40$ simulations. To ensure no systematic errors arise, as before, we constrain the simulations configured with a given population to not go over the average simulation time of the same population when using `GRX` runs.

On the x-axis, we have the initial angular momentum of the particle, while the y-axis shows the final angular momentum. Anything lying below the diagonally dashed line has a decrease in its angular momentum. The data is heavily concentrated in particular regions as signified by the kernel density estimates showing large peaks there. Nevertheless, when comparing the curves in the upper and right-hand panels, we observe that `Hermite` exhibits a larger proportion of its data lying above the diagonal. Furthermore, the lack of a second peak at values $L_f \approx L_{\text{crit}}$ indicates the difficulty Newtonian algorithms have to when inducing merging events due to their omission of GW radiation.
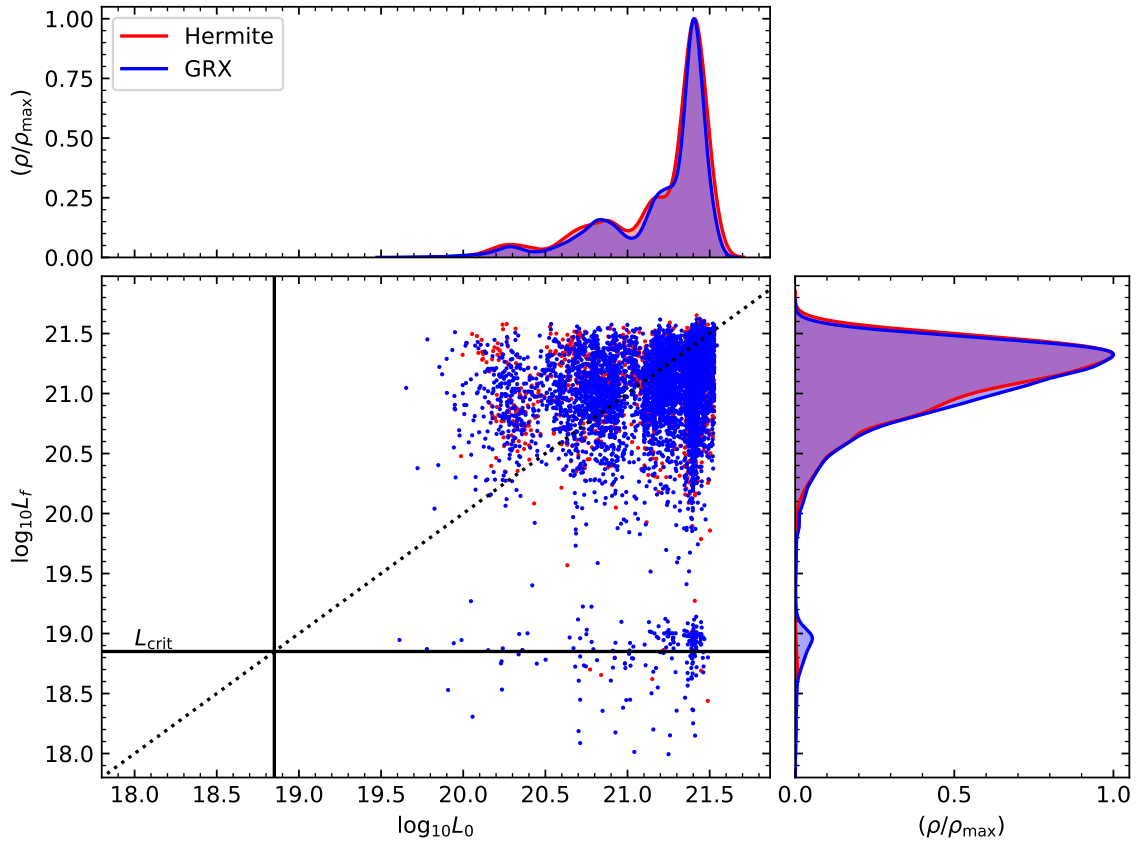
Figure D.1: Evolution of the IMBH's angular momentum. L_{crit} is defined by equation D.1

Appendix E: Ejection Events

N_{IMBH}	10	20	30	40	50	60	70	80	90	100
Counts	3	4	8	10	12	11	9	15	10	17
$\langle t_{\text{ejec}} \rangle$ [Myr]	13.7	39.5	39.7	8.80	11.9	4.90	4.90	1.37	1.81	1.55
min v_{ejec} [km s^{-1}]	242	295	305	258	262	276	262	258	295	265
max v_{ejec} [km s^{-1}]	294	344	625	1050	587	450	599	788	490	817
$\langle v_{\text{ejec}} \rangle$ [km s^{-1}]	268	315	410	412	321	318	368	357	353	421

Table E.1: Summary of ejection velocities depending on the population for `Hermite`.

N_{IMBH}	10	15	20	25	30	35	40
Counts	0	4	1	7	2	1	4
$\langle t_{\text{ejec}} \rangle$ [Myr]	–	19.2	5.87	0.651	1.78	0.637	0.999
min v_{ejec} [km s^{-1}]	–	309	395	300	428	316	258
max v_{ejec} [km s^{-1}]	–	342	395	570	507	316	382
$\langle v_{\text{ejec}} \rangle$ [km s^{-1}]	–	317	395	349	468	316	314

Table E.2: Summary of ejection velocities depending on the population for `GRX`.
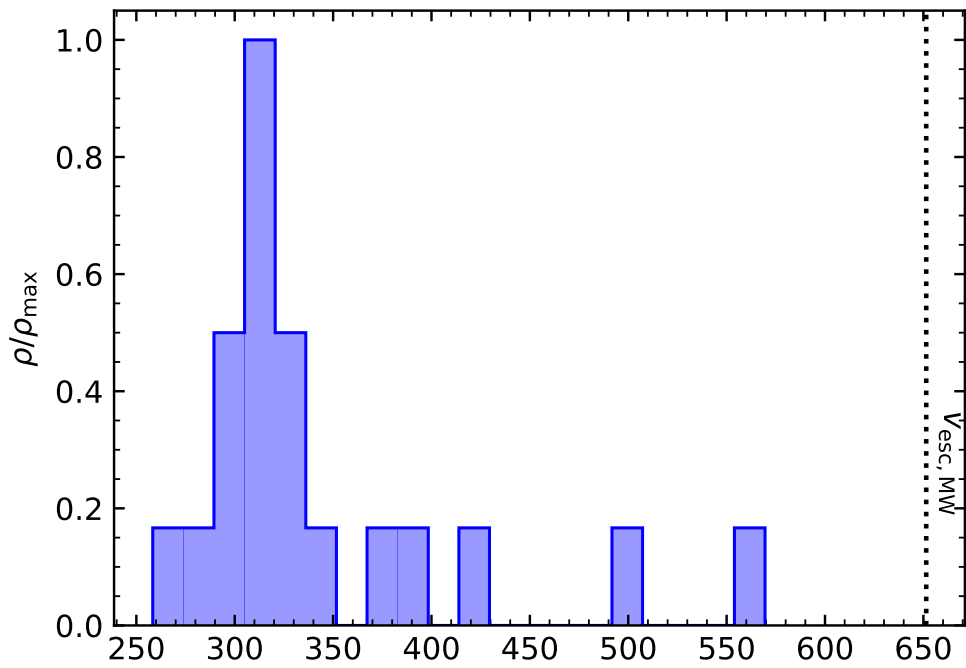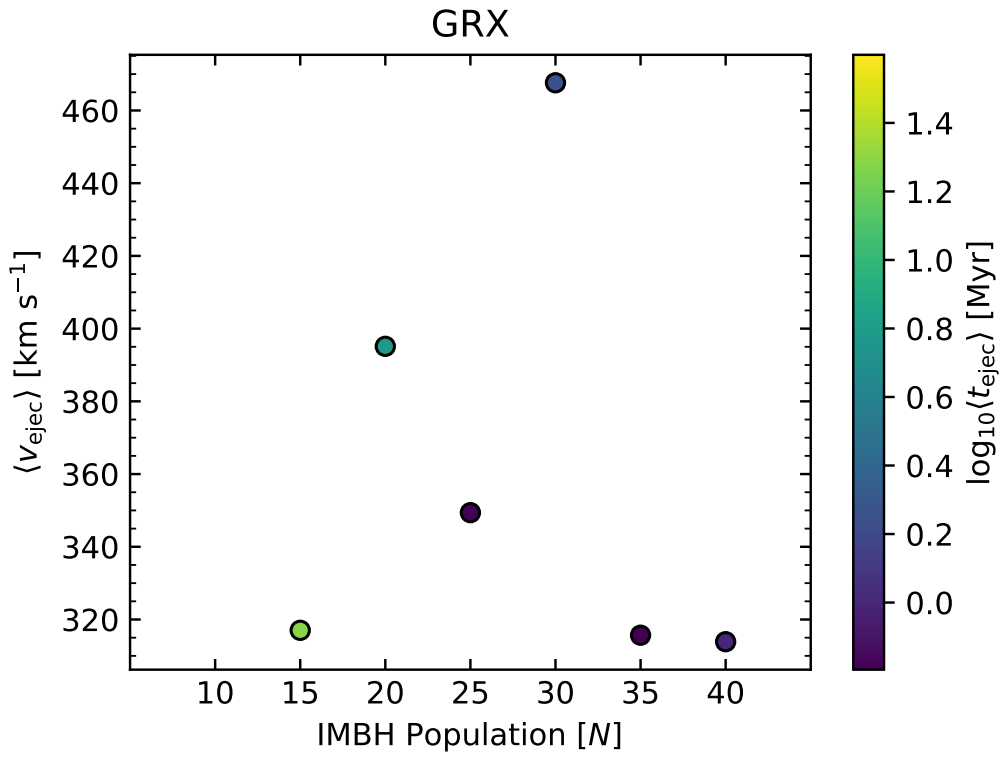
Figure E.1: Top: Average ejection velocities as a function of IMBH population. Bottom: Histogram showing ejection velocities of simulations ending with ejections.

Appendix F: Sustainable Systems

N_{IMBH}	10	20	30	40
Primordial Binaries	0.55	0.95	1.05	1.05
Hard Binaries	0.35	2.55	3.7	5.85
Total Binaries	5.75	18.4	30.8	40.0
$\langle t_{\mathrm{form}}\rangle$ [Myr]	0.02054	0.1271	0.09411	0.190
t_{GW}/t_H	0.00870	0.03270	0.0130	0.00751

N_{IMBH}	10	15	20	25	30	35	40
Primordial Binaries	1	1	0.95	0	1	1.05	0.90
Hard Binaries	0.65	1.63	1.48	1.88	1.10	2.13	3.10
Total Binaries	9.10	13.7	18.6	24.9	28.2	29.1	32.0
$\langle t_{\mathrm{form}}\rangle$ [Myr]	0.02279	0.4404	0.1120	0.1001	0.08377	0.2170	0.1680
t_{GW}/t_H	0.091	0.060	0.0404	0.0301	0.0222	0.02403	0.0211

Table F.1: Summary of binary systems observed. Values for the first three columns correspond to average number of systems found for a given population per simulation. The fourth column denotes the average time taken for the first system to emerge. The last column shows the fraction of binaries with merging timescales less than a Hubble time upon applying equation 2.24. Top: Results for `Hermite`. Bottom: Results for `GRX`.

N_{IMBH}	10	20	30	40
Primordial Tertiaries	0	0	0	0
Total Tertiaries	5.35	15.0	21.9	15.4
$\langle t_{\mathrm{form}}\rangle$ [Myr]	37.428	19.501	16.118	6.7868

N_{IMBH}	10	15	20	25	30	35	40
Primordial Tertiaries	0	0	0	0	0	0	0
Total Tertiaries	0.025	0.075	0	0	0	0	0.500
$\langle t_{\mathrm{form}}\rangle$ [Myr]	4.2350	18.705	–	–	–	–	0.05500

Table F.2: Summary of hierarchical systems observed. When relevant, columns indicate equivalent properties as table F.1. Top: Results for `Hermite`. Bottom: Results for `GRX`.
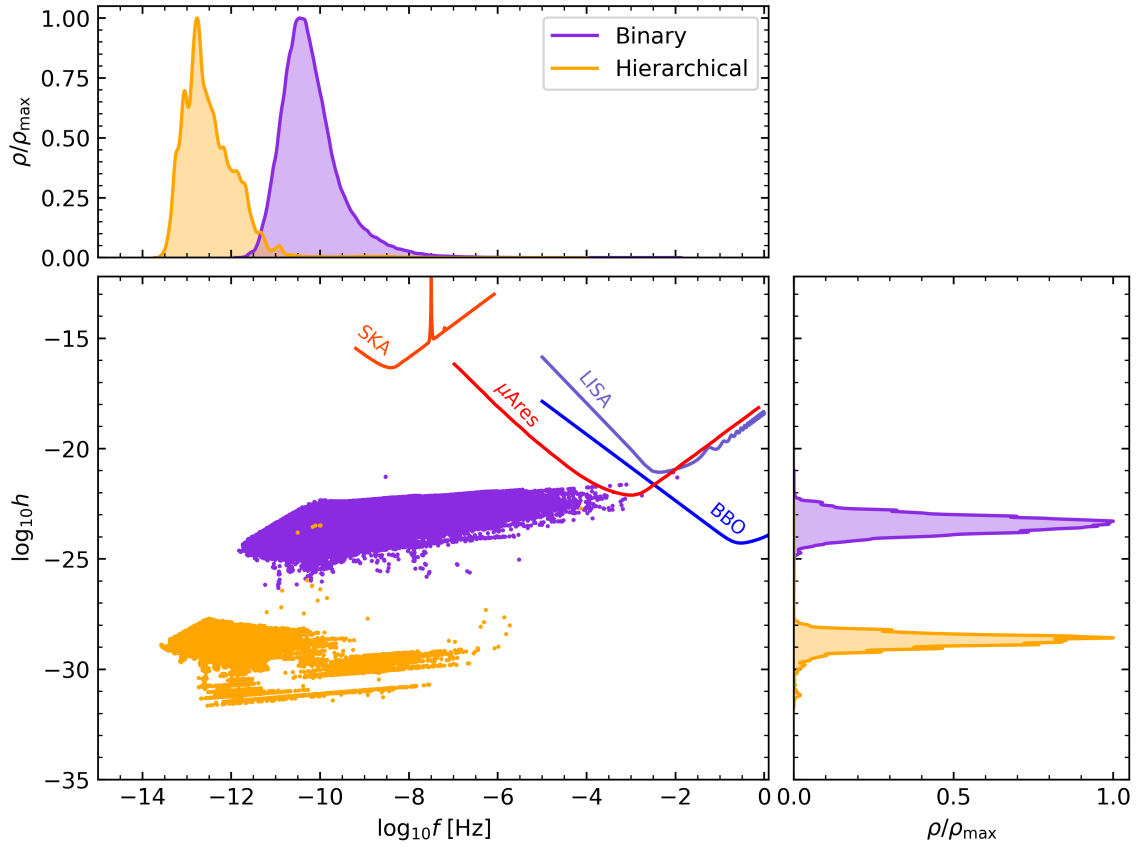
Figure F.1: Diagram showing where GWs emitted by binary systems lie in (f, h)-space in our `Hermite` simulations composed of $N_{\mathrm{IMBH}} \leq 40$.

Appendix G: Gravitational Wave Forecasting

	Hermite	GRX
Avg. NN Event Rate (IMBH-IMBH)	2.690	20.65
Avg. NN Event Rate (SMBH-IMBH)	1.377×10^3	1.667×10^3
Avg. NN Event Rate (Total)	1.379×10^3	1.688×10^3
Avg. SNN Event Rate (IMBH-IMBH)	1.272×10^3	11.46
Avg. SNN Event Rate (SMBH-IMBH)	0	2.120×10^3
Avg. SNN Event Rate (Total)	1.272×10^3	2.131×10^3
Avg. Event Rate (IMBH-IMBH)	1.275×10^3	32.11
Avg. Event Rate (SMBH-IMBH)	1.410×10^4	2.546×10^4
Avg. Event Rate (Total)	1.538×10^4	2.549×10^4

Table G.1: All forecasting values found for GW events. As in the main text, values were taken as the average over all simulations $N \leq 20$ and are given as the number of events per Myr. NN denotes nearest neighbours and SNN, events induced by second nearest neighbours.
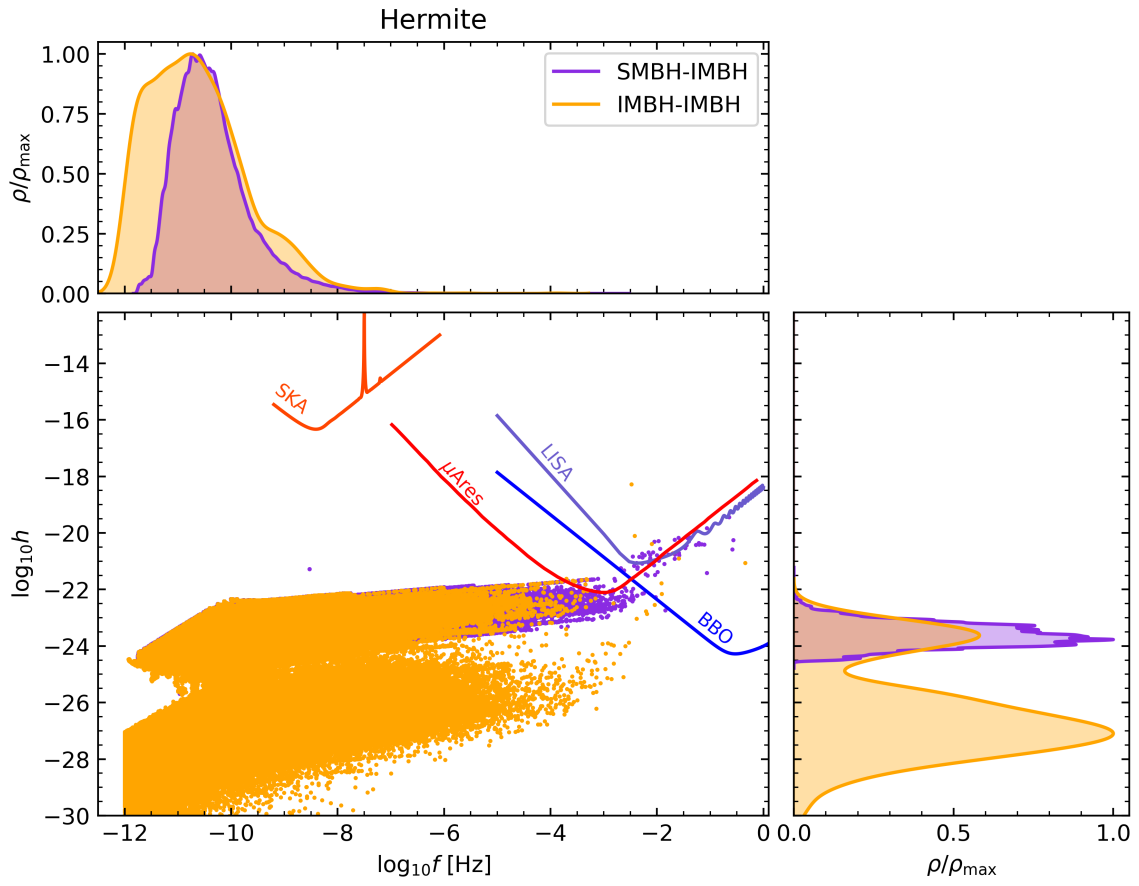
Figure G.1: f vs. h diagram for GW events occuring in all $N_{\mathrm{IMBH}} \leq 40$ `Hermite` simulations.
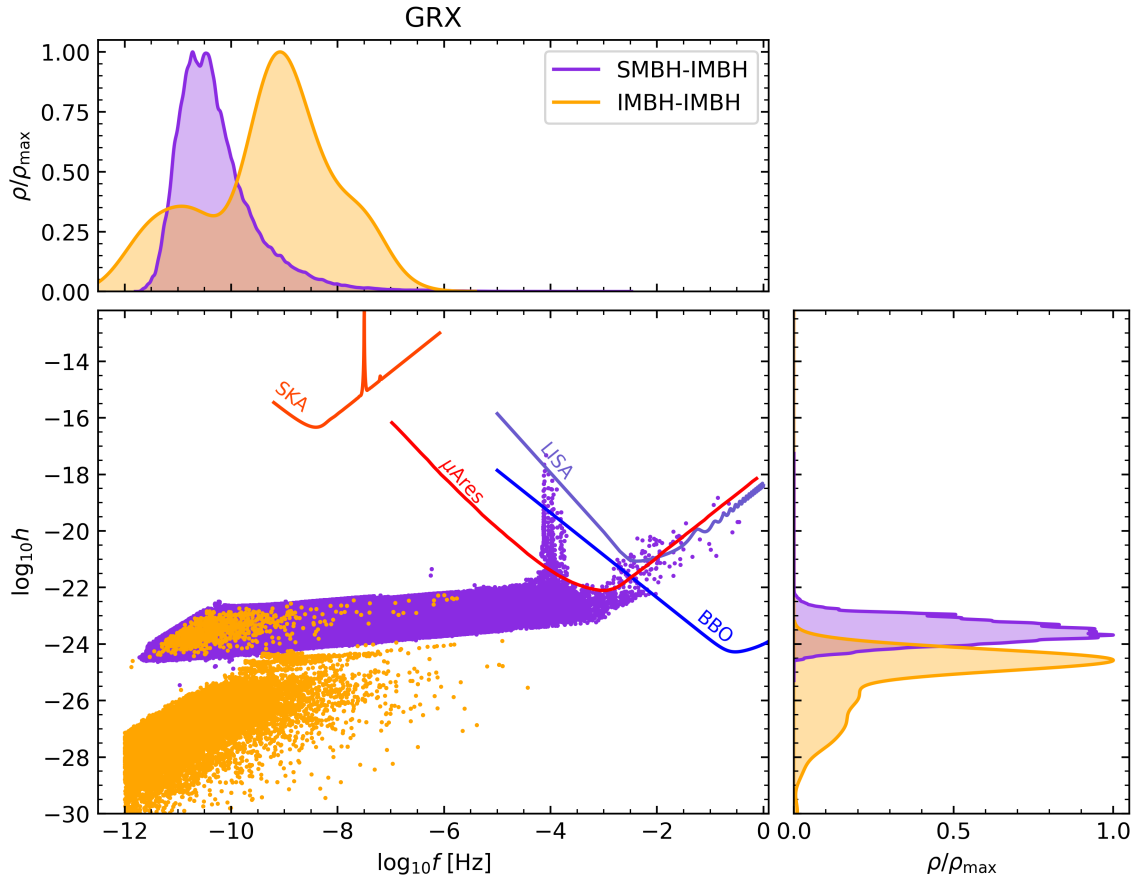
Figure G.2: f vs. h diagram for GW events occuring in all $N_{\mathrm{IMBH}} \leq 40$ GRX simulations.